QUANTIFIED LARGE-SCALE DENSITY FUNCTIONAL THEORY (DFT)
PREDICTIONS OF NUCLEAR PROPERTIES

By

Yuchen Cao

A DISSERTATION

Submitted to
Michigan State University
in partial fulfillment of the requirements
for the degree of

Physics — Doctor of Philosophy

2020

ABSTRACT

QUANTIFIED LARGE-SCALE DENSITY FUNCTIONAL THEORY (DFT) PREDICTIONS OF NUCLEAR PROPERTIES

By

Yuchen Cao

Reflection-asymmetric shapes of the atomic nucleus are relevant to nuclear stability, nuclear spectroscopy, nuclear decays and fission, and the search for new physics beyond the standard model. CP violation in the standard model is too weak to be responsible for the observed matter-antimatter asymmetry. Beyond standard model theories require additional source of CP violation, which could be found if non-zero atomic electric dipole moment (EDM) is observed.

The nuclear quantity that induces the atomic EDM is the Schiff moment, which is enhanced in octupole-deformed odd-mass or odd-odd nuclei where parity doublets exist. This calls for two tasks: First, a global survey of octupole-deformed even-even nuclei to determine the nuclear regions with strong octupole instability; second, Schiff moment calculations in the odd-mass and odd-odd in the vicinity of strongly octupole-deformed even-even nuclei. The calculated Schiff moments will then help us determine the best candidates for atomic EDM measurements. These two tasks constitute the first part of this dissertation.

The tool of choice for a large scale calculation on the entire nuclear landscape is nuclear DFT. Within the DFT framework, the Skyrme HFB method will be used to perform calculations in this dissertation.

Although nuclear DFT is a powerful tool, it lacks the ability to provide quality uncertainty estimates for its predictions. In the second part of this dissertation, we explore several Bayesian machine learning techniques to further increase the predictive power of nuclear

DFT, and to provide full Bayesian uncertainty quantification for DFT predictions.

Dedicated to my family, who have always been supporting me.
To Claire and Samantha, may you be healthy and happy forever.

ACKNOWLEDGMENTS

TABLE OF CONTENTS

LIST OF TABLES

LIST OF FIGURES

Chapter 1

Introduction

1.1 Overview of nuclear properties

The atomic nucleus came to light in 1911 with the formulation of the model from Ernest Rutherford [1], following his interpretation of the Geiger-Marsden experiments (more famously known as the Rutherford gold foil experiment) in 1909 [1]. From the series of scattering experiments, the first nuclear property studied was the charge and size of the nucleus.

With many unknowns to be discovered, the atomic nucleus soon became a testing ground for the rapidly developing field of quantum mechanics. Subsequent studies related to the stability and fission of the nucleus, called for an accurate description of the nuclear mass, or its binding energy, which resulted in the liquid drop model (LDM) formulated by Weizsäcker in 1935 [2].

As one of the first theories to describe the nuclear mass, the LDM provided good approximation of the experimental nuclear masses, and became the predecessor for many theoretical approaches used today [3–5].

However, the shortcoming of the original LDM is its assumption that the nucleus resembles the macroscopic spherical droplet. Microscopic description that takes into account the various quantum mechanical effects of the nucleus is thus required to further advance nuclear theory. Many microscopic theories that were developed over the years can be divided

into three main categories: *ab initio* [6, 7], configuration interaction (shell model) [8, 9], and nuclear density functional theory (DFT) [10, 11].

In order to study the nuclear properties of nuclei across the entire nuclear landscape, the tool of choice is DFT, which replaces protons and neutrons with nucleonic densities. The use of nucleonic densities enables us to scale up the nuclear many-body problem with relatively low computational cost, and also provides an intuitive path to describing and investigating the shape of the nucleus.

Studying various global nuclear properties, such as size, mass, and shape, can help us better understand the boundaries of the nuclear landscape, fission process, nucleosynthesis, and also gives us the tools to probe the fundamental symmetries of our universe.

1.2   Nuclear deformations

The atomic nucleus was initially believed to be spherically shaped. This can be seen in the formulation of the liquid drop model (LDM) [2] in 1935, which assumed the nucleus to be a droplet-like sphere. Around the same time, first evidence for a non-spherical nuclear shape came from the observation of a quadrupole component in the hyperfine structure of optical spectra, which showed that the electric quadrupole moments of the nuclei were more than an order of magnitude larger than the maximum value that could be attributed to a single proton [12, 13]. These observations suggested a collective deformation of the nucleus, which is a result of the nuclear Jahn-Teller effect [14–17].

Most of the quadrupole-deformed nuclei preserve reflection symmetry in their ground states. However, in rare cases, the nucleus can spontaneously break this intrinsic reflection symmetry, and acquire non-zero octupole moments associated with pear-like shapes [18–20]

(see Refs. [21, 22] for comprehensive reviews).

Due to the intrinsic reflection asymmetry, the computational requirement is dramatically increased for calculations involving self-consistent methods. Consequently, early calculations of these shapes were performed using macroscopic-microscopic (MM) models based on the shell correction method [3, 4, 23, 24]. Those were followed by self-consistent studies using nuclear DFT, which made use of different families of energy density functionals (EDFs), such as Gogny [25–28], BCP [26, 29], Skyrme [30, 31], and covariant [32–35].

These studies mostly focused on three specific regions: proton-rich actinides, neutron-rich lanthanides, and neutron-rich heavy and superheavy nuclei which are important for modeling heavy-element nucleosynthesis, and only a handful of them were global surveys [4, 25, 31, 34, 36]. In order to better understand the systematic trend of octupole instability across the nuclear landscape and reduce the bias due to a choice of a particular model, it is important to carry out inter-model comparisons. A global survey of octupole-deformed even-even nuclei using DFT is presented in Ch. 3, and constitutes an important part of this dissertation.

1.3   Schiff moments

The search for additional sources of charge-parity (CP) violation beyond the standard model is an ongoing exciting topic, one of the reasons being that the CP violation in the standard model is too weak to account for the matter and antimatter asymmetry in our universe [37]. If one assumes the CPT theorem to hold, violation of time-reversal (T) is equivalent to CP violation. One of the best ways to observe T violation (together with parity (P) violation) is to measure a non-zero static electric dipole moment (EDMS) of electrons, neutrons, or atoms [38].

Current atomic experiment has set the lower limit of atomic EDM using ^{199}Hg, at $\mid d\left(^{199}Hg\right)\mid < 3.1 \times 10^{-29}e$cm [39]. Due to the screening effect caused by the atomic electrons, the nuclear quantity that induces the atomic EDM is the Schiff moment [40].

It has been known for some time [41–43] that the sensitivity between the measured EDM and the strength of P, T violation coupling constants is enhanced in nuclei with large Schiff moments. The largest enhancements are predicted to be in nuclei which have low-lying parity doublets, and is a common characteristic of octupole-deformed nuclei.

Thus, the global survey of octupole-deformed calculation serves also as a precursor for finding nuclei with potentially large Schiff moments, which could predict better candidates in the atomic EDM measurements.

1.4 Application of Bayesian machine learning to nuclear structure models

Machine learning is one of the most rapidly developing computer science / applied mathematics areas in the past decade. Over the years, machine learning techniques have ventured beyond the scope of computer science and opened up new paths and brought breakthroughs in multiple disciplines.

It is thus natural to also incorporate these techniques into nuclear physics. Various such attempts have been made in nuclear physics [44–49]. Compared to an artificial neural network which determines the model parameters usually via the minimization of some cost function, a Bayesian neural network (BNN) adopts Bayesian inference techniques and determines the probability distributions for the model parameters, which in turn provide predictions in terms of probability distributions. Not only can a Bayesian machine learning approach, such

as the BNN, improve the predictability of our nuclear physics models, it also addresses the burning question of uncertainty quantifications for predictions.

1.5   Organization of this dissertation

This dissertation is organized as follows. Formulation of the nuclear DFT and related nuclear properties can be found in Ch. 2. The global survey of octupole-deformed even-even nuclei will be presented in Ch. 3, followed by Ch. 4, which contains results of Schiff moment calculations in the octupole-deformed actinide region. Chapter 5 describes various applications of Bayesian machine learning to nuclear binding energy. Finally, conclusions and future prospects are presented in Ch. 6.

Chapter 2

Nuclear density functional theory

2.1 Density functional theory

The density functional theory (DFT) was originally developed to investigate the structure of the electronic many-body systems, and was later adapted to investigate the structure of nuclear systems.

In nuclear DFT, protons and neutrons are described using nucleonic densities and currents. The advantage of doing so compared with solving the many-body Schrödinger equation directly is that in the latter, the problem will quickly become computationally infeasible as the number of particles increases, whereas this has little impact in the DFT framework. By replacing the interactions between nucleons with a mean-field, the exact strong nuclear force does not have to be known, further simplifying the problem. For these reasons, the nuclear DFT is capable of describing all nuclear systems in the nuclear landscape, and becomes especially useful in heavy systems where other theories cannot be used. This makes DFT the preferred theoretical tool to for large-scale surveys of nuclear properties.

2.1.1 General formalism

DFT is firmly rooted in the Hohenberg-Kohn theorems (H-K) [50]. The first H-K theorem states that the energy of an N-body system can be uniquely determined by the local particle

density $\rho(\boldsymbol{r})$, which only depends on the $3N$ spatial coordinates, thus greatly simplifying the many-body problem. The second H-K theorem says that for any nondegenerate system of particles put into a local external field, there exists a universal energy functional of the particle density $E[\rho]$, which is minimized at the correct ground state density $\rho_{\mathrm{g.s.}}(\boldsymbol{r})$. This minimized energy will correspond to the ground state total energy of the system $E^{min}[\rho_{\mathrm{g.s.}}] = E_{\mathrm{g.s.}}$.

To solve the nuclear ground state using the H-K theorems, we are left with two problems to tackle. First, we need to find the correct energy functional. Since we do not know the exact nuclear interactions, we'll have to resort to certain approximations methods. In practice, an energy density functional (EDF) $\mathcal{H}(\boldsymbol{r})$ is constructed, which is a real, scalar, isoscalar function of local densities and their derivatives. Integrating $\mathcal{H}(\boldsymbol{r})$ over space gives the total energy of the nucleus:

$$E[\rho] = \int \mathcal{H}(\boldsymbol{r}) d^3 r. \tag{2.1}$$

Examples of nuclear EDFs are the Skyrme EDFs (Sec. 2.1.2), Gogny EDFs [51–53], and covariant EDFs [54–57], which are, respectively, based on the zero-range Skyrme interaction [58,59], the finite range Gogny interaction [10,60], and the meson exchange forces [61]. In my work, Skyrme EDFs are used, due to the simplicities offered by the zero-range interaction, and good predictive power when it comes to experiment.

The second problem is to solve for the ground state particle density. In the electronic system, this is solved by means of variational method prescribed in the Kohn-Sham theorem (KS) [62]. In a nuclear system, since the nucleus is a self-bound system, this external field present in the electronic KS formulation is absent and creates conceptual problems. The

corrective treatments are complicated in practical implementation, thus in practice, nuclear DFT relies on mean-field variational methods such as the Hartree-Fock and Hartree-Fock-Bogoliubov method to solve for the ground state density of the nucleus. These methods will be discussed in Sec. 2.1.3.1 and 2.1.3.2.

2.1.2 Skyrme energy density functional (EDF)

Within the HFB framework, the total energy density $\mathcal{H}(r)$ in Eq. (2.1), using the zero-range Skyrme EDF, can be expressed as:

$$\mathcal{H}(r) = \mathcal{H}_{kin} + \mathcal{H}_{int} + \mathcal{H}_{Coul} + \mathcal{H}_{pair} - \mathcal{H}_{corr}, \tag{2.2}$$

where the terms on the right hand side correspond, respectively, to the kinetic energy density, interaction energy density, Coulomb energy density, pairing energy density, and correction for the spurious center of mass motion [10].

The kinetic energy density can be written as:

$$\mathcal{H}_{\text{kin}}(\boldsymbol{r}) = \frac{\hbar^2}{2m} \left(1 - \frac{1}{A}\right) \left(\tau_p(\boldsymbol{r}) + \tau_n(\boldsymbol{r})\right), \tag{2.3}$$

where the kinetic densities $\tau(\mathbf{r})$ can be expressed with the nonlocal densities $\rho\left(\mathbf{r}, \mathbf{r}'\right) = \left\langle \Psi \left| a^{\dagger}_{\boldsymbol{r}'} a_{\boldsymbol{r}} \right| \Psi \right\rangle$ as:

$$\tau(\mathbf{r}) = \nabla_{\mathbf{r}} \nabla_{\mathbf{r}'} \rho\left(\mathbf{r}, \mathbf{r}'\right)_{\mathbf{r}'=\mathbf{r}}, \tag{2.4}$$

The symbol A represents the mass number (total number of nucleons) and $\left(1 - \frac{1}{A}\right)$ is the center of mass correction. The subscripts $q = n, p$ correspond to neutrons (n) and protons (p), and will be used in the remainder of this dissertation.

The interaction energy density of the Skyrme EDF is based on the zero-range Skyrme force [58, 59], and can be written as a sum of the time-even and time-odd terms:

$$\mathcal{H}_{\text{int}}(\boldsymbol{r}) = \sum_{t=0,1} \left(\mathcal{E}_t^{\text{even}} + \mathcal{E}_t^{\text{odd}} \right), \tag{2.5}$$

$$\mathcal{E}_t^{\text{even}}(\boldsymbol{r}) = C_t^\rho \rho_t^2 + C_t^{\Delta\rho} \rho_t \Delta\rho_t + C_t^\tau \rho_t \tau_t + C_T^J \mathbb{J}_T^2 + C_t^{\nabla J} \rho_t \boldsymbol{\nabla} \cdot \boldsymbol{J}_t, \tag{2.6}$$

$$\mathcal{E}_t^{\text{odd}}(\boldsymbol{r}) = C_t^s \boldsymbol{s}_t^2 + C_t^{\Delta s} \boldsymbol{s}_t \cdot \Delta\boldsymbol{s}_t + C_t^T \boldsymbol{s}_t \cdot \boldsymbol{T}_t + C_t^j \boldsymbol{j}_t^2 + C_t^{\nabla j} \boldsymbol{s}_t \cdot (\boldsymbol{\nabla} \times \boldsymbol{j}_t), \tag{2.7}$$

where ρ_t, τ_t are the particle and kinetic energy density, respectively; $\mathbb{J}_t$ is the spin-current tensor energy densities and $\boldsymbol{J}_t$ the spin-orbit current density; $\boldsymbol{s}_t$ and $\boldsymbol{T}_t$ are the spin density and spin kinetic density; $\boldsymbol{j}_t$ is the momentum density. The symbols $t = 0$ and $t = 1$ corresponds to the isoscalar or isovector densities, respectively, $\rho_0 = \rho_n + \rho_p$ and $\rho_1 = \rho_n - \rho_p$. Additional discussion of these densities can be found in Ref. [10].

In many cases, one is interested in the ground states of even-even nuclei, where time reversal symmetry is conserved and the time-odd terms (2.7) vanish. Most of the time-even coupling constants C are real numbers, except for C_t^ρ, which is a density-dependent function:

$$C_t^\rho = C_{t0}^\rho + C_{tD}^\rho \rho^\gamma. \tag{2.8}$$

The Coulomb energy density from the protons can be divided into the direct term and the exchange term, which is a result of the anti-symmetrization:

9

$$\mathcal{H}_{\text{Coul}} = \mathcal{H}_{\text{Coul}}^{\text{dir}} + \mathcal{H}_{\text{Coul}}^{\text{exc}}, \tag{2.9}$$

$$\mathcal{H}_{\text{Coul}}^{\text{dir}}(\boldsymbol{r}) = \frac{e^2}{2} \int d\boldsymbol{r}' \frac{\rho_p(\boldsymbol{r})\rho_p(\boldsymbol{r}')}{\boldsymbol{r} - \boldsymbol{r}'}, \tag{2.10}$$

$$\mathcal{H}_{\text{Coul}}^{\text{exc}}(\boldsymbol{r}) \approx -\frac{3e^2}{4}\left(\frac{3}{\pi}\right)^{1/3}\rho_p^{4/3}(\boldsymbol{r}). \tag{2.11}$$

The above form of Coulomb exchange term is calculated in the Slater approximation [58,63] to avoid involving non-local densities.

Therefore, the standard Skyrme interaction energy density $\mathcal{H}_{\text{int}}(\boldsymbol{r})$ can be described by 13 parameters:

$$\left\{ C_{t0}^{\rho}, C_{tD}^{\rho}, C_t^{\Delta\rho}, C_t^{\tau}, C_t^{J}, C_t^{\nabla J} \right\}_{t=0,1} \quad \text{and } \gamma. \tag{2.12}$$

Furthermore, some of the parameters in (2.12) can be represented in terms of the nuclear matter (NM) properties: the total energy per nucleon E/A and density ρ_c at equilibrium; the isoscalar and isovector effective masses M_s^* and M_v^*, respectively; the nuclear matter incompressibility K; the symmetry energy coefficient a_{sym}; and the density dependence of the symmetry energy L_{sym}. (2.12) can then be represented by the following, more commonly used parameters:

$$\begin{aligned} &\left\{ \rho_c, E^{\text{NM}}/A, M_s^*, M_v^*, K^{\text{NM}}, a_{\text{sym}}^{\text{NM}}, L_{\text{sym}}^{\text{NM}} \right\}, \\ &\left\{ C_t^{\Delta\rho}, C_t^{J}, C_t^{\nabla J} \right\}_{t=0,1}. \end{aligned} \tag{2.13}$$

The pairing energy density $\mathcal{H}_{\text{pair}}$ is to account for the superfluid correlation that involves nucleons that occupy orbitals with the same quantum numbers but opposite spin; such nucleons tend to couple into Cooper pairs. The pairing energy density is usually written as:

$$\mathcal{H}_{\text{pair}} = \sum_{q=n,p} \frac{V_0^q}{2} \left[1 - \frac{\rho_0(\boldsymbol{r})}{2\rho_c} \right] \tilde{\rho}_q^2(\boldsymbol{r}), \tag{2.14}$$

where V_0^q is the pairing strength, and can have different values for protons and neutrons. $\rho_c \approx 0.16 \text{ fm}^{-3}$ is the saturation density. $\rho_0(\boldsymbol{r})$ and $\tilde{\rho}_q(\boldsymbol{r})$ are the isoscalar particle density and the pairing density, respectively.

2.1.3   Hartree-Fock-Bogoliubov method (HFB)

2.1.3.1   Hartree-Fock method

The ground state density of a nuclear system is obtained by using the variational methods such as the Hartree-Fock (HF) and Hartree-Fock-Bogoliubov method (HFB).

The HF equation is obtained by varing the energy functional $E[\rho]$ (2.1) with respect to the particle density ρ:

$$\delta E[\Psi] = 0, \tag{2.15}$$

with

$$E[\Psi] = \frac{\langle \Psi | E[\rho] | \Psi \rangle}{\langle \Psi | \Psi \rangle}. \tag{2.16}$$

The HF ground state wave function $|\Psi\rangle$ is represented by a Slater determinant [64] of single particle (KS) states

$$|\Psi\rangle = \prod_{i=1}^{A} \hat{a}_i^\dagger |0\rangle, \tag{2.17}$$

where the HF creation and annihilation operators $\hat{a}_k^\dagger$, $\hat{a}_k$ act on the HF vacuum, and represent the single particle wave functions ϕ_k. The single particle wave functions are the

eigenfunctions of the single particle (KS) Hamiltonian $\hat{h}$:

$$\hat{h}(i)\phi_k(i) = \epsilon_k(i)\phi_k(i), \ i = \{\boldsymbol{r}_i, s_i, q_i\}, \tag{2.18}$$

which sums up to be the total Hamiltonian of the HF system $\hat{H}^{\mathrm{HF}} = \sum_{i=1}^{A} \hat{h}(i)$. In practice, we usually solve the HF equations in the configuration space on some complete and orthogonal set of basis functions $\{\chi_l\}$:

$$\phi_k = \sum_l D_{lk}\chi_l. \tag{2.19}$$

For each χ_l, we can define their corresponding fermion operators $\hat{c}_l^\dagger, \hat{c}_l$, and express the single particle operators $\hat{a}_k^\dagger, \hat{a}_k$ as:

$$\begin{aligned} \hat{a}_k^\dagger &= \sum_l D_{lk}\hat{c}_l^\dagger, \\ \hat{a}_k &= \sum_l D_{lk}\hat{c}_l. \end{aligned} \tag{2.20}$$

2.1.3.2 Bogoliubov transformation and the HFB equations

The HF wave function does not take into account the short-range particle-particle correlations. In practice, the HF method is often used in parallel with the BCS pairing model [65], which is an analog of the BCS theory for superconductivity [66]. The HFB method combines and generalizes both the HF and BCS theory. The HFB ground state wave function can be written as:

$$|\Psi\rangle = \prod_k \hat{\beta}_k^\dagger |0\rangle, \tag{2.21}$$

where $\hat{\beta}_k^\dagger, \hat{\beta}_k$ are the quasi-particle (q.p.) operators which obey the fermion anti-commutation

relation, and relates to the operators $\hat{c}_l^\dagger, \hat{c}_l$ in (2.20) via the Bogoliubov transformation:

$$\hat{\beta}_k^\dagger = \sum_l U_{lk}\hat{c}_l^\dagger + V_{lk}\hat{c}_l,$$

$$\hat{\beta}_k = \sum_l U_{lk}^*\hat{c}_l + V_{lk}^*\hat{c}_l^\dagger. \tag{2.22}$$

We can define a unitary transformation matrix $\mathcal{W}^\dagger$,

$$W^\dagger \equiv \begin{pmatrix} U^\dagger & V^\dagger \\ V^T & U^T \end{pmatrix}, \tag{2.23}$$

and rewrite the transformation (2.22) as

$$\begin{pmatrix} \hat{\beta} \\ \hat{\beta}^\dagger \end{pmatrix} = \mathcal{W}^\dagger \begin{pmatrix} \hat{c} \\ \hat{c}^\dagger \end{pmatrix}. \tag{2.24}$$

Using the matrices U, V, the particle density $\rho_{ll'} = \langle\Psi| \hat{c}_{l'}^\dagger \hat{c}_l |\Psi\rangle$ and the HFB pairing tensor $\kappa = \langle\Psi| \hat{c}_{l'} \hat{c}_l |\Psi\rangle$ can be written in the matrix form as:

$$\rho = V^*V^T,$$

$$\kappa = V^*U^T. \tag{2.25}$$

The pairing tensor κ is simply related to the pairing density $\tilde{\rho}$ (2.14) [67]. The densities ρ and $\tilde{\rho}$ (or κ) uniquely define the energy of the system according to the H-K theorems [68]. Variation of the total energy 2.1 with respect to ρ and $\tilde{\rho}$ yields the HFB equations [69]:

$$\begin{pmatrix} h - \lambda & \Delta \\ -\Delta^* & -h^* + \lambda \end{pmatrix} \begin{pmatrix} U_k \\ V_k \end{pmatrix} = E_k \begin{pmatrix} U_k \\ V_k \end{pmatrix}, \tag{2.26}$$

with

$$h_{ij} = t_{ij} + \sum_{kl} \bar{v}_{iljk}\rho_{kl},$$

$$\Delta_{ij} = \frac{1}{2} \sum_{kl} \bar{v}_{ijkl}\kappa_{kl}, \tag{2.27}$$

where h is the self-consistent HF field, Δ is the self-consistent pairing field, and λ is the chemical potential. The HFB equation eigenvalues E_k represent q.p. energies, and $(U_k, V_k)^T$ are the HFB eigenvectors of the HFB ground state. Due to the density dependence of the mean-fields, the HFB equations are non-linear and thus need to be solved using a self-consistent approach, such as iterative diagonalization. Various HFB solvers exists, e.g. HF-BTHO(v3.00) [70] and HFODD (v2.73y) [71]. The former is the main solver that I used for calculations in this dissertation, and the latter contains more functionalities and the ability to break all self-consistent symmetries.

2.1.4 Other considerations

2.1.4.1 Constrained calculations

The Bogoliubov transformation (2.22) does not conserve particle number, thus we need to control the correct particle number by introducing a constraint. A common method to introduce constraints is to use the Lagrangian multiplier method. The modified total energy, or Routhian, E' can be written as:

$$E' = E - \lambda_n \left\langle \hat{N}_n \right\rangle - \lambda_p \left\langle \hat{N}_p \right\rangle, \tag{2.28}$$

where $\hat{N}_n$, $\hat{N}_p$ are the neutron and proton particle number operators, λ_n and λ_p are the corresponding Fermi energies, which are determined once the conditions $\left\langle \hat{N}_q \right\rangle = N_q$ are met.

Other more advanced restoration schemes, such as the Lipkin-Nogami method [69, 72–75] are also commonly used.

Constraints on the deformation of the nucleus can also be introduced via Lagrangian multipliers $C_{\lambda\mu}$:

$$E' = E - \sum_{\lambda\mu} C_{\lambda\mu} \left(\left\langle \hat{Q}_{\lambda\mu} \right\rangle - \bar{Q}_{\lambda\mu} \right)^2 , \tag{2.29}$$

where the $\hat{Q}_{\lambda\mu}$ are the mass multipole moment operators and $\bar{Q}_{\lambda\mu}$ the desired values of the multipole moments. Another commonly used method for constraining the deformations is the linear constraint method [76],

$$E' = E - \sum_{\lambda\mu} C_{\lambda\mu} \left(\left\langle \hat{Q}_{\lambda\mu} \right\rangle - \bar{Q}_{\lambda\mu} \right) , \tag{2.30}$$

where the Lagrange parameters $C_{\lambda\mu}$ are readjusted at every iteration following the procedures in Ref. [76]. This method for the multipole moment constraint is implemented in recent versions of the HFB solvers HFBTHO [70, 77] and HFODD [71, 78].

2.1.4.2 Deformations

One way to describe the deformation of the nucleus is to use the length of the radius vector at a given point on the nucleus' surface. It can be expanded using the orthonormalized spherical harmonics [68]:

$$r(\theta, \phi) = R_0 \left(1 + \alpha_{00} + \sum_{\lambda=1}^{\infty} \sum_{\mu=-\lambda}^{\lambda} \alpha_{\lambda\mu}^* Y_{\lambda\mu}(\theta, \phi) \right) . \tag{2.31}$$

In (2.31) R_0 is the radius of a sphere that has the same volume as the nucleus. The constant α_{00} serves to fix the volume of the nucleus to $V = \frac{4}{3}\pi R_0^3$. In the small deformation limit,

the $\lambda = 1$ terms mostly describe the translation of the nucleus as a whole, and are usually fixed by constraining the center of mass of the nucleus to the origin:

$$\int_V \boldsymbol{r} d^3 r = 0. \tag{2.32}$$

This condition is automatically satisfied if the system is reflection symmetric, in which case the expansion, equation 2.31, only contains even-valued λ terms. In systems with non-zero odd-value $\lambda > 1$ terms, e.g. in reflection asymmetric nuclei, one needs to constrain the corresponding $Q_{1\mu}$ (2.29) to zero in order to correctly describe the nuclear deformations.

In an axially symmetric system, all $\mu \neq 0$ terms of $\alpha_{\lambda\mu}$ become zero, and the remaining non-zero $\alpha_{\lambda 0}$ are usually called β_λ. The $\lambda = 2, 3, 4, ...$ terms describe the quadrupole, octupole, and hexadecapole deformations etc., respectively.

Another way to describe the deformations, which relate to the β_λ values, are the mass multipole moments $Q_{\lambda 0}$. Unlike the dimensionless β_λ values, the multipole moments are subject to an arbitrary constant factor. A common definition for the quadrupole ($\lambda = 2$) and octupole ($\lambda = 3$) moments is:

$$\begin{aligned} Q_{20} &= \left\langle 2z^2 - x^2 - y^2 \right\rangle, \\ Q_{30} &= \left\langle z \left(2z^2 - 3x^2 - 3y^2 \right) \right\rangle, \end{aligned} \tag{2.33}$$

where they relate to the deformation parameters β_2 and β_3 via:

$$\begin{aligned} \beta_2 &= Q_{20} / \left(\sqrt{\frac{16\pi}{5}} \frac{3}{4\pi} A R_0^2 \right), \\ \beta_3 &= Q_{30} / \left(\sqrt{\frac{16\pi}{7}} \frac{3}{4\pi} A R_0^3 \right). \end{aligned} \tag{2.34}$$

16

For R_0 one usually adopts the semi-empirical expression $R_0 = 1.2A^{1/3}$ fm.

In practice, one needs to be wary of the potentially different definitions of the multipole moments when comparing results. A somewhat safer option is to compare β_λ parameters.

2.1.4.3 Blocking calculation for odd systems

In an even-odd or odd-odd nucleus, the unpaired nucleons carry non-zero angular momentum. The non-zero angular momentum breaks time-reversal symmetry, which results in the presence of time-odd fields (2.7). In the HFB framework, the so-called particle blocking is required, making calculations in odd systems more computationally involved compared to their even-even neighbors.

In HFB, an odd-A nucleus can be viewed as a one q.p. excitation $\hat{\beta}_{\mu_0}^\dagger$ with respect to the ground state of its even-even neighbor. For instance, in the case of a even-proton, odd-neutron nucleus (Z, N), its ground state wave function can be expressed as:

$$|\Psi(Z, N)\rangle = \hat{\beta}_{\mu_0}^\dagger |\Psi(Z, N-1)\rangle, \qquad (2.35)$$

where μ_0 represents the quantum numbers of the blocked state [79]. A full blocking method treats the time-reversed component $\bar{\mu}_0$ of the q.p. state μ_0 properly when modifying the density matrix and pairing tensor (2.25). For the detailed description of blocking, see Refs. [79–81]

An approximate approach to blocking is the so-called equal filling approximation (EFA) [82, 83]. EFA treats the Kramers-degenerate states μ_0 and $\bar{\mu}_0$ with equal weights when they enter the density matrix and pairing tensor (2.25), thus conserving time-reversal symmetry. This allows odd systems to be calculated in the absence of the time-odd fields (2.7).

It has been shown that EFA is practically equivalent to the exact blocking when time-odd fields are set to zero, and even when they are switched on, the impact to the ground state energy is rather small [77,81]. Thus EFA can be used to explore odd systems, without needing to deal with the time-odd terms (2.7).

2.2   Schiff moment and the atomic electric dipole moment

The Schiff moment [40] serves as a bridge between the atomic electric dipole moment (EDM) and the parity (P) and time-reversal (T) symmetry violating nucleon-nucleon (πNN) interaction mediated by the pion. Several estimates of the atomic EDM expressed in terms of the Schiff moment have been given, e.g. ^{129}Xe [84–86], odd-mass isotopes of Rn, Fr, Ra, Ac, and Pa [87], and ^{239}Pu.

Because of atomic electrons' screening [40], the nuclear quantity that induces the the atomic EDM is not the nuclear dipole moment but rather the Schiff moment (to the first order [88]),

$$S \equiv \langle \Psi_0 | \hat{S}_z | \Psi_0 \rangle = \sum_{i \neq 0} \frac{\langle \Psi_0 | \hat{S}_z | \Psi_i \rangle \langle \Psi_i | \hat{V}_{\mathrm{PT}} | \Psi_0 \rangle}{E_0 - E_i} + \mathrm{c.c.}, \tag{2.36}$$

where $|\Psi_0\rangle$ is the member of the ground state multiplet with the maximum z-axis projection of the angular momentum J, and the sum runs over all excited states $|\Psi_i\rangle$. $\hat{S}_z$ is the third component of the Schiff operator, written as:

$$\hat{S}_z = \frac{e}{10} \sum_p \left(r_p^2 - \frac{5}{3} \bar{r}_{\mathrm{ch}}^2 \right) z_p. \tag{2.37}$$

The energy denominator in Eq. (2.36) implies that the lowest excited states dominate

the sum in (2.36). This makes octupole-deformed nuclei of particular interest. An octupole-deformed nucleus with odd-numbered neutrons or/and protons, is commonly accompanied by the existence of a parity doublet, which is a near-degenerate state with the same angular momentum as the ground state but with reversed parity [21, 22, 89]. For instance, in ^{225}Ra the energy splitting between the ground state with $J^{\pi} = 1/2^{+}$ and its opposite parity partner with $J^{\pi} = 1/2^{-}$ is $\Delta E \approx 55$keV [90]. In the rigid-deformation limit of DFT, the ground state $|\Psi_0\rangle = |J^{+}\rangle$ and its opposite parity partner $|\bar{\Psi}_0\rangle = |J^{-}\rangle$ are projections onto good parity and angular momentum of the same intrinsic state, and the Schiff moment (2.36) can be approximated as [91]:

$$S \approx -2\frac{\langle\Psi_0|\hat{S}_z|\bar{\Psi}_0\rangle\langle\bar{\Psi}_0|\hat{V}_{\text{PT}}|\Psi_0\rangle}{\Delta E} = -2\frac{J}{J+1}\frac{\langle\hat{S}_z\rangle\langle\hat{V}_{PT}\rangle}{\Delta E}, \tag{2.38}$$

where $\langle\hat{S}_z\rangle$ and $\langle\hat{V}_{PT}\rangle$ are the expectation values of S_z and V_{PT} in the intrinsic frame of the nucleus.

The work that I have done in this dissertation focus on evaluating the intrinsic Schiff moment $\langle\hat{S}_z\rangle$ expression (2.37) in the framework of HFB. Assuming axially symmetric (around z-axis) deformations, it can be expressed in the integral form:

$$\langle\hat{S}_z\rangle \equiv \frac{e}{10}\int\rho_p r_p^2 z_p d^3r. \tag{2.39}$$

This expression (2.39) will be evaluated for odd-A and odd-odd systems in the actinide region (Ch. 4) that have one nucleon more than their even-even neighbors predicted to be octuple-deformed in Ch. 3.

Chapter 3

Global survey of octupole-deformed even-even nuclei

In this chapter, I'll discuss the procedure and final results of the global survey of octupole-deformed even-even nuclei. Part of the results have been published on arXiv [92] and submitted to Physical Review C.

Calculations for the octupole-deformed even-even nuclei are performed using a modified version (Sec. 3.1.4) of the HFBTHO (v3.00) solver. Particle number symmetry is restored using the Lipkin-Nogami prescription, and the linear constraint method is used for the deformation constraints (Sec. 2.1.4.1).

We selected five Skyrme energy density functionals (SEDFs, see Sec. 2.1.2): UNEDF0 [93], UNEDF1 [94], UNEDF2 [95], SLy4 [96], and SV-min [97] to perform the calculation of octupole-deformed even-even nuclei. The selection of these interactions comes naturally as this work is an extension to the quadrupole mass-table calculated in 2012 that used the above SEDFs [98]. The root-mean-square (rms) error of BE, when comparing to the experimental masses in the mass evaluation AME2016 [99], ranges from 1.7 MeV (UNEDF0) to 5.3 MeV (SLy4).

Reflection-asymmetric calculations were performed in all even-even nuclei with $Z \leq 120$, starting with neutron numbers around (less than) the proton drip-line and a few beyond

the neutron drip-line, to ensure all bound systems are included, up to neutron number $N = 300$. A total of 2836 nuclei were computed for each of the SEDFs, resulting in five octupole-deformed mass-tables.

In the results reported here, we removed all systems with $Z \geq 112$, due to the fact that Coulomb frustration at this region could introduce exotic shapes such as bubbles and tori [100–105], and multipole moments constraints are insufficient in describing these nuclear shapes. The results in this region display frequent crossings among two-neutron separation energy lines between different isotopic chains, and irregular jumps in the deformations within a given isotopic chain, which indicates instability of the results.

3.1 Technical details of the global calculation

3.1.1 Potential energy surface (PES) and the HFB ground-state

Within the nuclear DFT framework, a common strategy to find the shape of a nucleus is to perform a set of constrained calculations to create the potential energy surface (PES).

By employing the Lagrange multiplier method, we can constrain the deformation of the nucleus in terms of its multipole moments, i.e. quadrupole moment Q_{20} and octupole moment Q_{30} etc.(Sec. 2.1.4.2), to find the energy of the nucleus at this particular shape. We can then create a two-dimensional grid, where each mesh point would correspond to a value of (Q_{20}, Q_{30}), and perform constrained calculations for the entire surface. After these calculations converge, each (Q_{20}, Q_{30}) pair will have a corresponding energy, in our case where the Hartree-Fock-Bogoliubov method is used, the HFB energy. The global minimum of these energies will be chosen as the nucleus' ground-state (g.s.) binding energy (BE) in the PES, and thus the corresponding (Q_{20}, Q_{30}) are its g.s. deformations.

Figure 3.1 is an example of a PES for the ^{224}Ra nucleus using the SLy4 Skyrme EDF. The white circle, $(Q_{20}^{\text{PES g.s.}}, Q_{30}^{\text{PES g.s.}}) = (1711 \text{ fm}^2, 3312 \text{ fm}^3)$, represents the position of the g.s. deformations, and its $\text{BE}^{\text{PESg.s.}}$ (-1710.705 MeV) serves as the zero-energy of the color contour.
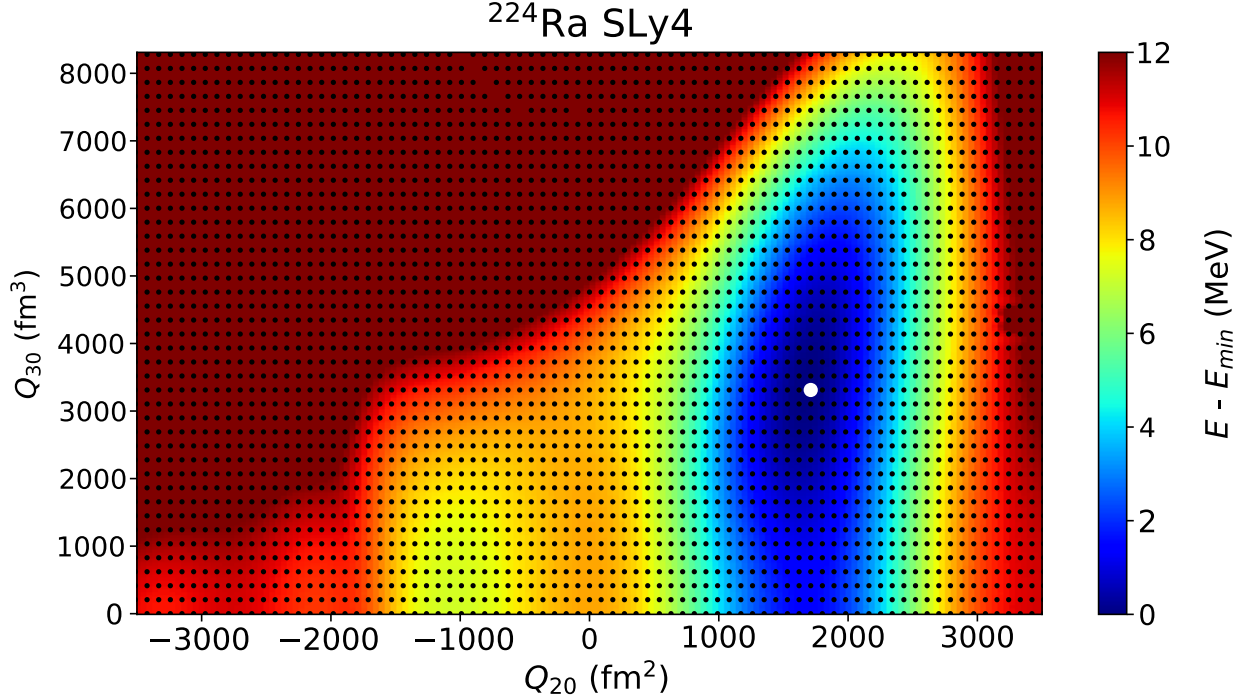
Figure 3.1: Potential energy surface of ^{224}Ra calculated using Skyrme energy density functional SLy4. The white circle marks the lowest binding energy, which serves as the baseline energy value.

Since the size of the grid is finite, values are interpolated in between calculated mesh points. In addition, the finite grid implies that the true g.s. of the system is believed to be in the vicinity of $(Q_{20}^{\text{PES g.s.}}, Q_{30}^{\text{PES g.s.}})$. Thus, one needs to perform an additional unconstrained calculation, by removing the Lagrangian multiplier terms used to constrain the multipole moments, and restart the HFB calculation from the converged g.s. many-body wave functions. Since the HFB equation is rooted in the variational principle, we are guaranteed to find a configuration with a lower energy compared to $\text{BE}^{\text{PES g.s.}}$. This

resulting configuration from the unconstrained calculation is then the true HFB g.s. with deformation $(Q_{20}^{\text{HFB g.s.}}, Q_{30}^{\text{HFB g.s.}})$.

3.1.2 PES grid selection

Ideally, one would choose a PES grid as dense and as large as their time and budget allows. The choice for density of the grids is arbitrary and subject to benchmarks. The PES for a nucleus in a HFB mass-table calculation usually consists around 150 mesh points, as this has been proven effective in finding the HFB g.s. with benchmarks using the two-step constrained + unconstrained method mentioned above.

Very large Q_{20} and Q_{30} values correspond to extreme and unstable shapes in a fission process, where one would not expect a g.s. to be located. This limits the range, or area, of the PES we have to calculate. Although the deformation constraints are imposed on the expectation values of multipole moments using Lagrangian multipliers, these moments scale with the size of the nucleus. For a fixed shape, we have:

$$
\begin{aligned}
Q_{20} &\propto R_0^2 \propto A^{2/3}, \\
Q_{30} &\propto R_0^3 \propto A.
\end{aligned}
\tag{3.1}
$$

Thus, when setting up the PES for a global mass-table calculation that includes masses ranging from 4 to 420, the range of Q_{20} and Q_{30} differs greatly, and instead, one should define the PES grids across all mass ranges using the deformation parameters β_2 and β_3, such that for axially symmetric nuclei with identical β_λ values, their shapes are identical.

In our latest octupole mass-table calculations, the range of β_2 and β_3 is $[-0.35, 0.35]$ and $[0, 0.4]$, respectively, and the step-size 0.05 and 0.1, respectively, creating a PES containing

$15 \times 5 = 75$ (β_{20}, β_{30}) mesh points for each nucleus. In the actual HFB calculations, the β_λ values are converted to the moments $Q_{\lambda 0}$ using Eq. (2.34).

3.1.3 Kick-off mode and characteristics of the calculation

The conventional two-step procedure of finding the nuclear g.s. is cumbersome, in the sense that at every point on the PES we first need to generate a "restart" file, which stores information of the current nuclear configuration in order to start the unconstrained calculations. To save storage, one could perform a PES without creating all the "restart" files, identify the $(Q_{20}^{\text{PES g.s.}}, Q_{30}^{\text{PES g.s.}})$, then redo the constrained calculation for this deformation while allowing it to generate a "restart" file.

An improved solution is to combine the two steps of constrained and unconstrained calculations, and use a so-called kick-off mode. This was introduced in the HFB solver HFBTHO (v2.00d) [77] and subsequently improved in the latest HFBTHO (v3.00) [70], where a derived version from the latter was used to perform our octupole mass-table calculation.

The idea of kick-off mode is to start the HFB calculation with moment constraints, continue this for the first N_{kickoff} iterations or until the convergence criteria $\varepsilon_{\text{kickoff}}$ is met, then release the constraints and allow the HFB calculation to smoothly transit into an unconstrained calculation. By experimenting with the N_{kickoff} and $\varepsilon_{\text{kickoff}}$ parameters, we were able to determine that with $N_{\text{kickoff}} = 20$ and $\varepsilon_{\text{kickoff}} = 1.0$ the number of PES points needed to find the g.s is reduced. This was tested in all bound O, Th and Fm isotopes. One can think of this pre-releasing of the constraints as granting the calculation a sort of "search radius", where the calculation is allowed to iterate in the first 20 steps to find roughly the density configuration near the given constraints, then release the constraints and let the variational principle take us to the minimum. Using too small a N_{kickoff} value does not

"guide" the calculation long enough to get close enough to the initial multipole moments, and using too large a $N_{kickoff}$ value, in the extreme of infinity, is equivalent to the combined two-step procedure, and does not reduce the number of PES points.

The effectiveness of kick-off mode has been throughly tested and benchmarked prior to the global calculations. The adopted mesh is $\beta_2^i \in [-0.35, 0.35]$, $\beta_2^{i+1} - \beta_2^i = 0.05$ and $\beta_3^i \in [0, 0.4]$, $\beta_3^{i+1} - \beta_3^i = 0.1$. This selection reproduces g.s. BE (within 10eV) of all bound nuclei in O, Ca, Gd, Dy, Th, and Fm isotopic chains when compared with PES calculations that use dense populated grids, where the kick-off calculations are able to converge within 200 iterations in most cases. We also performed these kick-off calculations by doubling the number of mesh points in β_2 and β_3, and found no significant decrease in the computed g.s. energies.

Although the kick-off mode is able to reduce the number of points by at least 50%, the disadvantage of kick-off mode is that we can no longer create a PES contour plot such as Fig. 3.1, since the converged calculations have (Q_{20}, Q_{30}) that are randomly spaced and sometimes clustered. However, if one is only interested in the global nuclear g.s. properties, kick-off mode can provide us with a more efficient solution, while providing equally high quality predictions.

Following the completion of the octupole mass-table, we selected nuclei that have zero octupole deformation and then performed reflection-symmetric calculations. The average g.s. BE difference between these benchmarks and the reflection asymmetric octupole mass-tables is 4 eV, with the largest difference at 26 eV, which demonstrates that HFBTHO (v3.00) solver handles the breaking of reflection symmetry with high precision.

The g.s. of each nucleus is selected to be the output that has the lowest binding energy among results from the 75 inputs. In practice, not all inputs will converge, as we limited the

maximum number of HFB iterations to be 1000. In limited cases where the nuclear g.s. come from the HFB calculation that requires more than 1000 iterations, the additional iterations decrease the g.s. BE on the order of 10 eV, which does not justify the cost of increasing the iteration limit.

We limit the number of harmonic oscillator shells in the basis to 20, as increasing this number to 30 shells did not bring any improvements. Out of the 75 (Q_{20}, Q_{30}) points, the percentage of converged mesh points varies between EDFs: UNEDF0 (78%), UNEDF1 (31%), UNEDF2 (62%), SV-min (94%), and SLy4 (95%). We believe this percentage does not have any impact on the quality of the g.s. BE predictions, as one could see in Fig. 3.2 that the rms deviation of BE predicted by UNEDF1 is similar to UNEDF2.
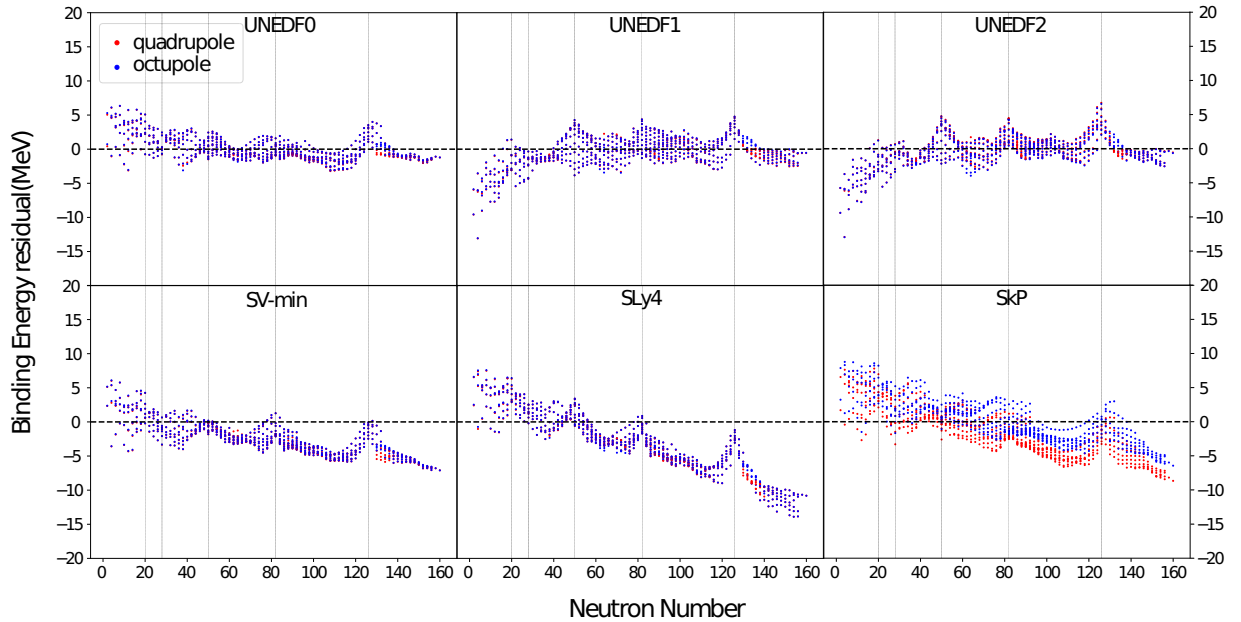
Figure 3.2: Binding energy residuals for Skyrme EDFs UNEDF0, UNEDF1, UNEDF2, SV-min, SLy4, and SkP mass-tables. Red dots are from quadrupole-deformed calculation [98], blue dots are from the current octupole-deformed mass-table. All rms deviations are improved in the latest calculations. The large shift in binding energy residuals in the SkP mass-table is due to the different pairing strengths used in these two calculations. Consequently, results from SkP calculations have not been considered.

In a few cases, the lowest binding energy was obtained at deformations that clearly went

beyond the fission barrier, such as β_2 as large as 1.5. Hence, we discarded all outputs with β_2 and β_3 greater than 0.5. All nuclei with deformation $\beta_2 > 0.4$ have been manually inspected, the ones with $\beta_2 > 0.5$ are prone to have suspiciously low minima, creating sharp kinks in the separation energy. We realize that this is by no means the most rigorous approach to deal with large deformations, as one should look at the PES in each case to be certain, but given the scale of calculation involved we find this compromise reasonable.

Finally, as a reminder, one always need to check if the dipole moment of the nucleus is constrained to zero (Sec. 2.1.4.2), which is essentially requiring the center of mass of the nucleus to be the same as the origin of the intrinsic reference frame.

3.1.4 Computational aspects

The 2836 nuclei in each mass-table, together with the 75 deformation mesh points for each nucleus, resulted in a total of 212,700 entries for each of the five SEDFs. Each entry is itself an individual HFB calculation, which takes anywhere from 10 minutes to 4 hours to complete, with an average of 2 hours for the UNEDF family of SEDFs and 40 minutes for SLy4 and SV-min, using the Intel Xeon E5-2680 processor at iCER [106]. This puts us at roughly 2 million CPU-hour for these five mass-tables and their related benchmarks. Although HFBTHO (v3.00) has OpenMP capability, no OpenMP were used in these global study as we would like to achieve 100% efficiency.

Adjustments to the MPI of HFBTHO (v3.00) was made. The parallel mass-table mode is now modified to allow for octupole deformation constraints in the input file. The default MPI uses the static scheduling scheme, where each MPI task will be assigned a fixed set of grids to calculate at the beginning of a parallel run. This quickly proves to be inefficient for global calculations, since the total time needed for all MPI tasks is determined by the slowest

MPI task. Additionally, in almost every batch of computation (1000 MPI tasks), there will be task that freezes, likely caused by hardware issues, creating further complications. We have thus replaced this static scheduling scheme with dynamic scheduling, where a MPI task was designated as a manager. Once a worker task completes its calculation and becomes available, it would send a message to a manager to acquire a new task. In this dynamic scheduling scheme, the worst-case scenario was for all MPI tasks to wait for one single tasks to complete. This greatly reduced the load imbalance in this large-scale computation.

By implementing dynamic scheduling, according to conservative estimates, roughly 50% of computational cost was saved. Together with the reduced PES sizes required by using the kick-off mode, an estimated 6 million CPU-hours were saved at the conclusion of our octupole project.

3.2   Global results

3.2.1   Comparison with the 2012 quadrupole survey

Figure 3.2 is the BE residual (difference with respect to experimental masses from AME2016 [99]) obtained in the current octupole mass-tables (blue dots) and the 2012 quadrupole mass-tables (red dots) [98]. The overall rms error and the improvements are in units of MeV. For UN-EDF0, UNEDF1, UNEDF2, SLy4, and SV-min a slight improvement in the rms error has been obtained, likely due to the additional octupole degree of freedom; this can be seen in the separation of blue and red dots around $N = 130$, which is where most of the octupole-deformed nuclei are located. The octupole mass-table of SkP (lower right) and SkM* (not displayed here) was left out of the current study due to the dramatic improvement in the rms error compared with their 2012 mass-table [98]. This improvement is clearly systematic,

and not just in the octupole-deformed region. We believe this has been caused by different pairing parameters used than the previous mass-table. Unfortunately, since the original pairing parameters of SkP and SkM* used for the 2012 mass-table [98] could not be retrieved, and the currently used pairing parameters have not been benchmarked, we decided to leave these two SEDFs out of the current study. The pairing strengths for SLy4 and SV-min were assumed to be -258.2 MeV and -214.28 MeV, respectively, assuming the same value for neutrons and protons, consistent with the 2012 mass-table [98].
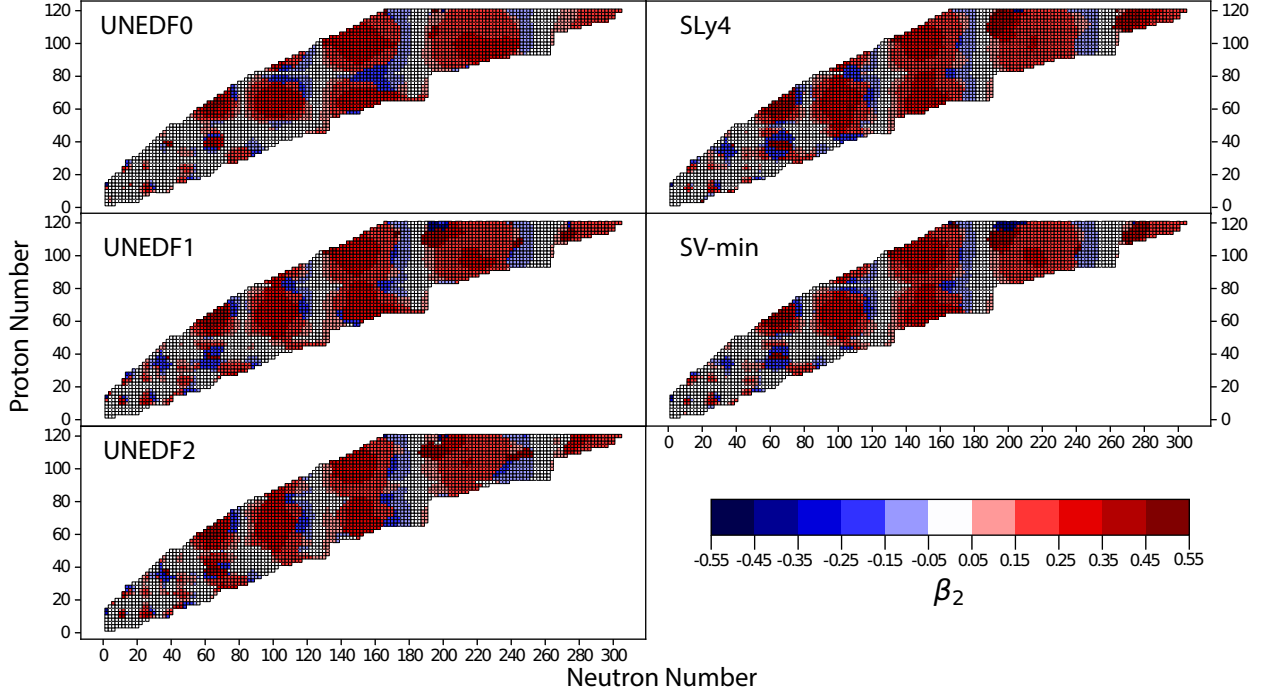
Figure 3.3: Total g.s. quadrupole deformation β_2 of even-even nuclei in the (Z, N) plane predicted with the SEDFs UNEDF0, UNEDF1, UNEDF2, SLy4, and SV-min from the current reflection-asymmetric calculations. Spherical shell closures can be easily seen.

Figure 3.3 shows the landscape of quadrupole deformation from the our calculations (note: unbound nuclei have not been removed from this figure). The prediction of quadrupole deformation is identical to the 2012 survey, which can be found on MassExplorer [107], a data distribution platform for theoretical nuclear data of our research group. In most

cases, the Q_{20} values obtained in the reflection-symmetric calculations are similar to that in our reflection-asymmetric calculations, which could also be seen in the example of Fig. 3.1. However, in rare cases, particularly near the end of the range of octupole deformation in an isotopic chain, this is not guaranteed, as the octupole minimum becomes shallower.

3.2.2 Octupole deformation β_3

The g.s. octupole deformations β_3 obtained in our calculations are displayed in Fig. 3.4. There is a good inter-model consistency, with large octupole deformations predicted around ^{146}Ba (neutron-rich lanthanides), ^{200}Gd (very neutron-rich lanthanides), ^{224}Ra (neutron-deficient actinides), and ^{288}Pu (neutron-rich actinides), i.e., in the regions of strong octupole collectivity defined by the presence of close-lying proton and neutron shells with $\Delta\ell = \Delta j = 3$ [21]. This finding is consistent with previous global studies [4, 25, 31, 34, 36].

In each region of octupole-deformed nuclei, the magnitude of octupole deformation increases with the number of valence nucleons. All five SEDFs predict neutron-deficient and neutron-rich actinides to exhibit strong octupole deformations, while predictions in the lanthanide region are less uniform regarding which nuclei are deformed and how deformed they are. In general, UNEDF2 and SLy4 predict the largest number of octupole-deformed nuclei and also larger values of β_3. In both models, proton-rich nuclei around ^{112}Ba are expected to be reflection-asymmetric. The functional UNEDF0 predicts the least amount of octupole-deformed nuclei and smaller β_3 deformations overall.
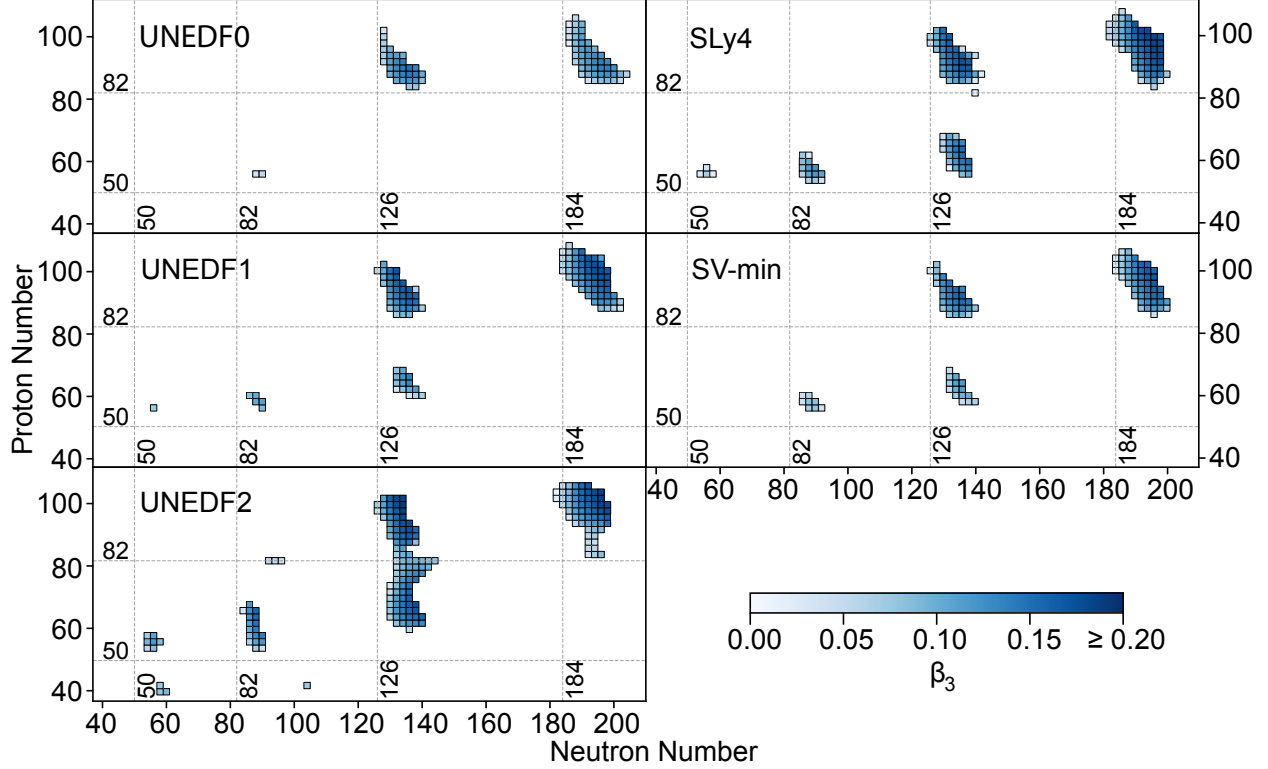
Figure 3.4: Total g.s. octupole deformations β_3 of even-even nuclei in the (Z, N) plane predicted with the SEDFs UNEDF0, UNEDF1, UNEDF2, SLy4, and SV-min. The magic numbers are indicated by dashed lines. (Figure taken from Ref. [92])

3.2.3 Octupole deformation energy ΔE_{oct}

The magnitude of octupole deformation, i.e. β_3, alone is insufficient in determining whether robust octupole deformation is present since it does not provide any information on the softness of the potential energy surface in the octupole direction. To address this point, we also look at the gain in binding energy ΔE_{oct} due to octupole deformation:

$$\Delta E_{\mathrm{oct}} = E^{\mathrm{a}}\left(\beta_2, \beta_3\right) - E^{\mathrm{s}}\left(\beta_2', \beta_3' = 0\right), \tag{3.2}$$

where E^{a} is the absolute binding energy obtained in reflection-asymmetric calculations, and E^{s} is the binding energy minimum from reflection-symmetric calculations. These two minima do not necessarily have the same quadrupole deformation, but as mentioned in Sec. 3.2.1,

they are expected to be very close.
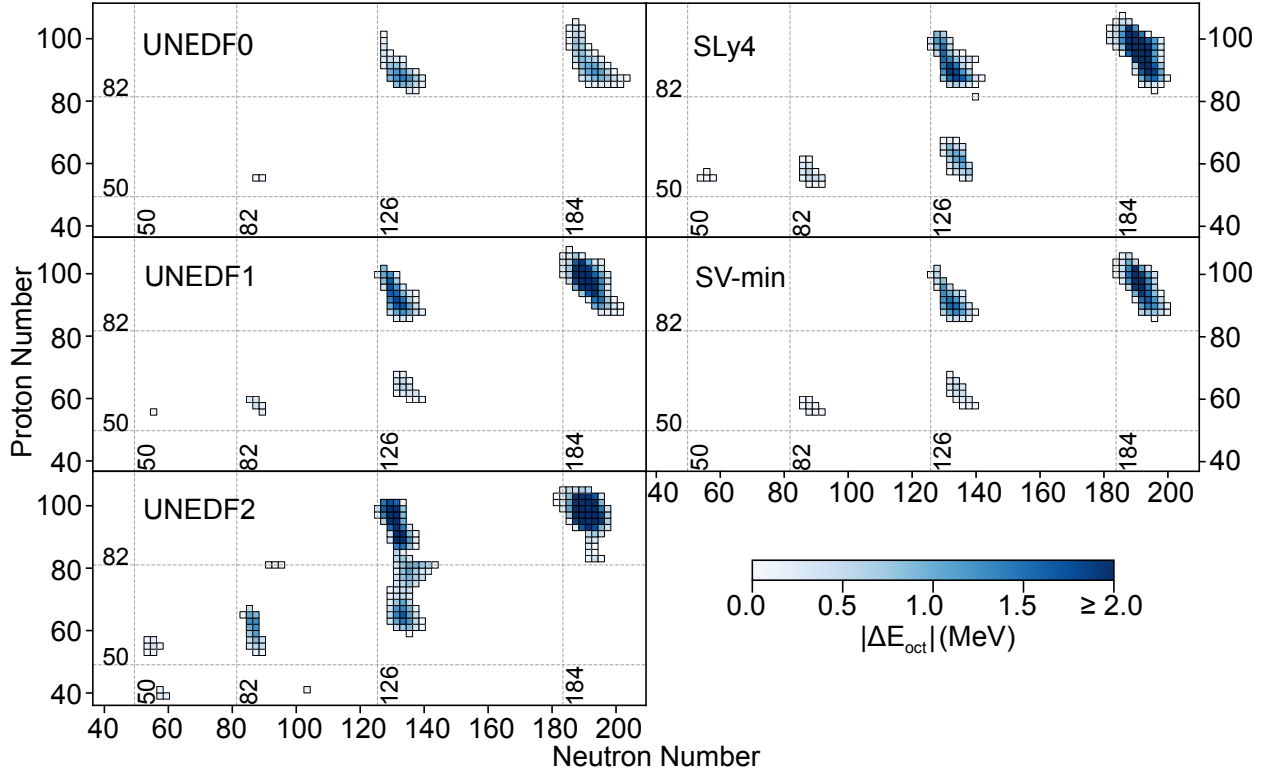
Figure 3.5: Similar to Fig. 3.4 but for the octupole deformation energy ΔE_{oct}. (Figure taken from Ref. [92])

The octupole deformation energies ΔE_{oct} predicted in our mass-table calculations are shown in Fig. 3.5. We can see that lanthanide nuclei have appreciably smaller ΔE_{oct} values as compared to the actinides in spite of similar octupole deformations. This indicates that most of the reflection-asymmetric lanthanide nuclei are predicted to have very soft PESs in the octupole direction, regardless of the equilibrium value of β_3.

The values of ΔE_{oct} and β_3 of nuclei with at least three SEDFs predicting it as octupole-deformed are displayed in Table A.1.

3.2.4 Octupole multiplicity: Joint analysis with covariant EDFs

In an effort to obtain a more robust picture of octupole deformations, we combined the oc-tupole predictions from our five SEDFs calculated using the HFB method and four covariant energy density functionals (CEDFs) DD-ME2 [54], DD-PC1 [57], NL3* [55], and PC-PK1 [56] using the relativistic Hartree-Bogoliubov method (RHB), in Fig. 3.6. Most of the CEDFs results can be found in Ref. [35]. We define the model multiplicity $m(Z, N) = k$ if a nu-cleus (Z, N) is predicted by k models ($k = 1, \dots 9$) to have a nonzero octupole deformation. Nuclei predicted by all nine EDFs as octupole-deformed (i.e., $m = 9$) are shown by stars. These are: ^{146}Ba, ^{224,226}Ra, ^{226,228}Th, and ^{228}Pu in the regions experimentally accessible; ^{288,290}Pu, ^{288,290}Cm, and ^{288,290}Cf in the very neutron-rich actinides region. Apart from the overall agreement between SEDFs and CEDFs when it comes to the predicted regions of octupole-instability, we see systematic shifts (by 2-4 neutrons) between the regions of $\Delta E_{\rm oct}$ and β_3 obtained by these two energy density functionals (EDF) families. This systematic effect is illustrated in Fig. 3.7, where dots mark the SEDFs' predictions with $m \geq 3$, squares show the CEDFs' predictions with $m \geq 2$, and diamonds mark the overlap of the two. This shift has been noticed in Ref. [35] pertaining to superheavy nuclei.

3.2.5 Single particle orbitals in octupole-deformed regions

Microscopically, octupole deformations can be traced back to close-lying pairs of single-particle (s.p.) shells coupled by the octupole field [21]. Each pair consists of the unusual-parity intruder shell (ℓ, j) and the normal-parity shell $(\ell - 3, j - 3)$. Consequently, the regions of nuclei with strong octupole correlations correspond to particle numbers near 34 ($g_{9/2} \leftrightarrow p_{3/2}$ coupling), 56 ($h_{11/2} \leftrightarrow d_{5/2}$), 88 ($i_{13/2} \leftrightarrow f_{7/2}$), 134 ($j_{15/2} \leftrightarrow g_{9/2}$), and 196
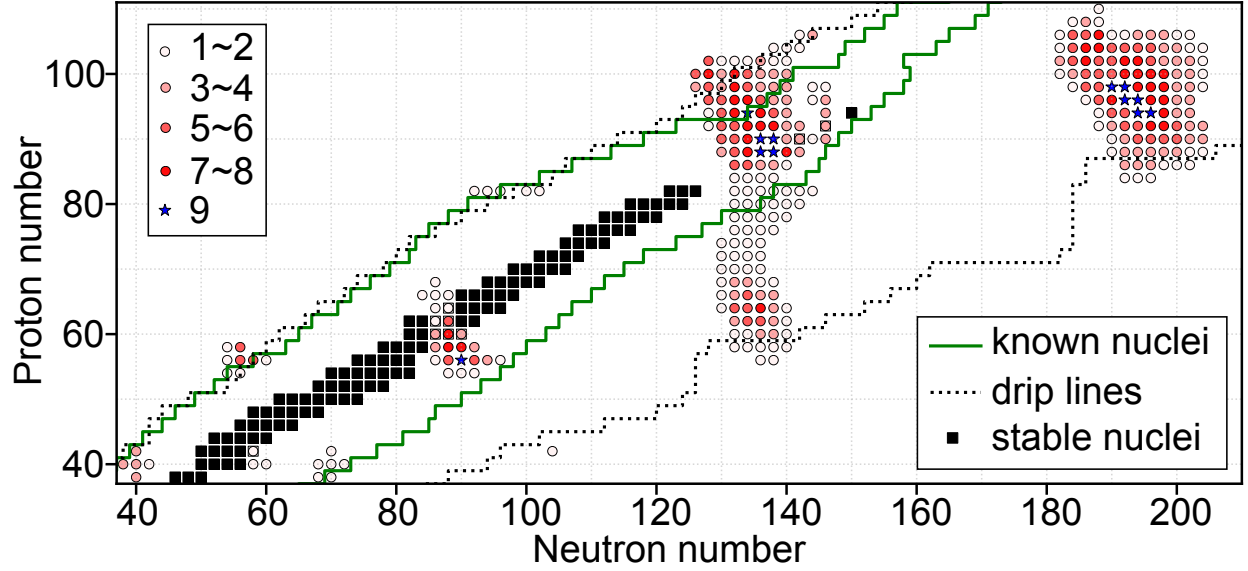
Figure 3.6: The landscape of g.s. octupole deformations in even-even nuclei. Circles and stars represent nuclei predicted to have nonzero octupole deformations. The model multiplicity $m(Z, N)$ is indicated by the legend. The boundary of known (i.e., experimentally discovered) nuclei is marked by the solid green line. For simplicity, this boundary is defined by the lightest and heaviest isotopes discovered for a given element. The average two-nucleon drip lines from Bayesian machine learning studies [108, 109] are marked by dotted lines. Primordial nuclides [110] are indicated by squares. (Figure taken from Ref. [92])
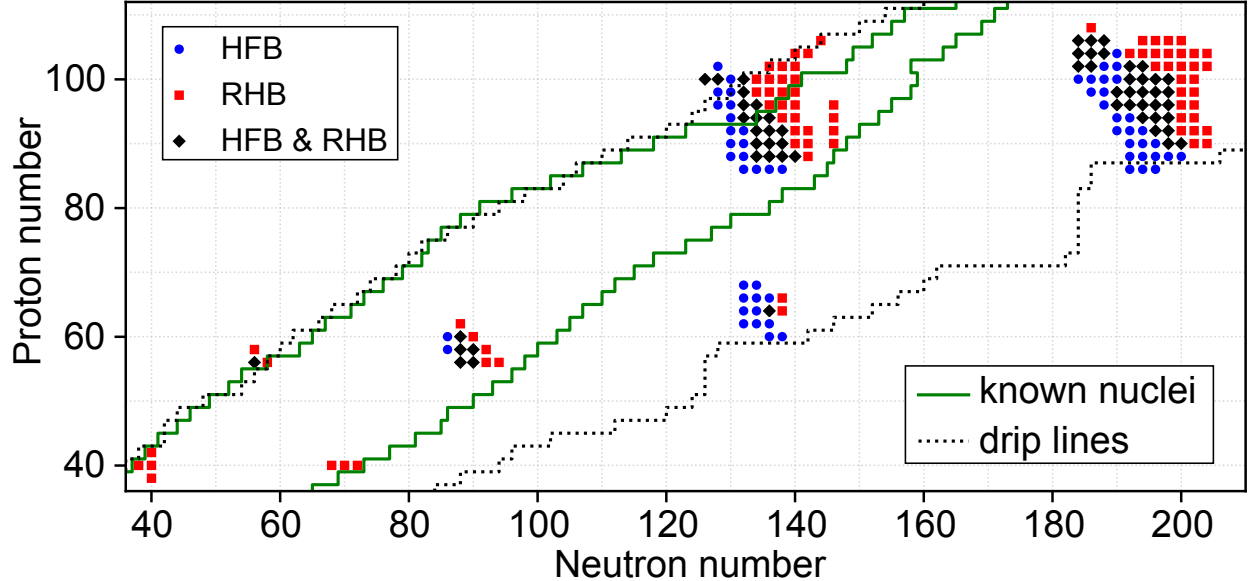
Figure 3.7: Comparison between SEDFs and CEDFs predictions. Dots mark the SEDFs predictions with $m \geq 3$, squares show the CEDFs predictions with $m \geq 2$, and diamonds mark the overlap region between SEDFs and CEDFs results. The borders of known nuclei and two-particle drip lines are as in Fig. 3.6. (Figure taken from Ref. [92])
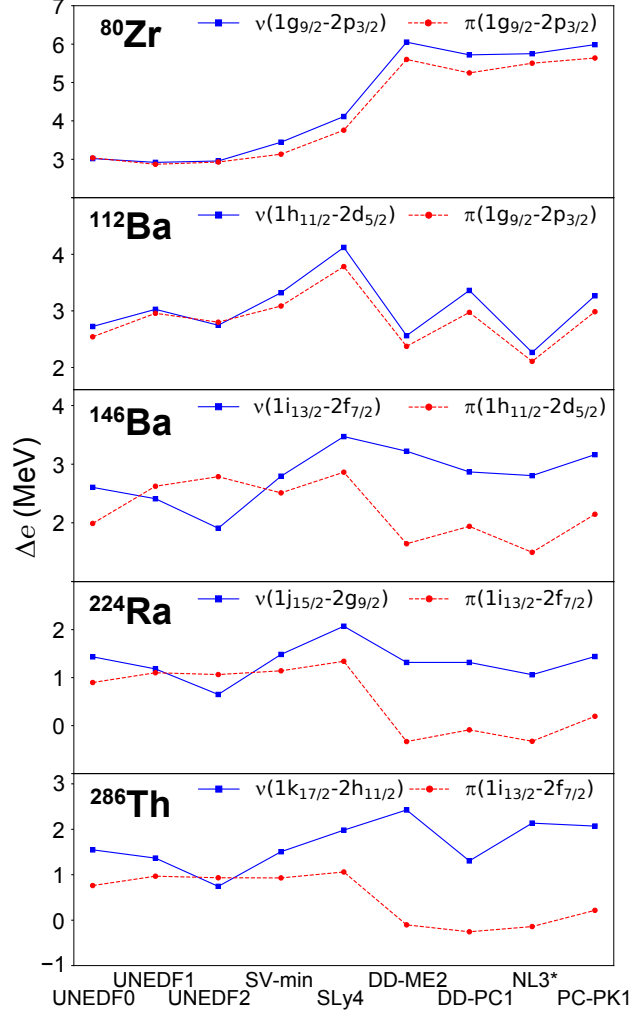
Figure 3.8: Single-particle energy splitting Δe between the unusual-parity intruder shell (ℓ, j) and the normal-parity shell $(\ell - 3, j - 3)$ for five nuclei representing different regions of octupole instability. The s.p. canonical states were obtained from spherical HFB/RHB calculations. The neutron (proton) splittings are indicated by the solid (dashed) lines. (Figure taken from Ref. [92])

$(k_{17/2} \leftrightarrow h_{11/2})$.

Figure 3.8 shows the energy splitting

$$\Delta e = e(\ell, j) - e(\ell - 3, j - 3), \tag{3.3}$$

between s.p. canonical shells obtained from spherical HFB/RHB calculations. In general,

there is a systematic decrease of Δe with mass, which – together with the increased degeneracy of s.p. orbits (and matrix elements of the octupole coupling) – results in enhanced octupole correlations in heavy nuclei. However, while this general trend is robust, the magnitude of Δe is not a good indicator of octupole correlations when comparing different models.

Indeed, when comparing different models one also needs to consider other factors related to each model's structure. For instance, the isoscalar effective mass of SLy4 is close to 0.7, which effectively increases the s.p. splitting as compared to UNEDF models (which have effective mass close to one). As a result, although in most cases SLy4 has larger Δe than UNEDF1, it predicts more octupole-deformed nuclei and larger ΔE_{oct} values. It is safer and more instructive to compare predictions of the UNEDF family of SEDFs, as their properties are not very different. Here, the UNEDF2 parametrization, constrained to the spin-orbit splittings in several nuclei, yields the lowest values of Δe for neutrons and predicts the strongest octupole correlations, see Figs. 3.5 and 3.6.

3.3 Local regions of octupole ground-state deformations

The majority of nuclei with g.s. octupole deformation are found near the intersection between neutron numbers 88, 134, and 194 and proton numbers 56 and 88. This pattern is more pronounced in heavy nuclei, due to their lower values of Δe, see Fig. 3.8.

I will be discussing the octupole collectivity in the actinide region ($Z \approx 88$) in section 3.3.1, and the lanthanide region ($Z \approx 56$) in section 3.3.2 , with a focus on the cases robustly predicted to be octupole-deformed in our SEDF calculations. Our SEDFs' results will be compared with octupole predictions using other theoretical methods: macroscopic-microscopic (MM) method using FRLDM interaction [22], generator coordinate method

(GCM) using Gogny interaction [23], Hartree-Fock + BCS (HF+BCS) method with Skyrme interaction SkM* [3], and the RHB method discussed earlier (Sec. 3.2.4). Except for the MM approach [22] that made predictions for odd-odd and odd-A nuclei, all other mentioned methods are calculated for even-even nuclei only.

We note that all EDFs used in this study provide robust and consistent predictions for quadrupole moments, which generally agree well with available experimental data [111–113]. This suggests that the quadrupole collectivity is well developed. On the other hand, in many nuclei, the octupole deformation energy has a modest value of less than 500 keV. Such small values of ΔE_{oct} indicate soft PESs resulting in the octupole collectivity of transitional character, i.e., between octupole rotational and vibrational collective motions [21]. While in this work we refer to a nucleus as octupole-deformed when it has $\beta_3 \neq 0$, this does not mean that this octupole deformation is static. For octupole-soft, transitional nuclei, beyond mean-field methods are needed to describe the system [26, 28, 29, 36, 114–117].

3.3.1 Actinide region

Because of large octupole correlation effects and experimental accessibility, neutron-deficient actinides have traditionally been in the spotlight of octupole deformation studies. As seen in Fig. 3.6, this region is expected to be abundant in octupole-deformed nuclei, with many systems predicted robustly by several models, i.e., having high octupole multiplicity.

3.3.1.1 Radon ($Z = 86$)

The isotopes ^{218,220}Rn and ^{224,226}Rn have been found experimentally to be close to the octupole vibrational limit [111, 118–120]. As seen in Fig. 3.9, $|\Delta E_{\mathrm{oct}}|$ reaches its maximum for ^{220}Rn, with an average value around 0.5 MeV. These shallow octupole minima suggest that
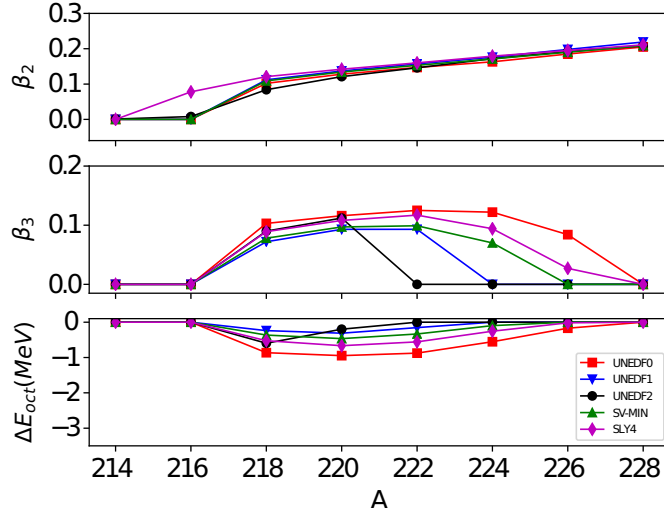
Figure 3.9: Predicted β_2, β_3, and ΔE_{oct} values for even-even Rn ($Z = 86$) isotopes.

neutron-deficient Rn isotopes are transitional systems, consistent with experiment. Interestingly, UNEDF0 predicted the largest $|\Delta E_{\text{oct}}|$ for Rn isotopes among the SEDFs. As we shall see later, UNEDF0 tends to predict the smallest $|\Delta E_{\text{oct}}|$ for other robust octupole-deformed nuclei.

More than half of the SEDFs predicted $^{218-224}$Rn as octupole-deformed, as well as GCM [25] and MM [4], where the latter extended its octupole prediction all the way to ^{232}Rn. The HF+BCS model [31] reported ^{220,222}Rn in their octupole list. No octupole deformation is predicted by CEDFs for Rn isotopes in Ref. [34].

3.3.1.2 Radium ($Z = 88$)

The search for octupole instability in neutron-deficient Ra isotopes has been of great interest [22, 111, 121], also because of atomic EDM studies [122, 123]. According to numerous theoretical calculations, ^{224}Ra has the largest octupole deformation [22, 121], and is often predicted to have the largest ΔE_{oct} among the Ra isotopes. It is therefore hardly surprising that ^{224}Ra, along with ^{226}Ra, is predicted to be octuple-deformed by all nine EDFs studied.
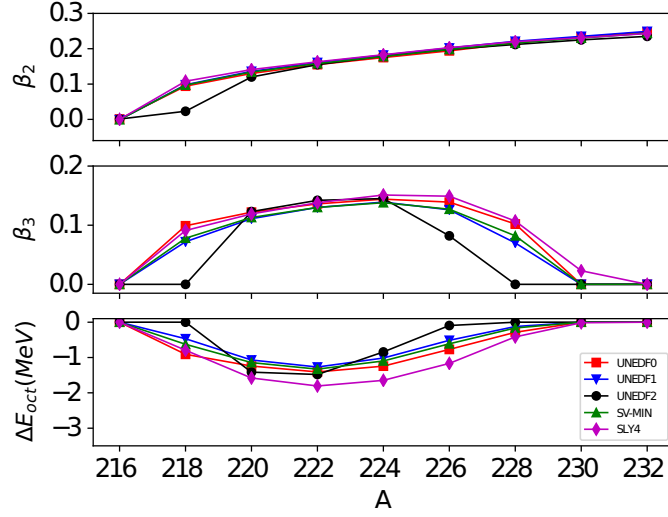
Figure 3.10: Predicted β_2, β_3, and ΔE_{oct} values for even-even Ra ($Z = 88$) isotopes.

Within the SEDFs, the values of Predicted β_2, β_3, and ΔE_{oct} values appear to be very consistent for ^{220,224}Ra, cf. Fig. 3.10. The largest $|\Delta E_{\text{oct}}|$ is predicted for ^{222}Ra, followed by ^{220}Ra and ^{224}Ra. In CEDFs predictions, $|\Delta E_{\text{oct}}|$ is largest for ^{224}Ra due to the shift in neutron numbers discussed earlier (Sec. 3.2.4).

Even-even $^{222-230}$Ra are calculated by at least half of the CEDFs to be octupole-deformed. Both MM [4] and GCM [25] models reported octupole moments in even-even $^{218-228}$Ra, in complete agreement with the majority of the SEDFs; HF+BCS [31] reported ^{222,224}Ra as octupole-deformed.

Recent experiments suggest ^{222}Ra has the largest octupole deformation among the Ra isotopes followed by ^{226}Ra, ^{228}Ra, and ^{224}Ra [112, 121, 124]. Figs. 3.11 and 3.12 show the proton Q_{20} and Q_{30} from our SEDFs' predictions compared with charge multipole moments derived from experimental data. The sudden drop in the proton Q_{20} of ^{224}Ra is predicted by none of the SEDFs and CEDFs, and currently we do not have any theoretical explanation for this effect. Additional measurements might be needed to confirm this particular behavior.
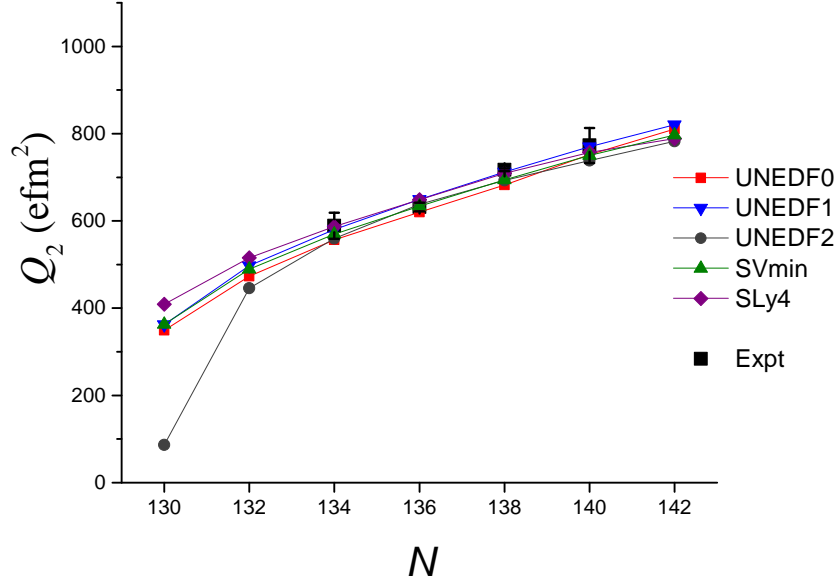
Figure 3.11: Proton Q_{20} of Ra isotopes from SEDFs calculations (see Table A.2 for a comprehensive list of values) compared with measured $E2$ intrinsic moments Q_2 for $2^+ \rightarrow 0^+$ transitions (black squares with error bars) of Ref. [111–113, 124]. (Figure taken from Ref. [125])
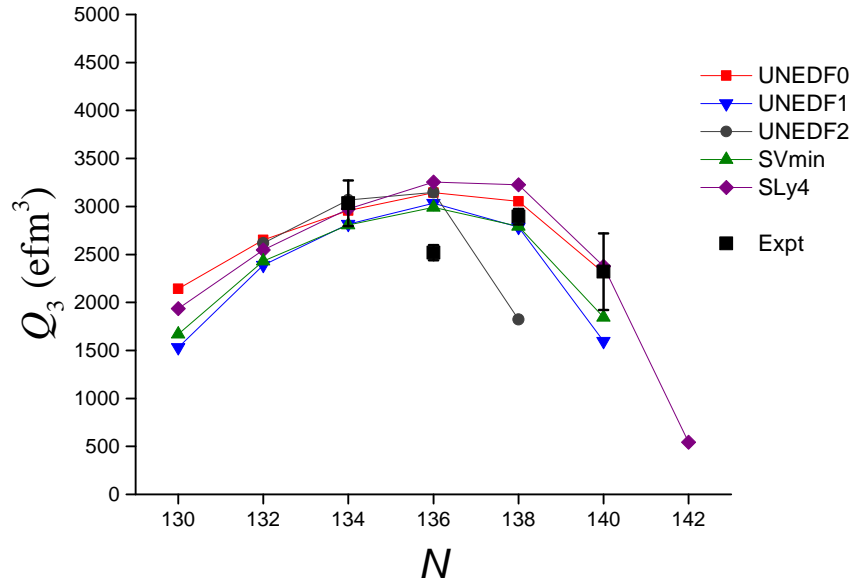
Figure 3.12: Proton Q_{30} of Ra isotopes from SEDFs calculations (see Table A.2 for a comprehensive list of values) compared with measured $E3$ intrinsic moments Q_3 for $3^- \rightarrow 0^+$ transitions (black squares with error bars) of Ref. [111, 112, 121, 124]. (Figure taken from Ref. [125])

Proton Q_{20} and Q_{30} values for octupole-deformed even-even nuclei from SEDFs predictions are compiled in Table A.2.

3.3.1.3   Thorium ($Z = 90$)
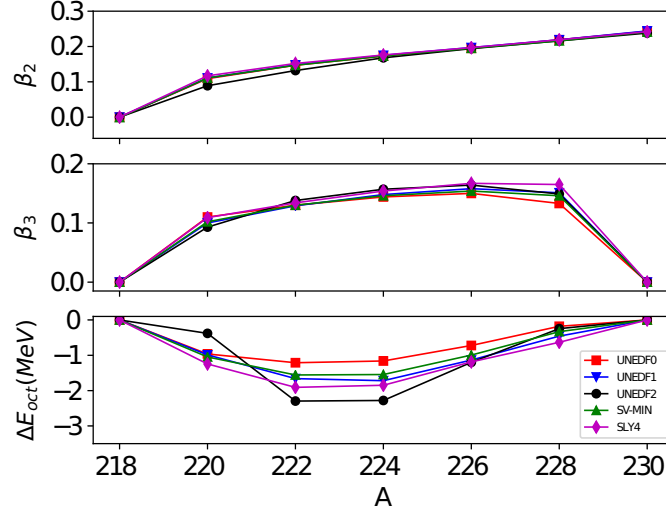
Figure 3.13: Predicted β_2, β_3, and ΔE_{oct} values for even-even Th ($Z = 90$) isotopes.

Experimentally, even-even $^{222-226}$Th exhibit many signatures of stable octupole deformation [118, 126, 127], in agreement with the SEDFs' predictions shown in Fig. 3.13. All SEDFs predict octupole deformations in even-even $^{220-228}$Th. These nuclei are identical to MM [4] and GCM [25] predictions, while HF+BCS [31] only reported ^{220,222}Th as octupole deformed. The CEDFs models [34] predicted octupole deformation in even-even $^{224-232}$Th, a shift of four neutrons compared to the SEDFs. From our SEDFs calculation, we predict the nucleus ^{222}Th and ^{224}Th to have strong g.s. octupole deformation.

3.3.1.4   Uranium ($Z = 92$)

The majority of SEDFs predict even-even $^{222-228}$U to be octupole-deformed. As seen in Fig. 3.14, the largest octupole deformation energy exceeding $2\,\text{MeV}$ is calculated for ^{224}U,
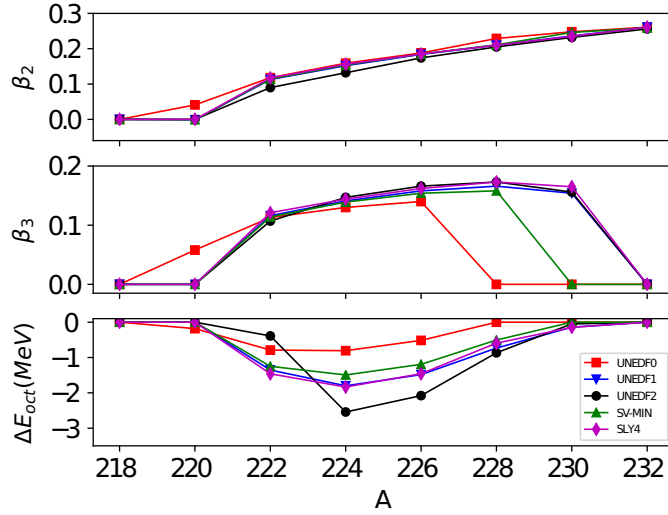
Figure 3.14: Predicted β_2, β_3, and ΔE_{oct} values for even-even U ($Z = 92$) isotopes.

followed by ^{222,226}U. Experimentally, the nucleus ^{226}U has similar octupole characteristics as ^{222}Ra and ^{224}Th [128].

MM [4] predicted the octupole-deformed U isotopes to be $^{220-226}$U, GCM [25] listed $^{222-232}$U and HF+BCS [31] listed ^{220,224,226}U as octupole-deformed. The CEDFs [34] predicted octupole deformations in $^{226-234}$U.

According to our SEDFs study, the nuclei ^{222,224,226}U are strong candidates for pear-shaped deformations, with ^{224}U being most promising.

3.3.1.5 Plutonium ($Z = 94$)

Neutron-deficient Pu isotopes have received little attention in experimental searches for octupole instability as they are extremely difficult to access. The lightest-known Pu isotope, ^{228}Pu, has a half-life of $1.1\,\text{s}$ [129] but spectroscopic information about this system is nonexistent. Likewise, virtually nothing is known about ^{230,232,234}Pu, except for their g.s. properties [110]. Interestingly, the isotope ^{228}Pu is predicted by all our models to be octupole-deformed, followed by ^{226}Pu ($m = 7$) and ^{230}Pu ($m = 8$) (see Fig. 3.6). The large
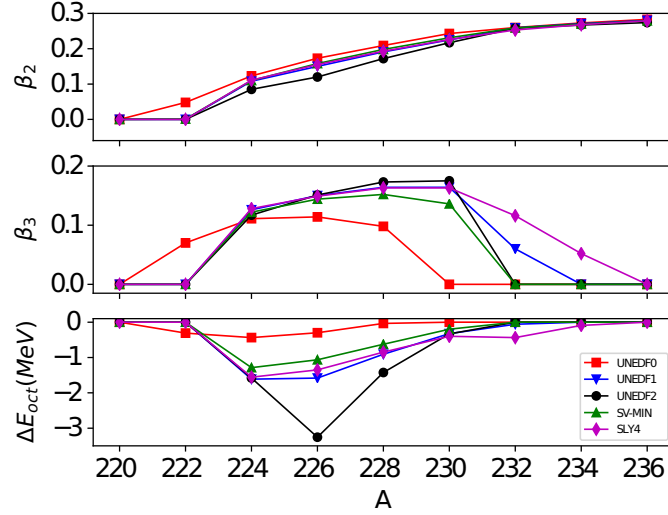
Figure 3.15: Predicted β_2, β_3, and $\Delta E_{\rm oct}$ values for even-even Pu ($Z = 94$) isotopes.

values of $|\Delta E_{\rm oct}|$ in ^{224,226,228}Pu (Fig. 3.15) calculated by SEDFs are similar to those Ra, Th, and U isotopes that show evidence for stable octupole deformations.

The GCM study [25] listed $^{228-234}$Pu as octupole-deformed, while MM model [4] reported $^{222-228}$Pu, with the largest $|\Delta E_{\rm oct}| = 1.09$ MeV in ^{224}Pu. The majority of the CEDFs of Ref. [34] predicted even-even $^{228-232}$Pu as octupole-deformed.

The lightest Cm isotope known experimentally is ^{233}Cm, which is significantly heavier than our most promising Cm candidates for pear-like shapes: ^{228,230}Cm. As seen in Fig. 3.6, in neutron-deficient actinides with $Z \geq 98$, most of the best candidates for octupole deformation lie well beyond the current discovery range, and some appear to be close, or outside, the predicted two-proton drip line [108].

3.3.1.6 Very neutron-rich actinides around ^{288}Pu

Many extremely neutron-rich actinide and transactinide nuclei with $184 < N < 206$ are predicted to be pear-shaped, see Fig. 3.6, Table A.1, and Refs. [27, 30, 33, 35]. From a purely nuclear structure perspective, this broad region of octupole instability is of solely theoretical

interest as it lies well outside experimental reach. While the production of nuclei heavier than $N = 184$ in the astrophysical r process is expected to be strongly hindered by neutron-induced fission [104, 130], the magnitude of this suppression strongly depends on predicted fission barriers [131] and hence the question of their astrophysical relevance is still open.

3.3.2 Lanthanide region

The region of Ba, Ce, Nd, and Sm isotopes around ^{146}Ba constitutes the second largest concentration of octupole-unstable nuclei predicted theoretically that are within the current experimental range.

3.3.2.1 Barium ($Z = 56$)
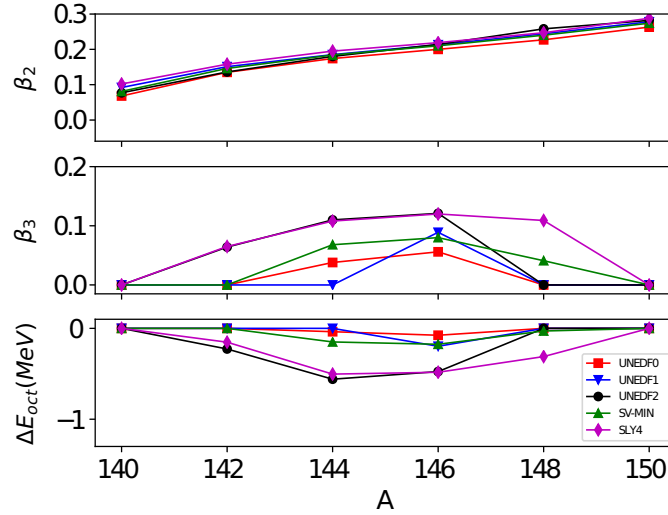
Figure 3.16: Predicted β_2, β_3, and ΔE_{oct} values for even-even Ba ($Z = 56$) isotopes.

Intrinsic dipole moment measurements indicate appreciable octupole correlations in even-even $^{140-148}$Ba [132–135]. In particular, direct measurements of E3 transition strength made recently in ^{144}Ba and ^{146}Ba ($48\left(^{+25}_{-34}\right)$ W.u. and $48\left(^{+21}_{-29}\right)$ W.u., respectively) [136,137]

suggest similar octupole correlations in these nuclei (within large experimental uncertainties). As seen in Fig. 3.16, except for UNEDF1, the SEDF results are consistent with this finding, as they predict similar β_3 and ΔE_{oct} for these systems.

The MM [4] and HF+BCS model [31] calculations also predicted similar β_3 in ^{144}Ba and ^{146}Ba. Although GCM calculation did not directly report β_3 values, they predicted $^{142-148}$Ba as octupole-deformed. The CEDFs predicted similar large β_3 and $|\Delta E_{\mathrm{oct}}|$ values between ^{146}Ba and ^{148}Ba.

3.3.2.2 Cerium $(Z = 58)$
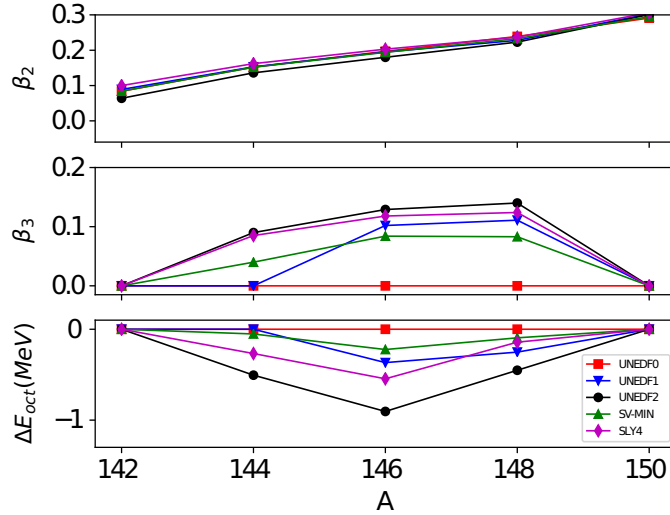
Figure 3.17: Predicted β_2, β_3, and ΔE_{oct} values for even-even Ce $(Z = 58)$ isotopes.

For the Ce isotopes, all SEDFs except for UNEDF0 predict octupole deformations in ^{146,148}Ce, with the largest $|\Delta E_{\mathrm{oct}}|$ in ^{146}Ce, see Fig. 3.17. Experiment suggests enhanced octupole correlations in ^{146}Ce [138], ^{144}Ce [134, 138], and ^{148}Ce [139], and a weakened octupole collectivity in ^{150}Ce [140].

Similar to our results, MM [4] also predicts the maximum $|\Delta E_{\mathrm{oct}}|$ value for ^{146}Ce, at 0.46MeV. GCM [25] predicts $^{144-148}$Ce to be octupole-deformed, and ^{144,146}Ce from

HF+BCS [31]. Again, the CEDFs predict similar results except for a shift of two neutrons.

3.3.2.3 Neodymium ($Z = 60$)
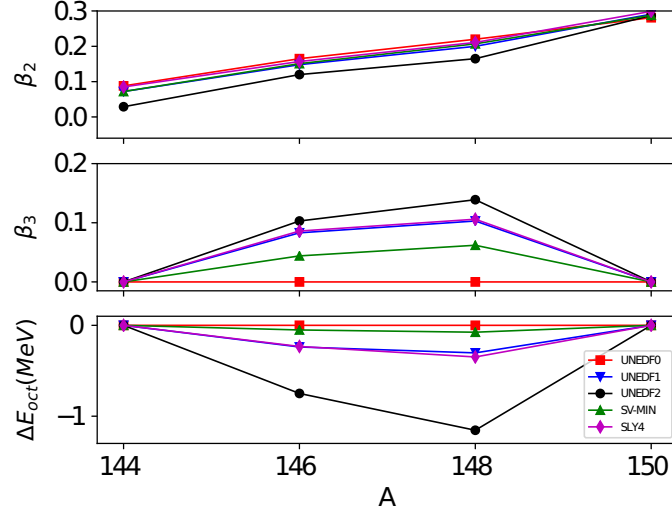
Figure 3.18: Predicted β_2, β_3, and ΔE_{oct} values for even-even Nd ($Z = 60$) isotopes.

The stable isotopes ^{146,148}Nd are predicted to be octupole-deformed (Fig. 3.18 and 3.6). Experimental data suggests enhanced octupole collectivity in ^{146,148,150}Nd [141–145]. Another stable isotope with predicted high octupole multiplicity is ^{150}Sm. Experimentally, there is some evidence for octupole collectivity in an excited band of ^{150}Sm [146]. As seen in Fig. 3.6, the isotopes ^{146,148,150}Nd and ^{150}Sm are the only stable even-even candidates for octupole instability. The parity doublets in odd-mass nuclei from this region, such as ^{153}Eu, can be excellent candidates for searches of T,P-violating effects with atoms, ions, and molecules [147].

3.3.2.4 Proton-rich nuclei around ^{112}Ba

Strong octupole correlations, including octupole instability, were predicted theoretically in nuclei around ^{112}Ba in the early 1990s [148, 149]. As seen in Fig. 3.6, some of our models

yield reflection-asymmetric shapes in a handful of nuclei from this region that lie close to, or beyond, the proton drip-line, with ^{112}Ba being the best candidate.

The experimental data in this region are scarce, with enhanced octupole correlations suggested for ^{112}Xe [150] and ^{114}Xe [151]. The lightest observed Ba isotope is ^{114}Ba [152], for which no spectroscopic information exists.

Shallow octupole minima are calculated in the Zr region around $N = 40$ and $N = 70$ by some CEDFs (Fig. 3.7), and also by GCM calculations [25]. On the other hand, our calculations predict no octupole instability in this region.

3.3.2.5   Very neutron-rich lanthanides around ^{200}Gd

Many extremely neutron-rich nuclei around ^{200}Gd are predicted to be octupole-deformed, see Fig. 3.6 and Table A.1. While this region lies well outside experimental reach, the nucleosynthesis calculations suggest that it can be accessed in a very neutron-rich r-process [153]. The best candidates for octupole instability in this region are ^{196,198,200}Sm, ^{196,198,200}Gd, and ^{200}Dy.

3.4   Summary: Octupole-deformed nuclei

In this chapter, we discussed the standard techniques of finding the Hartree-Fock-Bogoliubov g.s. of the even-even nuclei, and the optimization of the global survey calculation using kick-off mode and dynamic MPI scheduling which reduced the computational cost to 25% of the original estimate.

Among the five SEDFs employed in this global survey of octupole deformation, UNEDF2 and SLy4 predict the largest number of octupole-deformed nuclei, and also the largest oc-

tupole deformation energies $|\Delta E_{\text{oct}}|$. The functional UNEDF0, which was not optimized to experimental shell gaps, predicts the lowest number of octupole minima. This can be attributed to the larger energy splitting Δe between octupole-driving (ℓ, j) and $(\ell - 3, j - 3)$ shells in this model (Fig. 3.5).

The combined prediction from our five SEDFs and four CEDFs functionals of Ref. [34] are shown in the multiplicity plot Fig. 3.6, by combining multiple predictions across different theoretical frameworks.

There are 12 even-even nuclei predicted by all nine EDFs to be octupole-deformed: ^{146}Ba, ^{224,226}Ra, ^{226,228}Th, ^{228}Pu, ^{288,290}Pu, ^{288,290}Cm, and ^{288,290}Cf.

By analyzing the trend of predicted β_2, β_3, and ΔE_{oct} values along isotopic chains of actinides and lanthanides, we found that the SEDF results are fairly consistent with other studies [4, 25, 26]. A shift in the position of octupole-unstable regions (by 2-4 neutron numbers) is seen when comparing SEDFs and CEDFs results. This shift can be seen in Fig. 3.7, and likely comes from the shell structure obtained with CEDF models, as the SEDFs results agree well with the results of other global non-relativistic surveys.

Minor differences aside, the octupole landscape reported in Fig. 3.6, is consistent with current experimental data. Quadrupole deformations are highly consistent across all nine models used and agree well with experiment. In addition, proton Q_{20} and Q_{30} of ^{222,224,226,228}Ra from our SEDFs calculations are extremely consistent with available experimental data (Fig. 3.11 and 3.12), except for the unusual decrease in the measured proton Q_{30} of ^{224}Ra that cannot be explained yet.

In the neutron-deficient actinide region, in addition to the "usual suspects" of ^{224,226}Ra and ^{226,228}Th, our study suggests stable g.s. octupole deformations in ^{224,226,228}U, ^{226,228,230}Pu, and ^{228,230}Cm. The only stable pear-shaped even-even nuclei expected theoretically are

^{146,148,150}Nd and ^{150}Sm.

Our global survey predicts two exotic regions of octupole instability in extremely neutron-rich nuclei that are inaccessible experimentally. The first region, of lanthanide nuclei around ^{200}Gd, is possibly populated in a very neutron-rich r process. In the second region of actinide and transactinide nuclei with $184 < N < 206$, neutron-induced fission is likely to suppress the r-process production of nuclei with $N > 184$, but the magnitude of this hindrance strongly depends on predicted fission barriers.

Chapter 4

Intrinsic Schiff moment calculations

The results presented in Ch. 3 gave us a better understanding of different regions of octupole deformations. The strongest and most rigid octupole-deformed even-even nuclei are found in the neutron-deficient actinide and the superheavy actinide region, the latter however, are far beyond experimental reach.

In this chapter, we discuss the evaluation of the intrinsic Schiff moment,

$$\left\langle \hat{S}_z \right\rangle \equiv \frac{e}{10} \int \rho_p r_p^2 z_p d^3 r. \tag{4.1}$$

This evaluation was carried out within the HFB framework, using a modified version of the solver HFBTHO (v3.00) [70]. Blocking calculation for odd systems employs the equal filling approximation method (Sec. 2.1.4.3), hence time-odd terms are not included. Particle number is kept on average using (2.28), instead of the Lipkin-Nogami prescription (LN) used for the even-even octupole survey, because the implication of LN approximation in the context of blocking calculations is still unclear. Since the LN procedure is not used here, the ground state deformations of even-even nuclei are slightly different than from the global octupole survey, thus these nuclei were recalculated. In total, 120 deformation mesh points were used, defined as:

$$\beta_2^i \in [-0.35, 0.35], \ \beta_2^{i+1} - \beta_2^i = 0.05 \ ; \ \beta_3^i \in [0, 0.35], \ \beta_3^{i+1} - \beta_3^i = 0.05. \tag{4.2}$$

The same five Skyrme EDFs (SEDFs) as the global octupole survey were used for the Schiff moment calculations, namely UNEDF0, UNEDF1, UNEDF2, SLy4, and SV-min (see Ch. 3).

The Schiff moment expression (2.38) contains two major assumptions. The first one is the existence of a near-degenerate parity doublet, which dominates the sum (2.36) through its small energy denominator, and allows us to evaluate the intrinsic Schiff moment $\left\langle \hat{S}_z \right\rangle$ directly using the ground state proton density (2.25) from the HFB calculation. These parity doublets are more commonly identified in neutron-deficient actinide region [21]. Other studies found evidence of parity doublets in the lanthanides ^{151}Pm, ^{153}Eu, and ^{155}Eu which have energy splitting of about 100 keV between the doublet [154–156].

The second assumption requires rigid deformation in the nucleus. Although several even-even nuclei in the lanthanide region, such as ^{144}Ba and ^{146}Ba, exhibit large octupole deformations, their small $| \Delta E_{\text{oct}} |$ values (Fig. 3.16) suggest that the octupole deformations in these nuclei are soft, thus we do not consider them in the current Schiff moment analysis.

Given these reasons, our calculations for intrinsic Schiff moments are performed for octupole-deformed systems in the neutron-deficient actinide region with $86 \leq Z \leq 94$ and $N \leq 142$. Neutron-deficient isotopes with $Z = 95, 96$ that are octupole-deformed are very close to the proton drip-line, hence, they will not be presented in this chapter.
A brief description of the procedure used in calculating the odd systems is as follows:

1. Create a list of octupole-deformed even-even nuclei from the global octupole survey for each of the five SEDFs,

2. Recalculate these nuclei with no LN particle number restoration,

3. Identify the even-even ground state among the 120 outputs for each nucleus, store

the corresponding restart file for later use, select the lowest lying proton and neutron

quasiparticle (q.p.) states above the Fermi surface as the blocking candidates.

4. Perform blocking calculations using kick-off mode and identify the ground state of the

   odd system.

Several approximations have been used in the odd system's calculation: no time-odd fields were considered, approximate treatment of blocking used the equal filling approximation [82, 83], and identification of the q.p. state used Nilsson orbits of the largest s.p. component of the desired q.p. state. All create room for large uncertainties.

Since the q.p. state to be blocked is chosen from the lowest q.p. state above the Fermi surface of its even-even core, we require that the odd system's deformation is not too different from those of its even-even cores. If the deviation in the deformations between the odd and even nuclei is too large, the ordering of the q.p. orbitals in the odd system may have shifted, resulting in the blocking of a wrong q.p. state that does not correspond to the ground state of the odd system. Hence, when searching for the ground state of the odd system, the following conditions were applied:

$$\mid \beta_\lambda^{\text{g.s.}}(Z^{\text{odd}}, N^{\text{odd}}) - \beta_\lambda^{\text{g.s.}}(Z^{\text{even}}, N^{\text{even}}) \mid \leq 0.05, \ \lambda = 2, 3,$$

where

$$(Z^{\text{odd}}, N^{\text{odd}}) \in [(Z^{\text{even}}, N^{\text{even}} + 1), (Z^{\text{even}} + 1, N^{\text{even}}), (Z^{\text{even}} + 1, N^{\text{even}} + 1)].$$

In practice, since the typical range of β_2 is $[0, 0.35]$ and $[0, 0.15]$ for β_3, the above conditions are not too restrictive, and the correct ground state of the odd system is not likely to be

excluded.

4.1 Intrinsic Schiff moments in actinide nuclei

Intrinsic Schiff moments $\left\langle \hat{S}_z \right\rangle$ were evaluated in nuclei with $86 \leq Z \leq 96$ and $128 \leq N \leq 142$, using Eq. (4.1). As a result, "Schiff moments" in even-even nuclei are also calculated and presented, although strictly speaking, they are not relevant to the laboratory-system EDM (Sec. 2.2). As a demonstration, I will present results from the Ra and Ac isotopic chains in this section. More results can be found in Sec. 4.2 and Table 4.1.

4.1.1 Ra $(Z = 88)$
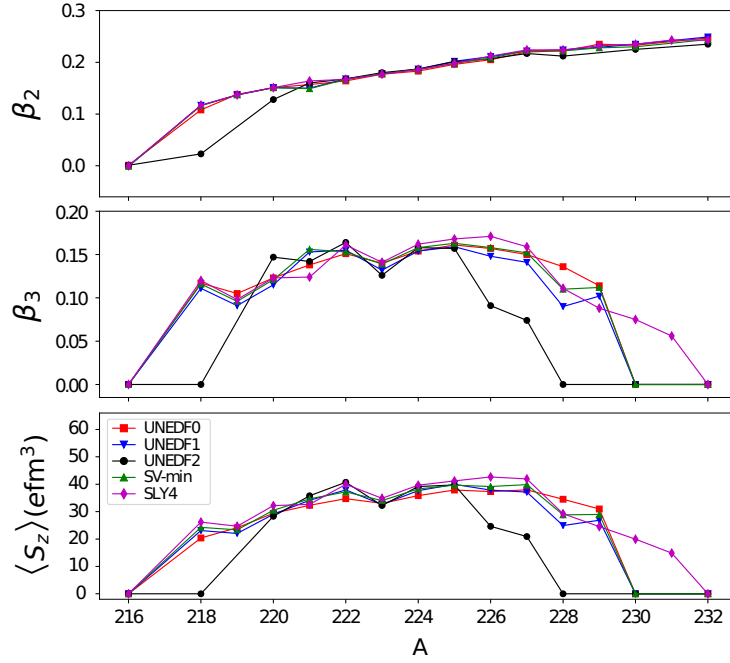
Figure 4.1: Predicted β_2, β_3, and $\left\langle \hat{S}_z \right\rangle$ values for Ra $(Z = 88)$ isotopes.

At the the center of octupole deformation of the Ra isotopes, i.e. $^{222-225}$Ra, the predicted values for β_2, β_3, and $\left\langle \hat{S}_z \right\rangle$ are very consistent between the five SEDFs. The octupole

53

deformation is believed to be rigid in the even-even Ra with $A = 220 - 224$ (Fig. 3.10), judging from the magnitude of $|\Delta E_{\text{oct}}|$. Assuming this rigid deformation also holds for their neighboring odd-mass Ra, ^{221,223,225}Ra are likely good candidates for the atomic EDM search, with average $\left\langle \hat{S}_z \right\rangle > 30$ $e\text{fm}^3$. Parity doublets in ^{223,225}Ra have been identified with energy splittings $\Delta E \approx 50$ keV, and in ^{221}Ra, the splitting is roughly doubled [21]. The octupole deformation in ^{227}Ra is perhaps not as rigid as the lighter odd-mass Ra, as the ΔE_{oct} of ^{227}Ra likely lies close to ^{226}Ra and ^{228}Ra. The energy splitting of the parity doublet in ^{227}Ra is 90 keV.

4.1.2   Ac $(Z = 89)$
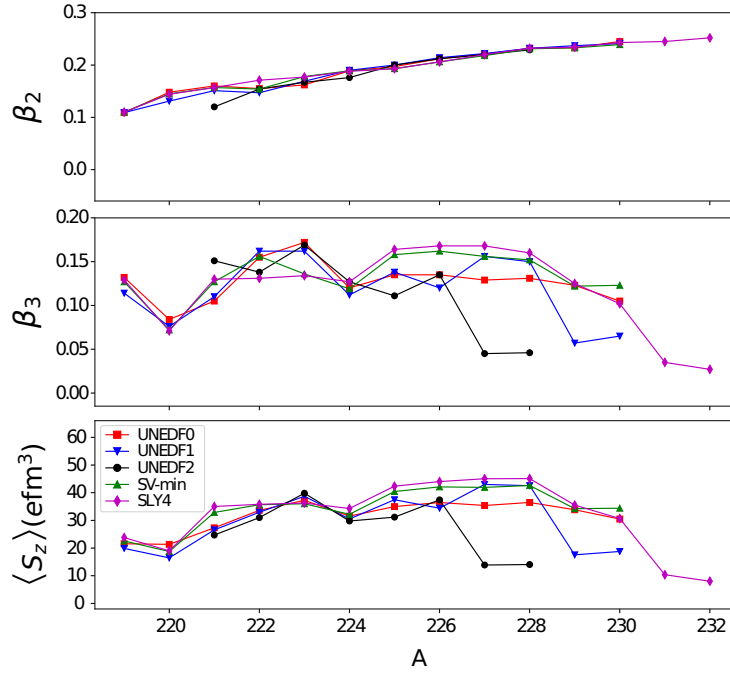
Figure 4.2:   Predicted β_2, β_3, and $\left\langle \hat{S}_z \right\rangle$ values for Ac $(Z = 89)$ isotopes.

Parity doublets were identified in ^{223,224,225,227}Ac, with $\Delta E \approx 70$ keV, 22 keV, 40 keV, and 27.4 keV, respectively [21]. Fig. 4.2 shows that the predicted β_2 values for these Ac nuclei

are consistent among the SEDFs, although the β_3 values exhibit a larger spread. Assuming the odd-N Ac isotopes also share similar tendency to develop rigid octupole deformation as their even-even cores, a wide range of $^{221-227}$Ac isotopes could be considered as excellent candidates for the atomic EDM measurements.

4.2   Summary: Intrinsic Schiff moments

In this section, I have shown the results of the intrinsic Schiff moment $\left\langle \hat{S}_z \right\rangle$ calculated using the expression (4.1), which assumes rigid deformation and the existence of parity doublets that are only found in octupole-deformed nuclei with odd-nucleon number. One needs to keep this in mind when interpreting the results of $\left\langle \hat{S}_z \right\rangle$. If these assumptions are not met, the interpretation in terms of the intrinsic Schiff moment reported here should be taken with a grain of salt.

One also needs to understand that the Schiff moment in the laboratory frame depends on the $\left\langle \hat{V}_{PT} \right\rangle$ term, and is very sensitive to the energy splitting ΔE between the parity doublet (Eq. (2.38)). Nonetheless, the intrinsic Schiff moment and octupole deformations calculated for the odd systems offer valuable insights to the relative strength of the full Schiff moment, since parity doublets and large β_3 and $\left\langle \hat{S}_z \right\rangle$ values tend to occur simultaneously.

By qualitatively extrapolating from the rigidness of octupole deformation in the odd system's even-even neighbors, and only consider the odd systems that are likely to have rigid octupole deformations, the following nuclei are likely to have large intrinsic Schiff moments. For even-Z isotopes, ^{221,223,225}Ra, ^{221,223,225,227}Th, ^{223,225,227}U, and ^{225,227}Pu; for odd-Z isotopes, ^{223}Fr, $^{221-227}$Ac, $^{221-227}$Pa, $^{223-229}$Np. Among these nuclei, parity doublets have been identified in ^{221,223,225}Ra, ^{227}Th, ^{223}Fr, ^{223,225,227}Ac [21].

If one also takes into account the lifetimes of these odd-A and odd-odd systems in order to conduct atomic EDM measurements, and limit to isotopes with $t_{1/2} > 1$ s, the potential candidates for atomic EDM measurements are listed in Table 4.1. Among isotopes with confirmed parity doublets, ^{223}Ra, ^{225}Ra and ^{227}Th share similar strength of $\left\langle \hat{S}_z \right\rangle^{\text{avg}} / \Delta E$. This "weighted" Schiff moment is much larger in ^{225}Ac and ^{227}Ac due to the small energy denominator, with ^{227}Ac almost twice the value of ^{225}Ra.

As a final comment, we note that there is a macroscopic expression [157] for the intrinsic Schiff moment:

$$S_{\text{intr}} = eZR_0^3 \frac{9}{20\pi\sqrt{35}} \beta_2\beta_3. \tag{4.3}$$

When attempting to fit all calculated $\left\langle \hat{S}_z \right\rangle$ to $ZR_0^3\beta_2\beta_3$ in the neutron-deficient actinides region, the R^2 score for a linear regression fit is only 0.43. Interestingly, when fitting $\left\langle \hat{S}_z \right\rangle$ directly to $\beta_2\beta_3$, the $R^2 \approx 0.9$ (see Fig. 4.3).

Table 4.1: Candidates for atomic EDM measurement with $86 \leq Z \leq 94$ and half-life $t_{1/2} \geq$ 1 second. $\left\langle \hat{S}_z \right\rangle$ from evaluating (4.1) has been averaged over the five Skyrme EDFs (except for ^{223}Fr and ^{229}Np which are only calculated for four Skyrme EDFs). Experimental energy splitting between parity doublets ΔE p.d. are shown where data exists [21]. The last column is the average $\left\langle \hat{S}_z \right\rangle$ divided by ΔE p.d.. The parity doublet in ^{224}Ac has not been fully established, the listed value is only for reference. ^{229}Pa is also listed, in the event that the low lying parity doublet of less than 1 keV from the ground state is confirmed.

Isotope	$t_{1/2}$	$\left\langle \hat{S}_z \right\rangle^{\text{avg}}$ ($e\text{fm}^3$)	ΔE p.d. (keV)	$\frac{\left\langle \hat{S}_z \right\rangle}{\Delta E}$ ($\frac{e\,\text{fm}^3}{\text{keV}}$)
^{223}Fr	22.00(7) min	31.30	160.45	0.195
^{221}Ra	28(2) s	33.91	103.4	0.328
^{223}Ra	11.43(5) d	33.35	50.19	0.664
^{225}Ra	14.9(2) d	39.69	55.2	0.719
^{227}Ra	42.2(5) min	35.55	90.0	0.395
^{222}Ac	5.0(5) s	33.80		
^{223}Ac	2.10(5) min	37.60	64.6	0.582
^{224}Ac	2.78(17) h	31.65	(22.0)	(1.439)
^{225}Ac	10.0(1) d	37.27	40.1	0.929
^{226}Ac	29.37(12) h	38.87		
^{227}Ac	21.772(3) y	35.84	27.4	1.308
^{225}Th	8.72(4) min	40.67		
^{227}Th	18.68(9) d	46.43	67.2	0.691
^{225}Pa	1.7(2) s	44.17		
^{226}Pa	1.8(2) min	43.51		
^{227}Pa	38.3(3) min	46.74		
^{229}Pa	1.50(5) d	50.60		
^{227}U	1.1(1) min	46.03		
^{228}Np	61.4(14) s	46.22		
^{229}Np	4.0(2) min	49.76		
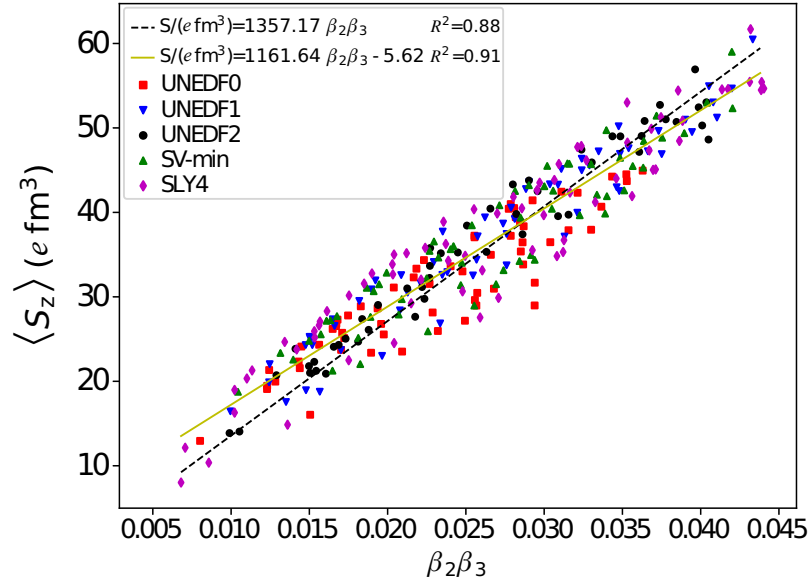
Figure 4.3: $\left\langle \hat{S}_z \right\rangle$ plotted against $\beta_2\beta_3$ for all odd systems in the neutron-deficient actinides region. Two linear fits were made, one without intercept (dashed line), and one with intercept (solid line). R^2 score for the linear fits are listed accordingly.

Chapter 5

Bayesian machine learning

This chapter summarizes a series of papers produced in our group, involving myself, from 2018 to 2020 [108,109,158,159]. These studies pertain to the applications of various Bayesian machine learning techniques to nuclear mass models. In particular, these techniques were used to improve model predictability, and to present uncertainty-quantified analysis of nuclear instability near the particle drip-lines.

5.1   The S_{2n} residual model

The binding energy, or mass of a nucleus describes how stable the nucleus is compared to its neighbors, which determines the decays of the nucleus. Theory models that predict the nuclear masses, from phenomenological models such as the liquid drop model in the early days, to the modern self-consistent mean-field models, all contain some assumptions due to incomplete physics, and approximations to reduce computational requirements; both aspects contribute to the systematic uncertainties of the predictions. On the other hand, experimental errors and fitting of the model parameters give rise to statistical uncertainties. These two types of uncertainties are responsible for most of the discrepancies between theory predictions and the measured nuclear masses.

Missing information contained in the mass differences, or the mass residuals, is generally unknown analytically. This presents us with the perfect test ground for "black-box" modeling

with machine learning. The modeled residuals can be added back to the original theory predictions to improve them. Moreover, by utilizing Bayesian machine learning techniques, one can provide uncertainty quantification for the new theory estimates.

To test this methodology, we first focus on the two-neutron separation energy S_{2n}, defined as:

$$S_{2n}(Z, N) = \text{BE}(Z, N-2) - \text{BE}(Z, N), \tag{5.1}$$

where $\text{BE}(Z, N)$ is the binding energy for nucleus with Z protons and N neutrons.

The reason for modeling the residual of S_{2n} instead of the binding energy is because, by performing a subtraction between neighboring nuclei, some of the systematic trend in the predicted masses will cancel out (Fig. 5.1). In this section, we limit ourselves to even-Z and even-N nuclei and S_{2n}.
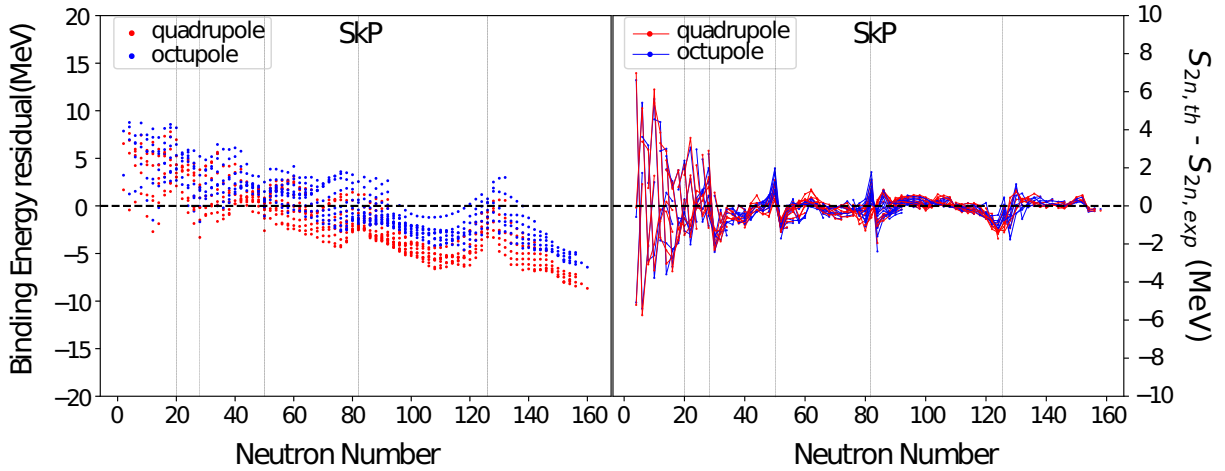
Figure 5.1: Left panel: Binding energy residuals of SEDF SkP (calculated w.r.t. experimental masses from the AME2016 mass evaluation [99, 160]). Results from octupole-deformed (blue dots) and quadrupole-deformed (red dots) survey calculations are shown. Right panel: Same as in left panel but for two-neutron separation energy S_{2n}. Note that the range on the energy axis is $[-10, 10]$ MeV for S_{2n} compared to $[-20, 20]$ MeV for BE, illustrating a significant reduction of systematic uncertainty in S_{2n}.

The S_{2n} residual is defined as the difference between experimental two-neutron separation

energy and the corresponding theory prediction:

$$\delta(Z, N) = S_{2n}^{\exp}(Z, N) - S_{2n}^{\text{th}}(Z, N, \vartheta), \tag{5.2}$$

where ϑ is represents the parameters in the theory model. Our task is to construct the emulator $\delta^{em}(Z, N)$ using machine learning techniques, such as the Bayesian neural network, Gaussian process, or frequency domain bootstrap [44–47, 49, 161–165].

Upon obtaining the posterior distribution of $\delta^{em}(Z, N)$, we can provide a new estimate of the predicted S_{2n} by combining the original theory predictions with the mean value of the emulated residuals:

$$S_{2n}^{\text{est}}(Z, N) = S_{2n}^{\text{th}}(Z, N, \vartheta) + \delta^{\text{em}}(Z, N). \tag{5.3}$$

Because the resulting $\delta^{em}(Z, N)$ is given by a probability distribution, we can assign an error bar associated with its mean value, which could be interpreted as the error bar for the new estimate $S_{2n}^{\text{est}}(Z, N)$.

In this study, 537 experimental S_{2n} values from AME2003 mass evaluation [166, 167](along with theoretical predictions) were used as the training set. 55 new data points in AME2016 mass evaluation [99, 160], i.e. S_{2n} previously unavailable in AME2003, were used as the testing data set and will be referred as AME2016-AME2003 (Fig. 5.2). This strategy aims to test data points outside the training regions, which is important for far extrapolations; this is different than the interpolations done in previous studies [45, 46, 49, 164, 165].

We have selected three groups of theory models representing different theoretical frameworks. The selection criteria for models have been defined as follows. First, the model needs
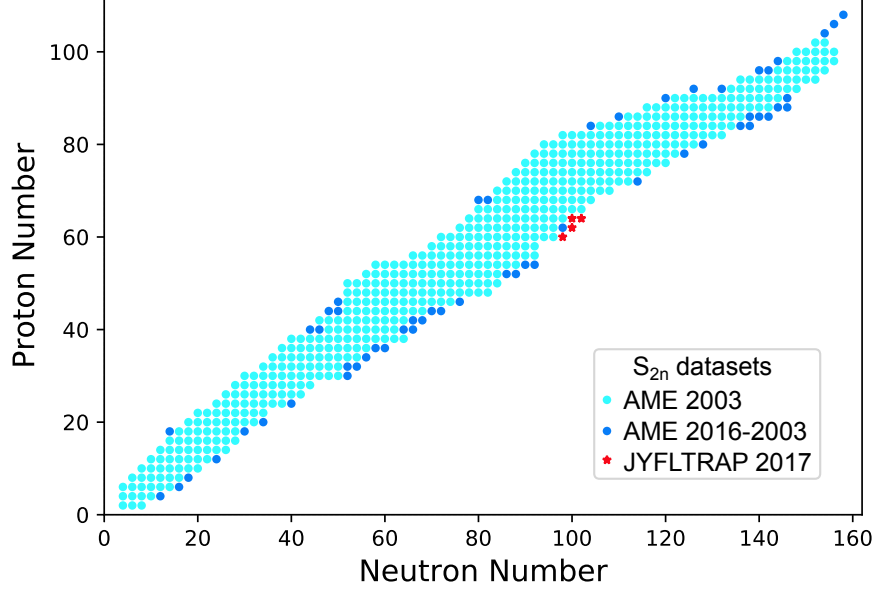
Figure 5.2: The experimental $S_{2n}(Z, N)$ datasets for even-even nuclei used in our study: AME2003 [166, 167] (light dots, 537 points), additional data that appeared in the AME2016 evaluation [99, 160] (dark dots, 55 points), and JYFLTRAP [168] (stars, 4 points). (Figure taken from Ref. [158])

to be able to extrapolate well into regions of the unknown nuclei, thus it should be based on sound many-body formalism using quantified input such as inter-nucleon interaction or nuclear energy density functional etc. Second, the theory needs to be able to reproduce other basic nuclear structural properties that impact nuclear binding energy, such as shell structure and deformations. Finally, it should be a global mass model capable of predicting binding energy in all mass regions.

The first group contains the more phenomenological global mass models FRDM-2012 [169] and HFB-24 [170], which are commonly used in astrophysical nucleosynthesis network simulations. FRDM is representative of a set of well-fitted microscopic-macroscopic mass models. HFB-24 is rooted in a self-consistent mean-field method with several phenomenological corrections added. The root-mean-square (rms) deviation of S_{2n} from both model compared to AME2003 is around 0.6 MeV (Fig. 5.3), which is as low as one can expect while using rea-
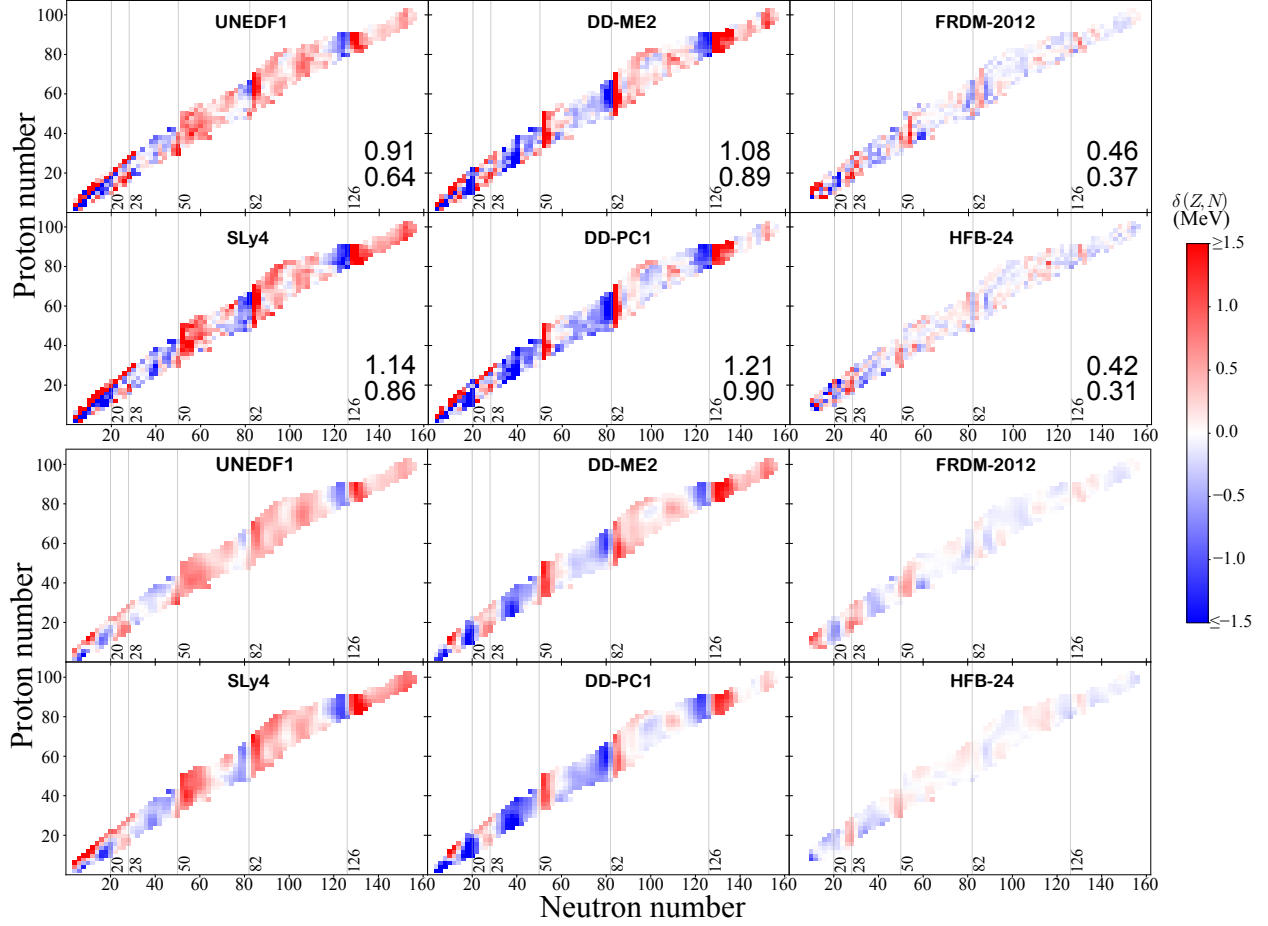
Figure 5.3: Top panel: Residuals of $S_{2n}(Z, N)$ for the six global mass models with respect to the testing dataset AME2003. The rms values of $\delta(Z, N)$ in MeV are marked for AME2003 (upper number) and AME2003-H (lower number). Bottom panel: Same as top panel but for $S_{2n}(Z, N)$ residuals smoothed with Gaussian folding function to emphasize long-range systematic trends. (Figure adapted from Ref. [158])

sonable numbers of phenomenological corrections. FRDM-2012 contains 38 parameters and was fitted to 2149 experimental nuclear masses; HFB-24 contains 25 self-consistent mean-field parameters and 5 phenomenological correction parameters and was fitted to 729 nuclear masses. Both these models included odd-odd and odd-A nuclei masses in the fitting samples.

The second group contains six microscopic Skyrme-DFT models based on energy density functionals (EDF) (Sec. 2.3) SkM* [171], SkP [172], SLy4 [96], SV-min [97], UNEDF0 [93], and UNEDF1 [94]. The rms deviation of S_{2n} of this group compared to AME2003 is around

1 MeV (Fig. 5.3). These Skyrme models contain around 12 model parameters and were fitted to less than 10 even-even nuclear masses for the first 3 models, and around 70 even-even nuclear masses for the latter 3 models.

The third group contains four microscopic covariant-DFT models based on relativistic energy density functionals NL3* [55], DD-ME2 [54], DD-PC1 [57], DD- MEδ [173]. The rms deviation of S_{2n} of this group compared to AME2003 is around 1.1 MeV, slightly higher than the Skyrme group (Fig. 5.3). The covariant EDFs have 6 to 10 parameters, with NL3* and DD-ME2 fitted to 12 even-even nuclear masses, and the other two fitted to around 60 even-even nuclear masses.

A visual representation of the residual data are shown in Fig. 5.3, with two models selected from each of the three theoretical frameworks. The bottom panel is a smoothed out version of the the residuals in the upper panel by using a Gaussian folding function to better visualize the long-range correlations. These long-range patterns are most noticeable in SLy4, DD-ME2, and DD-PC1, peaking at the neutron shell gaps and decreasing when moving further away; this is likely due to the low effective masses used in these theory models. UNEDF1 shows a much smoother trend. On the other hand, the more phenomenological models FRDM-2012 and HFB-24, being fitted to large amount of experimental masses, provide a very good reproduction of the experimental values.

5.2 Bayesian statistical models

Loosely speaking, a Bayesian method can be seen as a statistical way of solving an inverse problem of inferring the model parameters given some observations / data. Unlike the deterministic approach commonly used in the optimization process of physics modeling,

where the model parameters are determined through minimizing certain penalty function, in a Bayesian setting, a probability distribution of the parameters are generated using pure statistical sampling processes, such as in our case, the Metropolis-Hastings algorithm [174].

We perform a Bayesian analysis of the residuals $\delta(Z, N)$ using two different statistical models: Gaussian processes (GP) and Bayesian neural networks (BNN). We investigate the actual posterior distributions of all predicted quantities and parameters in the emulator model. This selection was made because GP is more capable of capturing short-range correlations while BNN is expected to capture more long-range trends. As general notation, we denote the statistical model by a function f of the particle number $x_i := (Z, N)$, and parameters θ, which are unknown and later estimated via Bayesian inference. We also replace the residual with $y_i := \delta(Z, N)$. Our Bayesian model is then of the form:

$$y_i = f(x_i, \theta) + \sigma \epsilon_i, \tag{5.4}$$

where f is either GP or BNN with parameters θ. The added term ϵ_i is a random variable used to model the error. We assume it to be an independent standard Gaussian variables with mean zero and unit variance, and σ is a noise scale parameter.

The relation Eq. (5.4) is called the likelihood equation, which relates the data y_i with the unknown parameters θ and σ. In the likelihood model, assuming fixed θ and σ, the probability density of y is denoted by $p(y \mid \theta, \sigma)$. For $x_i = (Z, N)$ where the values of y_i (S_{2n} residual) are unknown, i.e. the testing dataset, we use Eq. (5.4) to predict them once the posterior density of the unknown parameters θ and σ are determined via Bayesian inference. In order to do so, we must assume some prior distribution for these unknown model parameters, denoted as a joint probability density $\pi(\theta, \sigma)$.

According to Bayes theorem, the posterior density $p(\theta, \sigma \mid y)$, given the training data y, the prior $\pi(\theta, \sigma)$ and the likelihood models:

$$p(\theta, \sigma \mid y) \propto p(y \mid \theta, \sigma)\pi(\theta, \sigma). \tag{5.5}$$

We can then use this posterior density $p(\theta, \sigma \mid y)$ to predict y^* in the regions of x where y is unknown. This requires computing the conditional density $p(y^* \mid y, \theta, \sigma)$, where y is the known residual data, and integrating over the posterior density $p(\theta, \sigma \mid y)$ of the unknown model parameters:

$$p(y^* \mid y) = \int p(y^* \mid y, \theta, \sigma)\, p(\theta, \sigma \mid y)d\theta d\sigma. \tag{5.6}$$

As mentioned, we not only acquire the mean values of the predicted residuals, but also their uncertainties due to the probabilistic description (5.5) and (5.6) of the unknown parameters and predictions. In Bayesian terms, the quantity that resembles the "confidence interval" in classical statistics is what's called the credibility intervals. The credibility intervals, or CI, is an interval around the Bayesian mean value in which contains, e.g., 68% of the simulated sample, and is approximately the same as the confidence interval of one standard deviation if the posterior distribution of y^* is symmetric on the left and right of the mean. For simplicity, in this text, we shall treat CI as the confidence interval. This is justified because the posterior distributions of the residuals are highly symmetric.

In more precise notations, let m be the total number of samples in the posterior distribution of y_i for a given $x_i = (Z, N)$. These posterior distributions are computed via Monte Carlo techniques, in which the samples are obtained using 100,000 iterations of ergodic Markov chain produced by the Metropolis-Hastings algorithm [174].The prediction for the residual, the corrected prediction S_{2n}^{em} and the one-σ uncertainty (error bar) are thus

respectively:

$$\delta^{\text{em}}(Z,N) = \frac{1}{m} \sum_{j=1}^{m} y_j^*(Z,N),$$

$$S_{2n}^{\text{em}}(Z,N) = S_{2n}^{\text{th}}(Z,N) + \delta^{\text{em}}(Z,N), \tag{5.7}$$

$$\sigma^{\text{em}}(Z,N) = \sqrt{\frac{1}{m} \sum_{j=1}^{m} \left[y_j^*(Z,N) - \delta^{\text{em}}(Z,N) \right]^2}.$$

Here we use $S_{2n}^{\text{em}}(Z,N) \pm \sigma^{\text{em}}(Z,N)$ to approximately represent a two-sided 68%-CI and $S_{2n}^{\text{em}}(Z,N) \pm 1.96\sigma^{\text{em}}(Z,N)$ as a two-sided 95%-CI. Below I'll discuss the two specific Bayesian statistical models that were used to produce the posterior samples $y_i := \delta(Z,N)$ by constructing different $f(x_i, \theta)$ in Eq. (5.4).

5.2.1 Gaussian process

Gaussian processes have been used commonly in physics and other nature sciences to model the short-range, or local, correlations of the data. In the context of nuclear physics, it is fair to assume residual information of neighboring nuclei have stronger impact than nuclei further away due to similarities in their nuclear structures, thus GP is a suitable model for the task at hand. We treat a Gaussian process as a Gaussian functional on the two-dimensional nuclear landscape, characterized by its mean function and covariance function [175]. We take the mean function to be 0, and the "spatial" dependence of neighboring nuclei is described using an exponential quadratic covariance kernel,

$$k_{\eta,\rho}(x, x') := \eta^2 \exp\left[-\frac{(Z-Z')^2}{2\rho_Z^2} - \frac{(N-N')^2}{2\rho_N^2} \right], \tag{5.8}$$

where $x = (Z,N)$ and $\theta \equiv \{\eta, \rho_Z, \rho_N\}$ are the unknown parameters that need to be acquired through Bayesian inference. The parameter η defines the strength of dependence between neighboring nuclei, ρ_Z and ρ_N are the correlation ranges in the proton and neutron direction,

respectively. The covariance kernel k is the classical Gaussian kernel up to a linear transformation of its parameters, and it is symmetric in (x, x'). Other kernels such as Matérn kernels and exponential kernels offer similar performance on capturing short-range correlations, but the former requires more intense computation due to the embedded Bessel functions while the latter have heavy tails that are not needed here. Using the notation $\mathcal{GP}$ as a Gaussian vector here, we can define the function f in Eq. (5.4) as a random vector with parameters $\theta \equiv \{\eta, \rho_Z, \rho_N\}$ and input $x := (Z, N)$:

$$f(x, \theta) \sim \mathcal{GP}\left(0, k_{\eta,\rho}\right), \tag{5.9}$$

which means the distribution of $f(x, \theta)$ has mean 0 and covariance matrix $k_{\eta,\rho}$. The key component of the Gaussian process $f(x, \theta)$ is the covariance matrix $k_{\eta,\rho}$, which is trained on the values $k_{\eta,\rho}\left(x_i, x_j\right)$ from the known region and used to predict y^* according to its Gaussian distribution given y and θ, and can be expressed explicitly using $k_{\eta,\rho}$ [175]. We use pure experimental uncertainty to represent the noise parameter ϵ in Eq. (5.4), which is very small compared to the theory uncertainties. This value is fixed as 0.0235 MeV, which is the average experimental error.

Figure 5.4 is the computed posterior distribution of the GP parameters $\theta \equiv \{\eta, \rho_Z, \rho_N\}$ in the case of the DD-PC1 relativistic DFT model. It can be seen that all three parameters are well determined with small variance and symmetric around its mean. The strength of dependence between neighboring nuclei is of the scale $\eta = 0.87$ MeV, and the correlation range given by ρ_Z and ρ_N along the Z and N directions are precisely 68% concentrated within the width of 2ρ and 95% within the width of 4ρ. Thus we can conclude that roughly 90% of the correlation effects are localized in the region of $Z \pm 4, N \pm 2$.
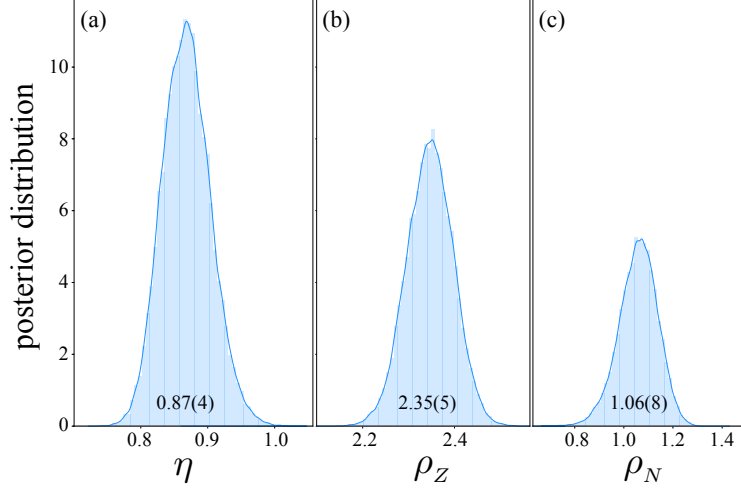
Figure 5.4: Posterior distributions of the GP parameters $\theta \equiv \{\eta, \rho_Z, \rho_N\}$ in the case of the DD-PC1 model, with the posterior mean and standard deviation listed. (Figure taken from Ref. [158])

5.2.2 Bayesian neural network

A Bayesian neural network is basically an artificial neural network [175], which computes distributions for its model parameters / weights instead of acquiring them using the frequentist approach of minimizing certain penalty functions, thus providing us with a probabilistic description of the model parameters. Here, we set the function $f(x, \theta)$ in Eq. (5.4) to have only one hidden layer and $H = 30$ hidden neurons [175]:

$$f(x, \theta) := a + \sum_{j=1}^{H} b_j \phi \left(c_j + \sum_i d_{ji} x_i \right), \tag{5.10}$$

where ϕ is a nonlinear activation function, and in our case chosen as the hyperbolic tangent function $\phi(z) = \tanh(z)$. The unknown parameters are the weights $\theta \equiv \{a, b_j, c_j, d_{ij}\}$ of this function, and are both internal to each neuron j's activation and external based on the training data to form the interacting network among neurons. The layers and number of neurons per layer H were selected to be 1 and 30 respectively, due to the small number of training data ($\sim$500) available in a nuclear physics setting.

The posterior density of y^* of the unknown region is determined by integrating over the posterior density of the unknown parameters $\theta \equiv \{a, b_j, c_j, d_{ij}\}$ as shown in Eq. (5.6). To acquire the likelihood function $p(y^* \mid y, \theta, \sigma)$, we first assume the noise term ϵ in Eq. (5.4) as a normal vector with independent and identical distributed components, with mean 0 and unit variances. We presume there is no information gain in our BNN in making more complex assumption for this term. Thus, the likelihood function is given as:

$$p(y \mid \theta, \sigma) \propto \exp\left[-\sum_i \frac{(y_i - f(x_i, \theta))^2}{2\sigma^2}\right], \tag{5.11}$$

where σ is the noise scale in Eq. (5.4). The y in the above probability density is a combination of both the training data y and the to-be-predicted values y^*. Therefore, given (θ, σ), these two datasets y and y^* can be seen as stochastically independent, and we have $p(y^* \mid y, \theta, \sigma) = p(y^* \mid \theta, \sigma)$ for Eq. (5.6).

5.2.3   Input refinement

We experimented with three variants of input for the above statistical models other than the standard $x_i = (Z, N)$. In the first variant, denoted as GP(H) and BNN(H), nuclei below Ca are removed from the dataset (H stands for "heavy"). Doing so allow us to compare our results with previous studies [45–47,49,176] that have systematically disregarded light nuclei in their datasets.

The second variant is denoted by GP(T) and BNN(T), where T represents "transformed". This variant was inspired by Ref. [49] which supplements the input $x_i = (Z, N)$ with information pertaining to the nucleus' distance from the magic numbers. This information is

represented by two additional inputs:

$$\tilde{x}_i \equiv (d_N(x_i), p(x_i)), \ p(x) = \frac{d_Z(x)d_N(x)}{d_Z(x) + d_N(x)}, \tag{5.12}$$

where $d_Z(x)$ and $d_N(x)$ are the distance of x to the closest proton and neutron magic number, respectively. The quantity $p(x)$ is the promiscuity factor that indicates the collectively in the open-shell nuclei [177].

The third variant is the combination of the above two, denoted as GP(T+H) and BNN(T+H). As we will see later, these refinements will significantly improve the BNN model, and provide only minor improvements for the GP.
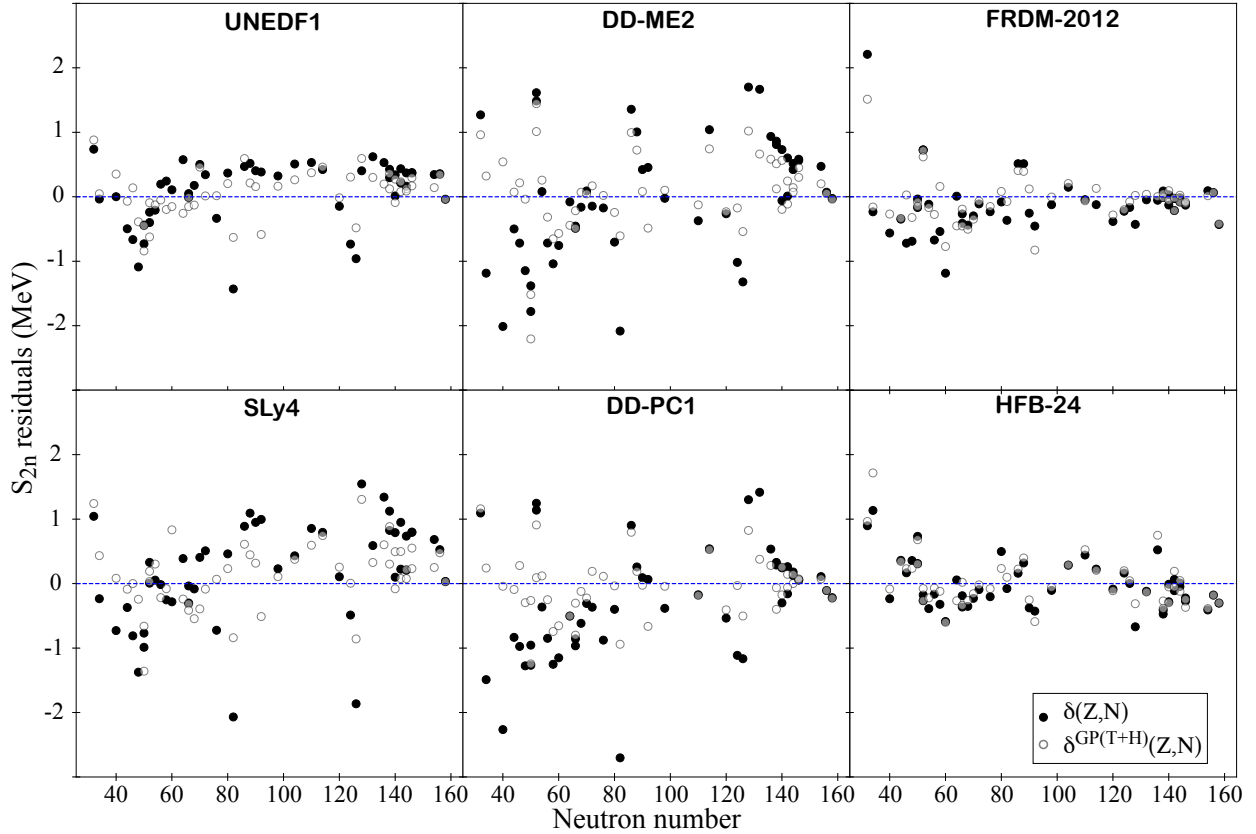
Figure 5.5: Residuals of $S_{2n}(Z,N)$ for the six global mass models with respect to the testing dataset (AME2016-AME2003): $\delta(Z,N)$ (dots) and the GP emulator $\delta^{\text{GP}}(Z,N)$ (circles). (Figure taken from Ref. [158])

5.3 Results of the S_{2n} residual model

We divided the exercise of modeling the S_{2n} residuals into three groups, each using different datasets. The first group tests the predictive power of our methodology and to compare the performance between GP and BNN, which used the training dataset AME2003 and AME2003-H (heavy) to test on AME2016-2003 data points (blue dots in Fig. 5.2). The results are shown in Fig. 5.5 and Table 5.1. Since AME2016 contains remeasured data for nuclei that were already in AME2003, if the differences in the two measurement is greater than 30% for a nucleus, we removed it from the AME2003 training dataset - this includes ^{10}He,^{24}O,^{34}Mg, and ^{52}Ca, which are moved into the testing dataset.

The second group used AME2003-H and AME2016-H as two different training datasets, and compared the trained residual models on the then recently measured masses at JYFLTRAP in 2017. Only the (T+H) variant of the inputs were used. This is to test how much the additional data points affect model predictions. The results are compared in Table 5.2.

Finally, we trained our residual emulators on the combined dataset of AME2016-H and JYFLTRAP to produce an estimate for the S_{2n} of the entire nuclear landscape, and analyzed the two-neutron drip-line of tin isotopes with the uncertainty-quantified S_{2n} values.

5.3.1 Training set: AME2003; testing set: AME2016-AME2003

The original residuals from $S_{2n}^{\text{th}}(Z, N)$ (black dots) and the residuals from the new estimates $S_{2n}^{\text{est}}(Z, N)$ (white circles) in Eq. (5.3) of six representative nuclear mass models are shown in Fig. 5.5 for GP(T+H). In Fig. 5.5, nearly all white circles, which are the residuals from the new estimates, moved closer to 0 compared to the corresponding black dots, which are from the original theory predictions. This is to say that the GP model systematically improved the

predicted S_{2n} for these nuclear mass models. Additionally, the local trends of the residuals have been visibly dampened, and the corrected residuals are closer to having a distribution of mean zero.

Table 5.1 lists the rms deviations of the residuals from different nuclear mass models using the standard input and three different input variants discussed in Sec. 5.2.3, and the two Bayesian models GP and BNN for the emulators $\delta^{\text{em}}(Z, N)$. Both GP and BNN reduced the rms deviation of the residuals noticeably for the Skyrme and relativistic DFT models, with GP having consistently better performance. The performance on relativistic DFT models are the best, around 50% rms reduction, followed by the Skyrme DFT models, around 30% rms reduction. In the more phenomenological models FRDM-2012 and HFB-24, the results are mixed. In HFB-24, instead of decreasing, the rms has increased for most cases, and for FRDM-2012, only the GP models systematically improved its prediction. This is not surprising, as we expect the residuals from the more microscopic models to have more implicit structure, whereas the more phenomenological models have been fitted very closely to mass data, and their residuals have a higher proportion of statistical noise. This can also be seen from the fact that after the improvements, the rms deviations seem to have reached a lower bound at around 300-500 keV for the GP(T+H) variant, which has the best performance, and is likely from the irreducible statistical noise. This lower bound also suggests that our statistical models captured most of the residual structure, and that an uncertainty quantification (UQ) analysis becomes necessary to further assess the models' quality.

Table 5.1: Root mean square values of $\delta(Z,N)$, $\delta^{\mathrm{BNN}}(Z,N)$, and $\delta^{\mathrm{GP}}(Z,N)$ (in MeV) for various nuclear models with respect to the testing dataset consisting of the AME2016-AME2003 S_{2n} values. The training AME2003 and AME2003-H datasets were used to compute the emulators $\delta^{\mathrm{BNN}}(Z,N)$ and $\delta^{\mathrm{GP}}(Z,N)$. The two numbers listed under the model's name in the first column are the uncorrected δ_{rms} model values with respect to AME2003 and AME2003-H datasets, respectively. The rms residuals corrected by a statistical model are shown in the remaining columns. For each model, GP results $\delta_{\mathrm{rms}}^{\mathrm{GP}}$ are given in the upper row and the BNN results $\delta_{\mathrm{rms}}^{\mathrm{BNN}}$ are listed in the lower row. The numbers in parathenses indicate the improvement in percent. The four statistical variants are listed: Std is the standard standard input $x = (Z,N)$; T indicates results involving the non-linear transformation $\tilde{x}_i = (d_N(x_i), p(x_i))$; H is based on the reduced dataset AME2003-H pertaining to heavy nuclei with $Z \geq 20$. (Table taken from Ref. [158])

model	Std	T	H	T+H
SkM*	0.96(23)	0.96(23)	0.49(52)	0.49(52)
1.25/1.01	0.99(20)	0.81(35)	0.73(28)	0.53(47)
SLy4	0.82(13)	0.82(13)	0.52(35)	0.52(35)
0.95/0.80	0.91(3)	0.82(14)	0.71(11)	0.56(30)
SkP	0.75(11)	0.75(11)	0.38(39)	0.38(39)
0.84/0.62	0.76(9)	0.74(12)	0.59(5)	0.45(27)
SV-min	0.70(10)	0.70(10)	0.32(34)	0.33(34)
0.78/0.49	0.72(8)	1.35(-73)	0.50(-1)	0.43(12)
UNEDF0	0.73(6)	0.73(6)	0.34(37)	0.34(37)
0.78/0.54	0.87(-12)	0.73(7)	0.55(0)	0.46(16)
UNEDF1	0.61(8)	0.61(8)	0.34(30)	0.34(30)
0.66/0.49	0.79(-20)	0.74(-12)	0.53(-10)	0.32(33)
NL3*	0.84(29)	0.84(29)	0.46(47)	0.45(47)
1.19/0.86	1.10(7)	0.90(24)	0.83(4)	0.69(20)
DD-MEδ	0.73(35)	0.74(35)	0.55(42)	0.55(42)
1.13/0.96	1.08(4)	0.91(19)	0.89(7)	0.75(22)
DD-ME2	0.71(32)	0.71(31)	0.63(34)	0.62(34)
1.04/0.95	1.00(4)	1.32(-27)	0.90(5)	0.61(36)
DD-PC1	0.79(28)	0.79(28)	0.46(50)	0.46(50)
1.10/0.91	1.00(9)	1.33(-22)	0.85(7)	0.54(41)
FRDM-2012	0.57(9)	0.57(9)	0.36(25)	0.36(26)
0.63/0.49	0.61(4)	0.72(-15)	0.48(2)	0.45(7)
HFB-24	0.40(-1)	0.40(-1)	0.40(-8)	0.40(-8)
0.40/0.37	0.59(-48)	0.44(-10)	0.37(1)	0.35(6)

5.3.2 Training sets: AME2003-H, AME2016-H, testing set: JYFLTRAP-2017

The difference in performance of the models trained on AME2003-H and the larger dataset AME2016-H is compared by predicting the recent S_{2n} values from JYFLTRAP using the (T+H) variant of the model input. The testing dataset consists of 4 points (red stars in Fig. 5.2); the results are shown in Table 5.2. From this table, we can see that the GP models reduced the rms significantly for all cases, while the BNN predictions of SLy4, SkP, SV-min, UNEDF0, and DD-MEδ deteriorated. This can be attributed to the emphasis on long-range correlations from the BNN model due to the non-vanishing tail in the activation function. On the other hand, the GP models, which use a Gaussian-like kernel and a range of correlation effects of $Z \pm 4, N \pm 2$, focus more on the short-range correlations and performed better. This can be explained by the observation that the residual surface in the region of JYFLTRAP data ($Z \sim 62, N \sim 100$) is fairly smooth (Fig. 5.3).

Overall, slightly better improvements have been achieved for the models trained using the AME2016-H dataset. However, this improvement is not significant - we see that only one new measurement in the extended data, i.e. AME2016-2003 (Fig. 5.2 blue dots), is in the vicinity of the testing dataset, and thus can only impose weak constraints on regions of the testing data.

5.3.3 Two-neutron drip-line of Sn ($Z = 50$)

In the next step, we trained the residual emulators on the entire even-even nuclear landscape with the combined dataset of AME2016-H and JYFLTRAP, using the (T+H) input variant. Based on results from this set of predictions, Fig. 5.6 shows the extrapolated S_{2n} values

Table 5.2: Similar as in Table 5.1 except for the rms values of $\delta(Z, N)$, $\delta^{\mathrm{BNN}}(Z, N)$, and $\delta^{\mathrm{GP}}(Z, N)$ (in MeV) for various nuclear models with respect to the testing dataset consisting of the four JYFLTRAP S_{2n} values. The second column shows the uncorrected rms value δ_{rms}. For each model, the training datasets AME2003-H (third column) and AME2016-H (fourth column) were used to compute $\delta_{\mathrm{rms}}^{\mathrm{GP}}$ (upper row) and $\delta_{\mathrm{rms}}^{\mathrm{BNN}}$ (lower row) using the T+H variant of statistical calculations. (Table taken from Ref. [158])

model	δ_{rms}	2003-H	2016-H
SkM*	0.91	0.40(56)	0.31(66)
		0.24(74)	0.25(72)
SLy4	0.27	0.09(65)	0.09(67)
		0.42(-57)	0.28(-4)
SkP	0.19	0.16(14)	0.14(26)
		0.35(-85)	0.36(-92)
SV-min	0.14	0.11(18)	0.10(29)
		0.17(-20)	0.26(-86)
UNEDF0	0.11	0.11(-3)	0.11(1)
		0.33(-199)	0.22(-97)
UNEDF1	0.26	0.17(36)	0.14(48)
		0.09(64)	0.13(50)
NL3*	0.32	0.19(39)	0.22(32)
		0.17(47)	0.18(43)
DD-MEδ	0.16	0.08(50)	0.09(46)
		0.18(-14)	0.28(-4)
DD-ME2	0.30	0.12(58)	0.13(55)
		0.28(8)	0.29(2)
DD-PC1	0.28	0.17(41)	0.13(52)
		0.25(12)	0.27(5)
FRDM-2012	0.13	0.10(20)	0.09(26)
		0.05(60)	0.05(58)
HFB-24	0.13	0.12(2)	0.11(12)
		0.07(43)	0.10(25)

and its credibility intervals (CI) of the Sn ($Z = 50$) isotopes using GP and BNN, for the relativistic DFT model DD-PC1. The objective here is to predict the location of the two-neutron drip-line. This is roughly equivalent to finding the largest neutron number N^* such that the lower endpoint of its one-sided 1.65-sigma CI barely touches the $S_{2n} = 0$ line, i.e.
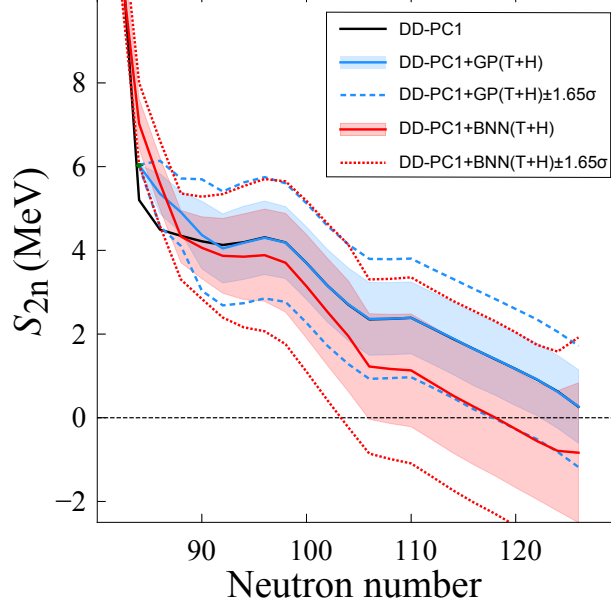
Figure 5.6: Extrapolations of S_{2n} for the even-even Sn chain calculated with DD-PC1 using statistical GP$(T + H)$ and BNN$(T + H)$ approaches. One-sigma and 1.65-sigma CIs are marked. (Figure taken from Ref. [158])

a 95% probability that this N^* gives the correct two-neutron drip-line. In Fig. 5.6, we can see that both the original DD-PC1 prediction and the DD-PC1+GP(T+H) posterior mean predicted N^* to be 126, and $N^* = 122$ and 118 at the 1- and 1.65-sigma CI, respectively. Similarly, the DD-PC1+BNN(T+H) posterior mean predicted N^*=118, and N^*=102 and 104 at the 1- and 1.65-sigma CI, respectively. One can immediately see the advantage of this description of the drip-line over simply saying: "DD-PC1 predicts the two-neutron drip-line of Sn at $N = 126$".

5.4 Neutron drip-line in the Ca region using Bayesian model averaging

The statistical model of residuals served as a proof of concept, which allowed us to test and analyze the performance of various Bayesian models and other aspects of the methodology.

In conclusion, we found that using the GP as our likelihood model has the overall best performance, and is also more numerically stable (Ref. [158]). The performance further increases by expanding the input dimension for the statistical models to include information on a nucleus' proximity to the neutron magic gaps. One could also limit their domain of training to heavy nuclei, such as nuclei above Ca to improve model performance, if they are only interested in heavier regions of the nuclear landscape. An additional benefit of using the Bayesian methodology is the resulting probabilistic description of the model parameters. This provides us a quantitative way to estimate our predictions' uncertainties, and thus quantifies the level of confidence of our predictions.

We next devoted ourselves to a more specific analysis on the neutron drip-line near the Ca region using the techniques developed in Sec. 5.1 and 5.2, and only used the GP model which was proven to be more effective. We also included the residual model for the one-neutron separation energy:

$$S_{1n}(N, Z) = BE(N, Z) - BE(N - 1, Z), \tag{5.13}$$

which is the difference in binding energies between neighboring nuclei with the difference of only one neutron. The neutron number here is always an odd number, which is to say we only study the residuals of S_{1n} in a system with odd-N and S_{2n} for systems with even-N. This is due to the fact that an odd-N system will decay first via removing one neutron, and an even-N system will decay first via removing a pair of neutrons, a consequence of the pairing correlation.

Since most calculations in DFT are performed for the even-even systems due to the additional blocking procedure required when dealing with the odd nucleon (Sec. 2.1.4.3), we took a simple approach in which we used the binding energies of the even-even neighbor and

the average paring gaps to approximate the binding energy of an odd-A (or odd-odd) system via:

$$\text{BE}(Z-1, N) = \tfrac{1}{2}[\text{BE}(Z, N) + \text{BE}(Z-2, N)]$$
$$+\tfrac{1}{2}\left[\Delta_p(Z, N) + \Delta_p(Z-2, N)\right], \tag{5.14}$$

$$\text{BE}(Z, N-1) = \tfrac{1}{2}[\text{BE}(Z, N) + \text{BE}(Z, N-2)]$$
$$+\tfrac{1}{2}\left[\Delta_n(Z, N) + \Delta_n(Z, N-2)\right], \tag{5.15}$$

where Δ_n and Δ_p are the average neutron and proton pairing gaps from DFT calculations [65]. The S_{1n} residuals $\delta_{1n}(Z, N)$ are defined similarly to $\delta_{2n}(Z, N)$ in Eq. (5.2), with a change in all the subscripts from $2n$ to $1n$.

Two training datasets were used in this work, in order to test the impact of additional nuclear mass measurements on the performance of our residual models, similar to what was done in Sec. 5.3. The first set uses the AME2003 experimental data, and the second set is AME2016*, which is AME2016 supplemented with the then new measurement of $^{52-55}$Ti masses from experiments at TRIUMF [178]. Nine theory models were used in this exercise, including seven Skyrme DFT models SkM* [171], SkP [172], SLy4 [96], SV-min [97], UNEDF0 [93], UNEDF1 [94], and UNEDF2 [95] and two more phenomenological models FRDM-2012 [169] and HFB-24 [170].

Figure 5.7 shows the new estimates for $S_{1n/2n}$ from the nine theory models:

$$S^{\text{est}}_{1n/2n}(Z, N) = S^{\text{th}}_{1n/2n}(Z, N,) + \delta^{\text{em}}_{1n/2n}(Z, N). \tag{5.16}$$

Experimental separation energies of $^{55-57}$Ca are provided by AME2016 extrapolations. We can see that all Skyrme DFT models' predictions for the S_{1n} values of ^{55,57}Ca are
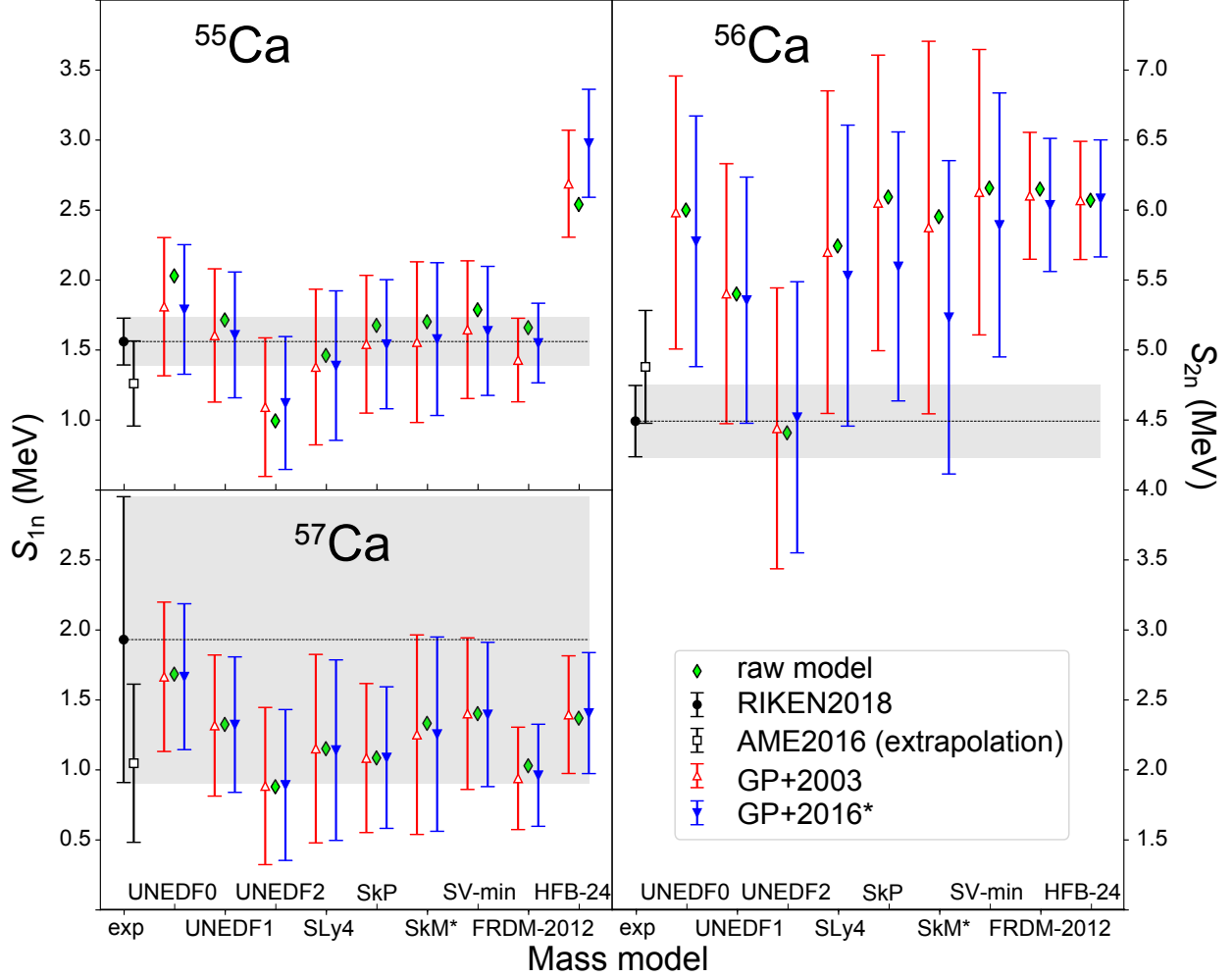
Figure 5.7: One-neutron separation energy for ^{55,57}Ca (left) and two-neutron separation energy for ^{56}Ca (right) calculated with the nine global mass models with statistical correction obtained with GP trained on the AME2003 (GP + 2003) and AME2016* datasets. The recent data from Ref. [179] (RIKEN2018) and the extrapolated AME2016 values [99, 160] are marked. The shaded regions are one-sigma error bars from Ref. [179]; error bars on theoretical results are one-sigma credible intervals computed with GP extrapolation. (Figure taken from Ref. [159])

consistent with experiments within the range of uncertainties, and the S_{2n} values of ^{56}Ca

are consistent with the experimental data for new predictions of UNEDF1, UNEDF2, SLy4,

SkP and SkM*. The GP corrections for the more phenomenological models are very small,

due to the fact that these models are already well-fitted in almost all mass regions, thus

leaving very little information to be used for the statistical process. The large deviation

in the new HFB-24 predictions is due to the irregular behavior of its neutron separation energies in its original prediction.

Since we're using GP model, as discussed in Sec. 5.2.1, the effective range of the GP is very short, meaning that additional data points in the AME2016* training set compared to AME2003 do not have a huge impact on our GP model. There are slight improvements in the mean value predictions of the separation energies.

We also introduce a quantity $p_{ex}(Z, N)$, which is called the probability of existence. $p_{ex}(Z, N)$ is the probability of the predicted separation energy $S^*_{1n/2n}(Z, N)$ to be positive in its posterior distribution:

$$p_{ex}(Z, N) := p\left(S^*_{1n/2n}(Z, N) > 0 \mid S_{1n/2n}\right). \tag{5.17}$$

This provides another way of describing a nucleus' instability to neutron decay.

The $S_{1n/2n}$ predictions near the Ca drip-line are shown in Fig. 5.8 for the theory models UNEDF0, SV-min and FRDM-2012. The probability $p_{ex}(Z, N)$ is shown in the figure's insert. The colored bands are the one-sigma CIs. We can see that the posterior predictions between the three theory models are overall consistent.

Without the loss of generality, we chose $p_{ex} = 0.5$ as the boundary for the estimated one and two neutron drip-lines. This is marked by a dotted line in this figure.

Applying the same strategy for the broader region around the neutron-rich Ca isotopes we arrive at Fig. 5.9. The top panel, Fig. 5.9(a) uses uniform averaging (equal weights) across the nine theory models after correction with Eq. (5.16). Under this simplistic averaging scheme, the p_{ex} values for the already discovered nuclei [180, 181] ^{49}S, ^{52}Cl, and ^{53}Ar are 0.58, 0.45, and 0.64, respectively. These low p_{ex} values show that the odd-neutron systems present a
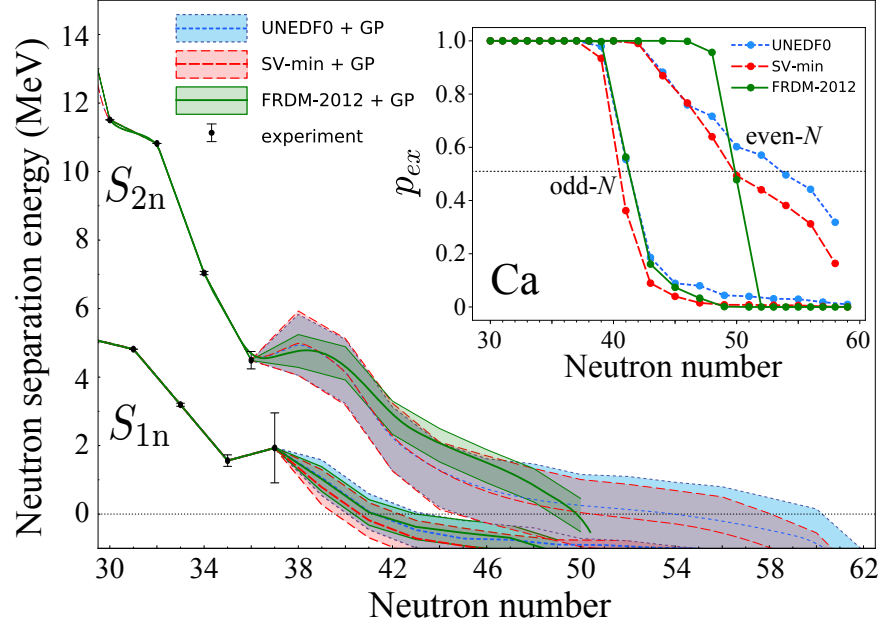
Figure 5.8: Extrapolations of S_{1n} and S_{2n} for the Ca chain corrected with GP and one-sigma CIs, combined for three representative models. The solid lines show the average prediction while the shaded bands give one-sigma CIs. The insert shows the posterior probability of existence for the Ca chain. The $p_{\text{ex}} = 0.5$ limit is marked by a dotted line. (Figure taken from Ref. [159])

challenge for our theory models, as was noticed in Ref. [180]. Thus, we use the knowledge that these three isotope have been observed to inform the model averaging process, through the posterior averaging weights:

$$w_k := p\left(\mathcal{M}_k \,|\, {}^{52}\text{Cl}, {}^{53}\text{Ar}, {}^{49}\text{S} \text{ exist}\right). \tag{5.18}$$

These weights reflect the ability of a model $\mathcal{M}_k$ to predict the existence of these isotope, i.e. the probability of predicting $S_{1n} > 0$ after correction. Using the posterior weights, the resulting p_{ex} values for ${}^{49}\text{S}$, ${}^{52}\text{Cl}$, and ${}^{53}\text{Ar}$ are 0.69, 0.53, and 0.69, respectively(Fig. 5.9(b)), slightly better than using uniform model averaging.

By comparing Fig. 5.9(a) and (b), the impact of including the information that ${}^{49}\text{S}$, ${}^{52}\text{Cl}$, and ${}^{53}\text{Ar}$ exist were able to extend the drip-line ($p_{\text{ex}}(Z, N) \geq 0.5$) by two neutron numbers
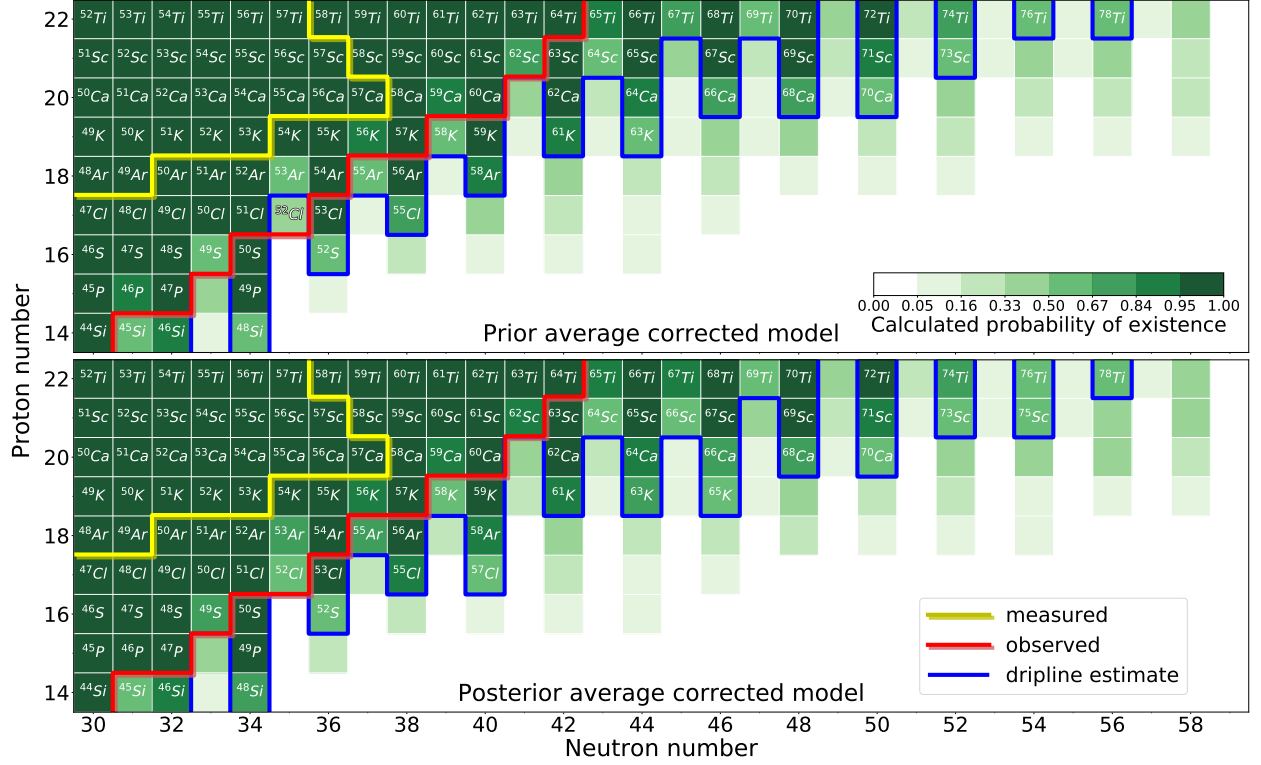
Figure 5.9: Posterior probability of existence of neutron-rich nuclei in the Ca region averaged over all GP corrected models. Top: Uniform model averaging. Bottom: Averaging using posterior weights Eq. (5.18) constrained by the existence of ^{52}Cl, ^{53}Ar, and ^{49}S. The range of nuclei with experimentally known masses is marked by a yellow line. The red line marks the limit of nuclear domain that has been experimentally observed; nuclei to the right of the red line await discovery. The estimated drip line that separates the $p_{\text{ex}} > 0.5$ and $p_{\text{ex}} < 0.5$ regions is indicated by a blue line. (Figure taken from Ref. [159])

in most cases. According to these average $p_{\text{ex}}(Z, N)$, we can say that ^{61}Ca and ^{71}Ti are expected to be one-neutron unstable while the two-neutron drip-lines are at ^{70}Ca and ^{78}Ti. The nucleus ^{59}K, which had one registered event in Ref. [180], is predicted to be stable against neutron decay.

5.5 Proton drip-line analysis and two-proton emitters

In the next project we improved predictions by using Bayesian model averaging (BMA) to the proton-rich side of the nuclear landscape, with an additional goal of identifying two-proton

emitters.

Because of the Coulomb barrier, the one- and two-proton drip-lines lie relatively close to the valley of stability. Thus the half-lives of proton-unstable nuclei beyond the drip-lines are relatively long, allowing us to study the nuclear structure and dynamics in systems with low-lying proton continuum. One of the phenomenon that emerges in these region is the existence of two-proton emitters. Unlike the one- and two-neutron drip-lines shown in Fig. 5.8, which has the clear trend that the S_{1n} lies to the left of the S_{2n} line, and thus one-neutron drip-line will always occur before two-neutron drip-line (also seen in Fig. 5.9), there is the possibility that in a proton-rich nucleus, the two-proton separation energy S_{2p} is negative while S_{1p} is positive. This implies that the system can be one-proton bound but at the same time unstable to two-proton emission. Several two-proton emitters have been identified by experiments: ^{19}Mg [182], ^{45}Fe [183, 184], ^{48}Ni [185–188], ^{54}Zn [189, 190], and ^{67}Kr [191]. Additionally, broad resonances associated with the two-proton emission were reported in several light nuclei such as ^{6}Be [192] and ^{11,12}O [193, 194].

In this work, we included two Gogny DFT models D1M [53] and BCPM [195] to the set of models used in Sec. 5.4, making the total number of theory models used to be eleven. The D1M model is a modern parametrization of the finite-range Gogny interaction, and fitted to 2149 masses from the AME2003 dataset and other nuclear properties. The BCPM model is primarily given by a fit to the equation of state in both neutron and symmetric nuclear matter, which resulted in relatively small numbers of free parameters, and was fitted to the masses of 579 even-even nuclei from the AME2003 mass dataset [166].

5.5.1 Modified Gaussian process and Bayesian model averaging

We modified the GP model slightly as compared to what was done in Sec. 5.2.1, and introduced an additional parameter μ as the mean of the Gaussian vector:

$$f(x, \theta) \sim \mathcal{GP}\left(\mu, k_{\eta,\rho}\left(x, x'\right)\right).\tag{5.19}$$

This added parameter μ improved the rms deviation of the residual by an additional 15% compared to the initial 25% improvement from the zero-mean version of the GP.

The training dataset used is AME2016+, where we augmented the AME2016 dataset with masses from Ref. [168, 178, 196–200], and kept the most recent value if there were repeat measurements.

Four variants of weights for the model averaging were used in this work. The first used uniform weights (BMA-0) without the need of additional information and the costly computation of the posteriors. The other three variants, BMA-I, -II, and -III are built on Bayesian model averaging and their weights depends on how information from the known two-proton emitters $x_{2p,\text{ known}} \equiv \left\{{}^{19}\text{Mg}, {}^{45}\text{Fe}, {}^{48}\text{Ni}, {}^{54}\text{Zn}, {}^{67}\text{Kr}\right\}$ is utilized.

The second variant, BMA-I, used the conditional probability that the corrected theory model is able to predict the correct signs of the experimental Q_{2p} and S_{1p} values for $x_{2p,\text{ known}}$. The weights are given as:

$$w_k(\text{I}) \propto p\left(\mathcal{M}_k \mid Q_{2p} > 0, S_{1p} > 0 \text{ for } x_{2p,\text{ known}}\right),\tag{5.20}$$

where $\mathcal{M}_k$ represents the theory model.

The third variant BMA-II was based directly on the ability of a theory model $\mathcal{M}_k$ to

predict the Q_{2p} values of the five known two-proton emitters $x_{2p,\ \text{known}}$:

$$w_k(\text{II}) \propto p\left(\mathcal{M}_k \mid Q_{2p} \text{ of } x_{2p,\ \text{known}}\right). \tag{5.21}$$

The final variant BMA-III is a trivial version of BMA-II, consisting of the Gaussian likelihood of $x_{2p,\ \text{known}}$ evaluated at the posterior mean and posterior variance, assuming that these values are statistically independent. Compared to BMA-II, this variant ignores all correlation effects of the posterior predictions for $x_{2p,\ \text{known}}$. The weights for BMA-III are given as:

$$w_k(\text{III}) \propto \prod_{i \in x_{2p,\ \text{known}}} \frac{1}{\sqrt{2\pi\sigma_i^2}} e^{-\frac{1}{2}\left(\frac{y_i}{\sigma_i}\right)^2}, \tag{5.22}$$

where y_i are the Q_{2p} residuals of $x_{2p,\ \text{known}}$.

As a result, we discovered that the BMA-0, BMA-I, and BMA-III variants achieved better performance compared to the more sophisticated BMA-II, and the best performance in terms of rms deviation reduction came from the simplest BMA-0 and BMA-I variants. The resulting prediction of p_{ex} for proton-rich nuclei with $16 \leq Z \leq 82$ is shown in Fig. 5.10.

5.5.2 Two-proton emitters

Although the proton chemical potential is positive for nuclei with $S_{1p/2p} < 0$, the HFB (Sec. 2.1.3) calculations are very stable in the range of binding energies considered due to the Coulomb barrier's confinement effect on the proton density that effectively pushes the proton continuum up in energy in the proton-rich nuclei. Thus, we can safely obtain the proton separation energies $S_{1p/2p}$ and the corresponding Q values from the binding energies of the proton unbound systems.
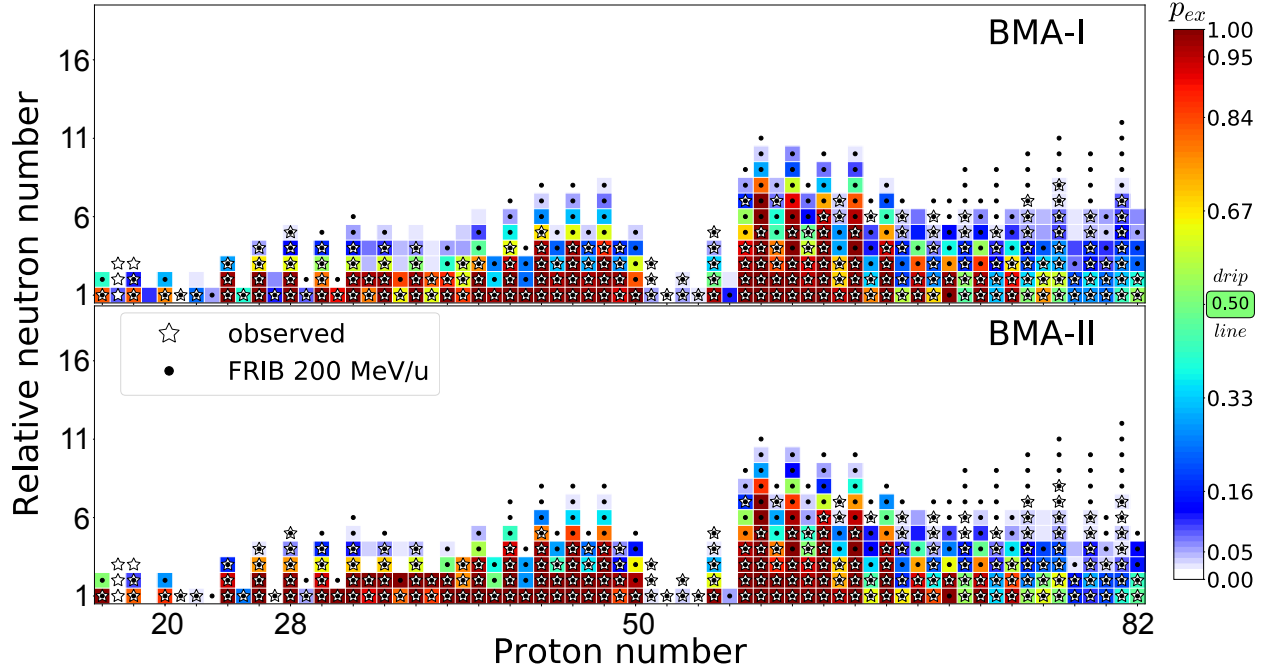
Figure 5.10: Probability of existence p_{ex} that a nuclei is bound with respect to proton decay for proton-rich nuclei with $16 \leq Z \leq 82$. Calculations using BMA-I (top) and BMA-II (bottom) variants of model averaging are shown. For each proton number, p_{ex} is shown along the isotopic chain versus the relative neutron number $N_0(Z) - N$, where $N_0(Z)$, listed in Tables A.3 and A.4, is the neutron number of the lightest proton-bound isotope for which an experimental one- or two-proton separation energy value is available. The domain of nuclei that have been experimentally observed (both proton-bound and proton-unbound) is marked by open stars; those within FRIB's experimental reach are marked by dots. (Figure taken from Ref. [109])

This work is considered as an extension of the previous global survey of proton emitters [201, 202], and uses the same criterion to select *true* two-proton emitters:

$$Q_{2p} > 0, \quad S_{1p} > 0, \tag{5.23}$$

where $Q_{2p} = -S_{2p}$. This condition corresponds to a simultaneous emission of two-proton in the diproton model [185, 186], compared to the sequential emission of two protons in the direct-decay model [163]. We shall refer to the two-proton emission corresponding to the diproton model as the *true* two-proton emission.

There is an additional constraint on the nucleus' lifetime when selecting a two-proton emitter, due to the fact that very large Q values will cause the decay to be too fast to be observed. On the other hand, if the Q values are too small, the proton-decay rates will be negligible compared to other decay channels such as β or α decays. The practical range of lifetime to consider is [201]:

$$10^{-7} < T_{2p} < 10^{-1}s. \tag{5.24}$$

The lower bound of 100 ns is to ensure the two-proton decay can be captured by current experimental techniques, and the upper bound of 100 ms is to prevent the nucleus from being dominated by β decay. We used the semi-classical Wentzel-Kramers-Brillouin (WKB) approximation and assumed a diproton decay with angular momentum $l = 0$ to get an order-of-magnitude estimate for the two-proton emitters' lifetimes. A Woods-Saxon potential with the Chepounov parameters was used. Details of the calculation can be found in Refs. [201, 203]. The proton overlap $\mathcal{O}^2 = 0.0011$ has been fitted to match the measured lifetimes of ^{19}Mg, ^{45}Fe, ^{48}Ni, and ^{54}Zn. Branching ratio of the two-proton decay channel in ^{67}Kr cannot be determined, and was thus left out of the fit.

We also defined the posterior probability p_{2p} for *true* two-proton emitters that satisfies Eq. (5.23) as:

$$p_{2p} := p\left(S_{2p}^* < 0 \cap S_{1p}^* > 0 \mid S_{1p/2p}\right), \tag{5.25}$$

where $S_{1p/2p}^*$ are the values from the unknown mass region, and $S_{1p/2p}$ are what's being used as the training dataset, following conventions in Sec. 5.2.

Fig. 5.11 shows the Q_{2p} values from the BMA-I predictions together with the range of
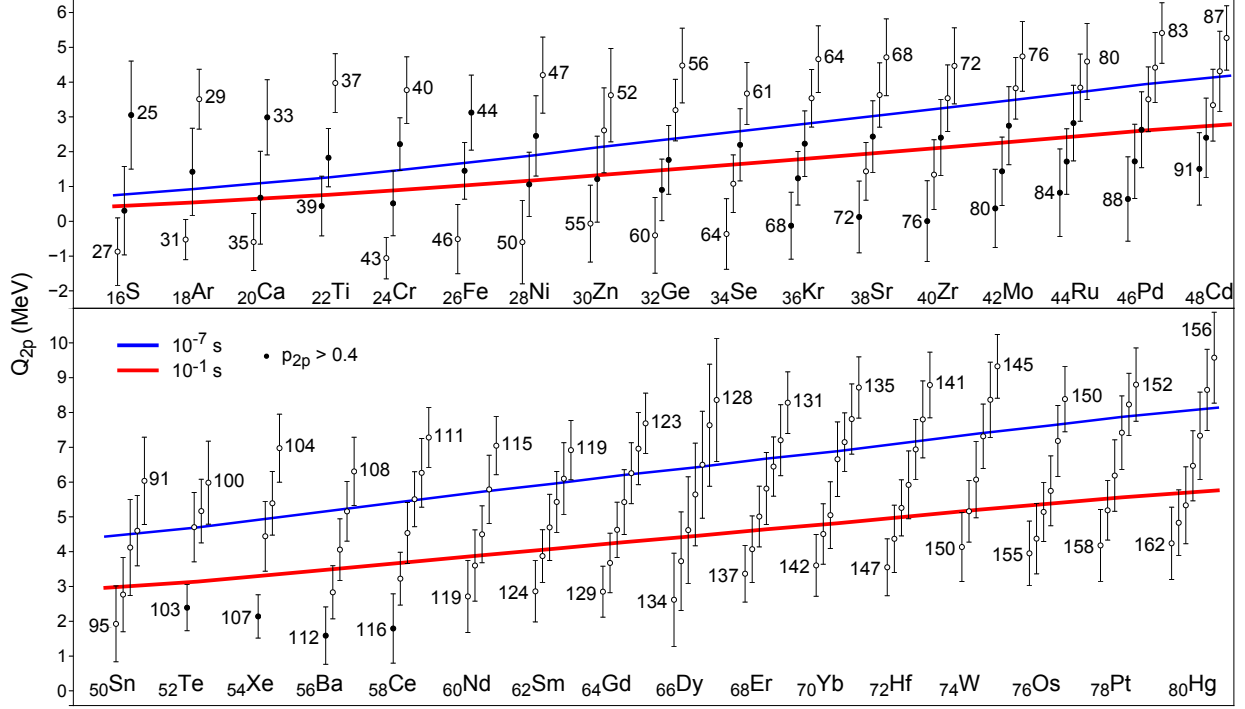
Figure 5.11: Q_{2p} values predicted in BMA-I for even-even isotopes with $16 \leqslant Z \leqslant 80$. The thick solid lines mark the lifetime range (5.24). The mass numbers of selected isotopes are shown. The nuclei with the probability $p_{2p} > 0.4$ are indicated by dots. Here, we used this value of p_{2p} rather than $p_{2p} > 0.5$ because the criterion (5.25) of the *true* 2p emission is slightly more restrictive than the energy criterion previously adopted in Ref. [202]. (Figure taken from Ref. [109])

lifetime in (5.24). The colored shades for the lifetime range corresponds to the uncertainty in the fitted proton overlap $\mathcal{O}^2$, and is clearly negligible in most cases except for e.g. ^{41}Cr. It is important to note that the large error bars in the Q_{2p} predictions correspond to several decades of the two-proton decay lifetime due to the exponential energy dependence in the WKB integral. The known two-proton emitters $x_{2p,\,\text{known}} \equiv \left\{ ^{19}\text{Mg},^{45}\text{Fe},^{48}\text{Ni},^{54}\text{Zn},^{67}\text{Kr} \right\}$ consistently fall within the target lifetime range (5.24). The black dots correspond to nuclei with $p_{2p} > 0.4$, this value of p_{2p} is selected rather than $p_{2p} > 0.5$ is because the criterion (5.25) is slightly more restrictive than the single-value energy criterion previously adopted in Ref. [201].

We predict the most promising candidates for *true* two-proton emission, other than

the known ones $x_{2p,\text{ known}}$, are: ^{30}Ar,^{34}Ca,^{39}Ti,^{42}Cr,^{58}Ge,^{62}Se,^{66}Kr,^{70}Sr,^{74}Zr,^{78}Mo, ^{82}Ru,^{86}Pd,^{90}Cd, and ^{103}Te.

The calculated p_{2p} is very low for nuclei with $Z \geq 54$ that also fall into the lifetime range (5.24). The large Coulomb barriers and the condition of $p_{2p} > 0.4$ which corresponds to low Q_{2p} values, i.e. very long lifetimes, resulted in the small two-proton decay widths.

Many of the very proton-rich nuclei with small p_{2p} values such as ^{131,132}Dy, ^{134,135}Er, and ^{144,145}Hf, are excellent candidates for the direct-decay model of two-proton emission [163].

These findings using the BMA methods are mostly consistent with other predictions. The nuclei ^{39}Ti and ^{42}Cr, are expected to be excellent two-proton decay candidates [204, 205]. The Q_{2p} value predicted in BMA-I is not consistent with the claim that ^{39}Ti primarily decays via β decay by Ref. [186]. Other two-proton decay candidates predicted by BMA-I and discussed in other literature include ^{26}S, $^{29-31}$Ar [206], ^{34}Ca [207], ^{58}Ge, ^{62}Se, and ^{66}Kr [208]. Ref. [202] predicts ^{103}Te to exhibit a competition between alpha decay and two-proton decay, and ^{145}Hf to exhibit competition between α decay and direct-decay model of two-proton emission.

5.6   Quantified limits of the nuclear landscape

The latest project in the series is on the quantified limits of the nuclear landscape [108].

Within the DFT framework, limits of the nuclear landscape were probed by performing global mass surveys using several energy density functionals (EDFs): Skyrme [98, 209, 210], Gogny [53, 211], and covariant [210, 212–214]. The problem however, is that these early studies often lacked uncertainty quantification. In few cases [98, 210, 215], systematic uncertainties have been estimated by combining predictions of several different surveys, and by

performing simple mean averaging.

The Bayesian residual modeling, predictions for the probability of existence $p_{\text{ex}}(Z, N)$ follow closely to the descriptions in Sec. 5.2 and 5.4. Gaussian process was selected as our Bayesian model, using the non-zero mean variance defined in (5.19). Four residual models: one- and two-neutron separation energies (for odd-N and even-N, respectively), one- and two-proton separation energies (for odd-Z and even-Z, respectively) were modeled and trained separately.

For the BMA, we considered eight models based on masses calculated using EDFs under the HFB framework (Sec. 2.1.3). Masses from the odd-Z and odd-N nuclei were calculated using Eq. (5.14). The more phenomenological mass models FRDM-2012 [169] and HFB-24 [170] are also included.

Two variants of weight were used for the BMA, each focusing on data from either the neutron-rich (BMA(n)) or the proton-rich (BMA(p)) nuclear regions, following similar methods described in Sec. 5.4 and 5.5. In order to assess the nuclear landscape, we also applied a third BMA variant which assigned local model averaging weights for each nucleus, called BMA($n + p$):

$$w_k(Z, N) = w_k(n) H \left[N \geqslant N_\beta(Z) \right] + w_k(p) H \left[N < N_\beta(Z) \right], \qquad (5.26)$$

where $H(x)$ is the Heaviside step function and $N_\beta(Z)$ is the neutron number corresponding to the average line of β stability defined as in Ref. [216].

The resulting model weights for BMA(n) and BMA(p) are shown in Table 5.3. We can see that BMA(n) is well balanced while BMA(p) is more selective, which penalizes large deviations at single data points.

Table 5.3: Model posterior weights obtained in the variants BMA(n) and BMA(p) of our BMA calculations. For compactness, the following abbreviations are used: UNEn=UNEDFn (n=0,1,2) and FRDM=FRDM-2012. (Table taken from Ref. [108])

BMA variant	SkM*	SkP	SLy4	SV-min	UNE0	UNE1	UNE2	BCPM	D1M	FRDM	HFB-24
BMA(n)	0.10	0.10	0.06	0.11	0.12	0.10	0.09	0.06	0.04	0.12	0.09
BMA(p)	0.00	0.03	0.08	0.05	0.04	0.14	0.12	0.04	0.16	0.17	0.17

By design, the local variant BMA($n+p$) performs the best, since it evaluates each model according to their local quality, i.e. when assigning model weights on the neutron-rich side of the nuclear chart - models that are more accurate in predicting neutron separation energies shouldn't be penalized for their poor performance in predicting two-proton emitters. In practice, all three BMA variants perform similarly in terms of posterior rms deviation ($S_{1n} \approx$ 302keV, $S_{2n} \approx 453$keV, $S_{1p} \approx 410$keV, $S_{2p} \approx 438$keV) when using AME2016-AME2003 (Sec. 5.3.1) as the testing set. These BMA weights can also help us assess the predictive power of different theory models after GP correction: UNEDF0, FRDM-2012, and SV-min have higher predictive power on the neutron-rich side while FRDM-2012, HFB-24, and D1M performs better on the proton-rich side.

In the entire nuclear landscape, the probability of existence p_{ex} is defined slightly differently as:

$$p_{\text{ex}} = p\left(S^*_{1p/2p} > 0 \mid S_{1p/2p}\right) p\left(S^*_{1n/2n} > 0 \mid S_{1n/2n}\right), \tag{5.27}$$

where $p\left(S^*_{1p/2p} > 0 \mid S_{1p/2p}\right)$ was obtained with BMA(p) and $p\left(S^*_{1n/2n} > 0 \mid S_{1n/2n}\right)$ with BMA(n). In practice, one of these two probabilities is always ≈ 1, as one would expect the proton separation energies for neutron-rich nuclei to be well above zero and vice versa.

Plotting p_{ex} for the entire nuclear landscape gave us the quantified limit of the nuclear landscape shown in Fig. 5.12. The drip-line corresponds to $p_{\text{ex}} = 0.5$, and the ranges of
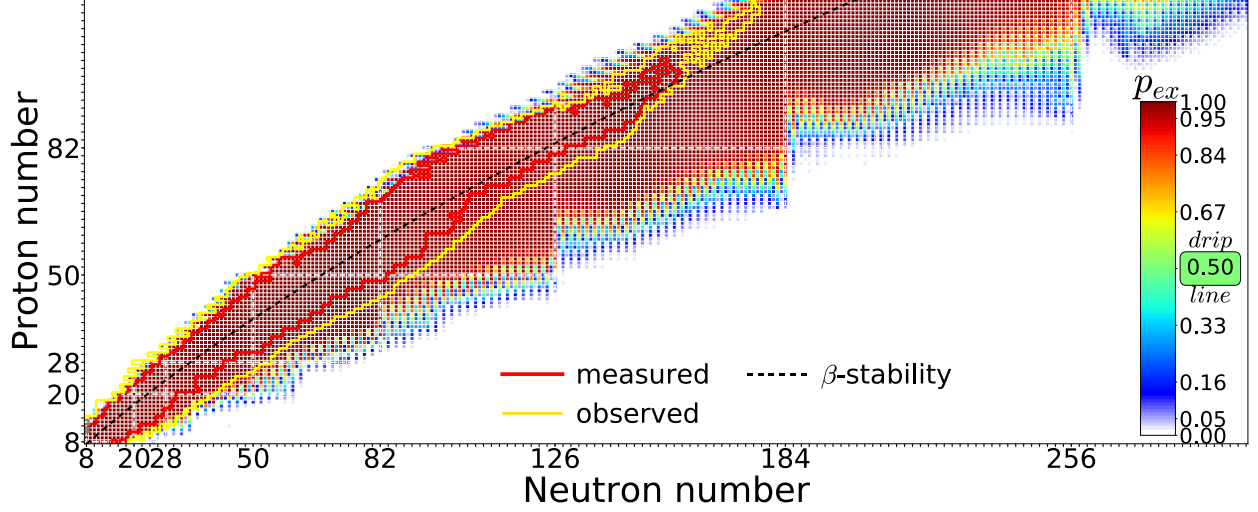
Figure 5.12: The quantified landscape of nuclear existence obtained in our BMA calculations. High-resolution of this figure can be found in Ref. [217]. For every nucleus with $Z, N \geqslant 8$ and $Z \leqslant 119$ the probability of existence p_{ex} (5.27), i.e., the probability that the nucleus is bound with respect to proton and neutron decay, is marked. The domains of nuclei which have been experimentally observed and whose separation energies have been measured (and used for training) are indicated. To provide a realistic estimate of the discovery potential with modern radioactive ion-beam facilities, the isotopes within FRIB's experimental reach are marked. The magic numbers are shown by straight (white) dashed lines, and the average line of β-stability defined as in Ref. [216] is marked by a (black) dashed line. In our estimates, we assumed the experimental limit for the confirmation of existence of an isotope to be 1 event/2.5 days. (Figure taken from Ref. [108])

nuclear mass measurements and known nuclei are marked. According to the BMA$(n + p)$ variant of model averaging, we find the number of particle-bound nuclei with $Z, N \geqslant 8$ and $Z \leqslant 119$ to be 7708 ± 534.

On the proton-rich side of the landscape, we can see that many heavy proton-unstable nuclei will be reached by FRIB, which could test our predictions for the two-proton emitters (Sec. 5.5.2). On the neutron-rich side, FRIB could also examine our p_{ex} predictions for the neutron unstable systems in the light to medium mass region.

5.7 Summary: Bayesian machine learning

In this chapter, we started by introducing the method of using Bayesian neural networks (BNN) and Gaussian process (GP) to emulate the residuals of the two neutron separation energy as a way to improve theory models' predictability. The resulting probabilistic description of the modeled residuals gave us a way to quantify the systematic model uncertainty of the separation energy predictions. This lead to the concept of the probability of existence p_{ex}, which states the probability of a near drip-line nucleus to have a positive separation energy. We also concluded that the Gaussian process is a better approach compared to BNN to in modeling the separation energy residuals, due to its emphasis on the short-range correlations.

Using the notion of p_{ex}, we performed an uncertainty-quantified analysis of the neutron drip-line in the Ca region, and presented a probabilistic description for the one- and two-neutron drip-line. We also introduced Bayesian model averaging (BMA) techniques.

Following the neutron drip-line analysis in the Ca region, we set our eyes onto the proton drip-line, and further experimented with various BMA weighting methods. We also used the prediction for the one- and two-proton separation energy to provide predictions for potential two-proton emitters, in addition to the uncertainty-quantified proton drip-line predictions in the medium-mass region. In this project, we also included a non-zero mean random variable into our GP for the first time, which reduced the theory models' rms deviation by an additional 15% compared with the initial 25% reduction brought by the GP.

Finally, we expanded the Bayesian techniques developed in the first three projects to the entire nuclear landscape, and provided probability of existence predictions for all nuclei with $Z, N \geqslant 8$ and $Z \leqslant 119$. For all even-even, even-odd, and odd-odd systems, our model

predicted 7708 ± 534 nuclei have probability of existence greater than 0.5. We hope this quantified limit of the nuclear landscape can provide a guide for experimental research at next-generation rare isotope facility including the FRIB facility on MSU campus that will soon become operational.

Chapter 6

Conclusions and Outlook

This dissertation consists of two parts: the applications of nuclear DFT to predict ground state nuclear properties on a large scale, and the applications of Bayesian machine learning techniques in nuclear physics. The common theme is large-scale DFT calculations of nuclear properties across the nuclear landscape aided by high-performance computing.

6.1 Octupole deformations and intrinsic Schiff moments

The global survey of octupole-deformed even-even nuclei was performed using nuclear DFT, in particular the Skyrme HFB theory. This served as a precursor to the second project, which was the computation of intrinsic Schiff moments in the vicinity of robust candidates for octupole-deformed even-even nuclei.

In the global octupole survey discussed in Ch. 3, results from five Skyrme EDFs and four covariant EDFs were combined to present the landscape of octupole multiplicity; this gave us a less model-biased prediction of the octupole deformations in even-even nuclei. We have confirmed that enhanced octupole instability mostly occur in the neutron-deficient actinide region and the superheavy actinides with $N \geq 182$, where the latter is far from current experimental reach. Among nuclei in the neutron-deficient actinide region, we predicted the largest octupole deformations in $^{224,226}\mathrm{Ra}$, $^{226,228}\mathrm{Th}$, $^{224,226,228}\mathrm{U}$, $^{226,228,230}\mathrm{Pu}$, and $^{228,230}\mathrm{Cm}$.

By looking at the octupole deformation energy ΔE_{oct} in the octupole-deformed nuclei, we were also able to qualitatively determine the rigidness of octupole deformation. For instance, although the predicted β_3 for lanthanide nuclei such as ^{144,146}Ba, ^{146,148}Ce, and ^{146,148}Nd are large and comparable in β_3 to Ra and Th isotopes, their average values of ΔE_{oct} of less than 0.5 MeV imply very shallow octupole minima, and suggest that octupole deformations are not rigid. However, large octupole correlations are still expected for these lanthanide nuclei, which could be reflected in the enhanced $E1$ and $E3$ transition strengths that in many cases have been measured. We also realize that beyond-DFT effects, crucial for soft systems, can play an important role in the lanthanide region nuclei, which could enhance the theoretical predictions of octupole deformation in this region [218].

The global octupole deformation survey helped us to determine the best candidates to conduct Schiff moment in the neutron-deficient actinide region. A list of promising candidates for the atomic EDM measurement are presented in Table. 4.1.

6.2 Bayesian machine learning

Chapter 5 is a summary of the works done between 2018 and 2020, which involved using Bayesian machine learning techniques to produce uncertainty-quantified predictions of nuclear stability.

We began with using the Bayesian statistical models BNN and GP to produce emulators for the $S_{2\text{n}}$ residuals of the theory predictions compared with experimental data. This served as a pilot study to determine which statistical model is better for modeling the separation energy residuals, and what improvements can be made to achieve better performance. It was determined that the GP model, which has a larger emphasis on short-range correlations,

is more suited for the modeling of the separation energy residuals, and is also more stable from a computational viewpoint.

The second project focused on the detailed analysis of the neutron drip-line in the calcium region by means of Bayesian model averaging techniques. The concept of probability of existence p_{ex} of a nucleus was introduced in this project by evaluating the probability of a nucleus to have a positive separation energy.

We then studied the proton drip-line and made predictions for two-proton ($2p$) emitters. We emphasized experimenting with different variants of the weights for BMA. A non-zero mean GP was also introduced in this project, which increased model performance from an average of 25% to 40% rms deviation reduction.

Finally, we expanded the prediction of p_{ex} to include all nuclei with $Z, N \geqslant 8$ and $Z \leqslant 119$, and performed BMA for eleven theory + GP models. This resulted in the quantified limit of the nuclear landscape (Fig. 5.12) which predicted the number of particle-bound nuclei with $Z, N \geqslant 8$ and $Z \leqslant 119$ to be 7708 ± 534. We also hope the estimates of the drip-lines could guide experimental research for the discovery of exotic isotopes at FRIB and other next-generation rare isotope facilities.

6.3   Outlook

Despite the many exciting results presented in this dissertation, much more awaits to be done.

The calculation performed for odd systems in this dissertation employed approximated blocking methods, which lacks key inputs from the time-odd terms of the Skyrme interaction. This can be overcome by using the latest version of the solver HFODD (v2.73y). However,

this can be computationally expensive as HFODD is symmetry-unconstrained. As a versatile solver, HFODD could also benefit from a re-design of the user interface, as well as incorporating additional parallel programming to promote wider use and broader applications. Global minima calculations can also benefit from machine learning tools.

The Schiff moment calculation presented here is limited to the evaluation of the intrinsic Schiff moment. This can be expanded to include the effects of P-, T-violating potential - such functionality has already been implemented in HFODD, but was not investigated in this dissertation. The calculation of parity doublets using beyond mean-field methods, including restoration of intrinsically-broken symmetries, is also crucial in determining the magnitude of Schiff moment, albeit challenging. In the first step, one could limit the scope of calculations to the robust octupole-deformed odd-mass and odd-odd systems, by performing a global survey of the odd systems with the full blocking method.

The application of Bayesian machine learning in nuclear physics will likely become a major focus, with great potential for discoveries [219]. Here, one should always keep an eye open for new technologies, and be well informed of the latest developments.

APPENDICES

Appendix A: Supplementary Tables

Table A.1: ΔE_{oct} (MeV) and β_3 (in parentheses) values calculated using five Skyrme EDFs: UNEDF0, UNEDF1, UNEDF2, SLy4, and SV-min. See (2.34) and (3.2) for definitions of β_3 and ΔE_{oct}, respectively. Nuclei with at least three Skyrme EDFs predicting them as octupole-deformed are shown.

N	A	UNEDF0	UNEDF1	UNEDF2	SLy4	SV-min
Z = 56 (Ba)						
56	112		0.09 (0.07)	0.36 (0.12)	0.08 (0.07)	
88	144	0.04 (0.04)		0.56 (0.11)	0.5 (0.11)	0.15 (0.07)
90	146	0.08 (0.06)	0.2 (0.09)	0.48 (0.12)	0.48 (0.12)	0.18 (0.08)
Z = 58 (Ce)						
86	144			0.51 (0.09)	0.27 (0.09)	0.05 (0.04)
88	146		0.37 (0.1)	0.9 (0.13)	0.55 (0.12)	0.22 (0.08)
90	148		0.25 (0.11)	0.45 (0.14)	0.14 (0.12)	0.09 (0.08)
Z = 60 (Nd)						
86	146		0.24 (0.08)	0.75 (0.1)	0.23 (0.09)	0.05 (0.04)
88	148		0.3 (0.1)	1.15 (0.14)	0.35 (0.11)	0.08 (0.06)
136	196		0.03 (0.03)	0.07 (0.06)	1.03 (0.14)	0.28 (0.1)
138	198		0.07 (0.06)		0.5 (0.15)	0.3 (0.1)
Z = 62 (Sm)						
132	194		0.05 (0.03)	0.51 (0.08)	0.62 (0.1)	0.1 (0.05)
134	196		0.24 (0.08)	0.79 (0.11)	1.05 (0.14)	0.38 (0.1)
136	198		0.35 (0.1)	0.89 (0.12)	1.28 (0.15)	0.46 (0.12)

N	A	UNEDF0	UNEDF1	UNEDF2	SLy4	SV-min
Z = 64 (Gd)						
132	196		0.34 (0.08)	1.06 (0.11)	0.87 (0.12)	0.25 (0.07)
134	198		0.59 (0.11)	1.45 (0.13)	1.02 (0.15)	0.53 (0.11)
136	200		0.45 (0.13)	1.21 (0.15)	0.81 (0.16)	0.33 (0.12)
Z = 66 (Dy)						
132	198		0.37 (0.09)	1.36 (0.12)	0.86 (0.12)	0.24 (0.07)
134	200		0.52 (0.12)	1.68 (0.14)	0.5 (0.14)	0.29 (0.1)
136	202		0.15 (0.14)	1.13 (0.16)	0.28 (0.13)	
Z = 68 (Er)						
132	200		0.17 (0.08)	1.21 (0.12)	0.18 (0.1)	0.05 (0.05)
134	202		0.17 (0.1)	1.36 (0.15)	0.05 (0.08)	
Z = 86 (Rn)						
132	218	0.86 (0.1)	0.24 (0.07)	0.6 (0.09)	0.52 (0.09)	0.36 (0.08)
134	220	0.95 (0.12)	0.31 (0.09)	0.2 (0.11)	0.67 (0.11)	0.47 (0.1)
136	222	0.88 (0.12)	0.15 (0.09)		0.56 (0.12)	0.33 (0.1)
138	224	0.55 (0.12)			0.26 (0.09)	0.1 (0.07)
192	278	0.04 (0.04)		0.19 (0.05)	0.13 (0.05)	
194	280	0.18 (0.07)		0.01 (0.06)	0.36 (0.1)	
196	282	0.25 (0.09)			0.36 (0.11)	0.03 (0.04)
Z = 88 (Ra)						
130	218	0.91 (0.1)	0.47 (0.07)		0.79 (0.09)	0.63 (0.08)
132	220	1.24 (0.12)	1.07 (0.11)	1.41 (0.12)	1.58 (0.12)	1.14 (0.11)
134	222	1.41 (0.14)	1.27 (0.13)	1.48 (0.14)	1.81 (0.14)	1.33 (0.13)
136	224	1.24 (0.14)	1.01 (0.14)	0.84 (0.14)	1.65 (0.15)	1.1 (0.14)
138	226	0.77 (0.14)	0.51 (0.13)	0.09 (0.08)	1.17 (0.15)	0.61 (0.13)
140	228	0.29 (0.1)	0.12 (0.07)		0.42 (0.11)	0.16 (0.08)
192	280	0.65 (0.09)		0.25 (0.05)	1.02 (0.11)	0.58 (0.08)
194	282	0.91 (0.11)		0.0 (0.04)	1.51 (0.13)	0.75 (0.11)
196	284	0.97 (0.12)	0.28 (0.09)		1.58 (0.14)	0.79 (0.12)
198	286	0.79 (0.12)	0.22 (0.08)		0.9 (0.14)	0.49 (0.11)
200	288	0.45 (0.12)	0.12 (0.06)		0.19 (0.07)	0.13 (0.07)

N	A	UNEDF0	UNEDF1	UNEDF2	SLy4	SV-min

Z = 90 (Th)

N	A	UNEDF0	UNEDF1	UNEDF2	SLy4	SV-min
130	220	0.96 (0.11)	0.99 (0.1)	0.38 (0.09)	1.25 (0.11)	1.05 (0.1)
132	222	1.21 (0.13)	1.66 (0.13)	2.3 (0.14)	1.91 (0.13)	1.56 (0.13)
134	224	1.16 (0.14)	1.72 (0.15)	2.28 (0.16)	1.85 (0.15)	1.54 (0.15)
136	226	0.72 (0.15)	1.13 (0.16)	1.2 (0.16)	1.19 (0.17)	0.99 (0.15)
138	228	0.18 (0.13)	0.46 (0.15)	0.25 (0.15)	0.63 (0.17)	0.33 (0.15)
192	282	1.04 (0.11)		0.45 (0.06)	1.66 (0.12)	1.09 (0.11)
194	284	1.25 (0.13)	0.99 (0.12)	0.3 (0.07)	2.11 (0.14)	1.41 (0.13)
196	286	1.11 (0.14)	1.14 (0.13)		1.91 (0.16)	1.3 (0.14)
198	288	0.62 (0.14)	0.81 (0.13)		1.06 (0.16)	0.75 (0.14)
200	290	0.05 (0.12)	0.3 (0.11)			0.11 (0.12)

Z = 92 (U)

N	A	UNEDF0	UNEDF1	UNEDF2	SLy4	SV-min
130	222	0.79 (0.11)	1.35 (0.12)	0.39 (0.11)	1.46 (0.12)	1.25 (0.11)
132	224	0.81 (0.13)	1.8 (0.14)	2.54 (0.15)	1.83 (0.14)	1.49 (0.14)
134	226	0.52 (0.14)	1.48 (0.16)	2.08 (0.17)	1.46 (0.16)	1.19 (0.15)
136	228		0.73 (0.17)	0.87 (0.17)	0.59 (0.17)	0.51 (0.16)
138	230		0.14 (0.15)	0.05 (0.16)	0.15 (0.17)	
190	282	0.89 (0.1)			0.66 (0.11)	0.16 (0.09)
192	284	1.04 (0.12)	0.23 (0.11)	0.53 (0.08)	2.03 (0.14)	1.53 (0.12)
194	286	1.04 (0.13)	1.49 (0.13)	0.69 (0.09)	2.24 (0.15)	1.65 (0.14)
196	288	0.7 (0.14)	1.51 (0.14)	0.38 (0.09)	1.67 (0.17)	1.21 (0.15)
198	290	0.09 (0.13)	0.76 (0.15)		0.8 (0.17)	0.5 (0.15)

Z = 94 (Pu)

N	A	UNEDF0	UNEDF1	UNEDF2	SLy4	SV-min
130	224	0.44 (0.11)	1.61 (0.13)	1.58 (0.12)	1.56 (0.13)	1.29 (0.12)
132	226	0.3 (0.11)	1.58 (0.15)	3.26 (0.15)	1.35 (0.15)	1.06 (0.14)
134	228	0.04 (0.1)	0.91 (0.16)	1.42 (0.17)	0.85 (0.16)	0.62 (0.15)
136	230		0.32 (0.16)	0.33 (0.17)	0.4 (0.16)	0.2 (0.14)
190	284	0.9 (0.11)	0.77 (0.09)	1.68 (0.09)	1.93 (0.12)	1.0 (0.11)
192	286	0.74 (0.12)	1.71 (0.12)	2.16 (0.11)	2.42 (0.14)	1.92 (0.13)
194	288	0.55 (0.13)	2.06 (0.14)	1.76 (0.12)	2.16 (0.16)	1.59 (0.15)
196	290	0.19 (0.12)	1.4 (0.16)	0.94 (0.12)	1.24 (0.17)	0.85 (0.16)
198	292		0.4 (0.16)	0.43 (0.15)	0.29 (0.18)	0.07 (0.15)

N	A	UNEDF0	UNEDF1	UNEDF2	SLy4	SV-min
Z = 96 (Cm)						
128	224	0.31 (0.07)	0.37 (0.08)	0.6 (0.08)	0.45 (0.09)	0.15 (0.07)
130	226	0.05 (0.1)	1.73 (0.14)	3.11 (0.13)	1.57 (0.14)	1.21 (0.13)
132	228		1.22 (0.16)	3.23 (0.16)	0.83 (0.15)	0.5 (0.15)
134	230		0.36 (0.17)	0.98 (0.18)	0.31 (0.16)	
188	284	0.69 (0.09)	1.03 (0.09)	1.85 (0.09)	1.6 (0.11)	0.53 (0.08)
190	286	0.83 (0.11)	2.4 (0.12)	3.19 (0.12)	2.93 (0.14)	1.92 (0.12)
192	288	0.36 (0.12)	2.45 (0.14)	3.62 (0.13)	2.67 (0.15)	2.15 (0.14)
194	290	0.07 (0.1)	2.12 (0.15)	2.91 (0.14)	2.05 (0.17)	1.45 (0.15)
196	292		1.28 (0.17)	1.92 (0.15)	1.11 (0.18)	0.62 (0.16)
198	294		0.29 (0.17)	0.7 (0.16)	0.2 (0.18)	
Z = 98 (Cf)						
128	226	0.26 (0.07)	0.86 (0.1)	1.38 (0.1)	0.96 (0.1)	0.46 (0.08)
130	228		1.67 (0.14)	3.32 (0.14)	1.49 (0.14)	0.82 (0.13)
132	230		0.71 (0.17)	2.76 (0.17)	0.53 (0.16)	
186	284	0.01 (0.02)	0.45 (0.07)	0.77 (0.08)	0.86 (0.09)	0.21 (0.06)
188	286	0.8 (0.09)	1.82 (0.11)	2.75 (0.11)	2.47 (0.12)	1.25 (0.1)
190	288	0.74 (0.11)	2.7 (0.13)	3.71 (0.13)	3.28 (0.14)	2.61 (0.13)
192	290	0.07 (0.1)	2.46 (0.15)	4.0 (0.15)	2.68 (0.16)	2.06 (0.15)
194	292		1.93 (0.17)	3.1 (0.16)	1.95 (0.17)	1.32 (0.16)
196	294		1.29 (0.17)	1.84 (0.17)	1.26 (0.18)	0.55 (0.17)
198	296		0.46 (0.17)	0.7 (0.18)	0.35 (0.18)	
Z = 100 (Fm)						
126	226		0.17 (0.05)	0.42 (0.07)	0.33 (0.06)	0.03 (0.03)
128	228	0.16 (0.06)	1.05 (0.11)	1.67 (0.11)	1.17 (0.1)	0.58 (0.09)
130	230		1.28 (0.15)	2.76 (0.15)	1.22 (0.15)	
132	232		0.27 (0.17)	2.32 (0.18)	0.35 (0.16)	
184	284		0.09 (0.04)	0.19 (0.06)	0.45 (0.07)	0.02 (0.02)
186	286	0.1 (0.04)	0.75 (0.09)	1.1 (0.09)	1.29 (0.1)	0.48 (0.07)
188	288	0.79 (0.09)	2.08 (0.12)	2.74 (0.12)	2.8 (0.13)	1.52 (0.11)
190	290	0.61 (0.11)	2.61 (0.14)	3.83 (0.14)	3.21 (0.15)	2.42 (0.14)
192	292		2.2 (0.16)	3.86 (0.16)	2.5 (0.17)	1.84 (0.15)
194	294		1.59 (0.17)	2.86 (0.17)	1.65 (0.18)	1.09 (0.17)
196	296		1.07 (0.18)	1.47 (0.18)	1.17 (0.18)	0.39 (0.16)
198	298		0.38 (0.17)	0.47 (0.18)	0.24 (0.17)	

N	A	UNEDF0	UNEDF1	UNEDF2	SLy4	SV-min
Z = 102 (No)						
128	230	0.05 (0.04)	0.87 (0.11)	1.47 (0.11)	0.9 (0.1)	0.45 (0.08)
184	286		0.14 (0.05)	0.25 (0.06)	0.48 (0.08)	0.06 (0.04)
186	288	0.1 (0.04)	0.76 (0.09)	1.09 (0.1)	1.22 (0.1)	0.49 (0.08)
188	290	0.63 (0.08)	1.98 (0.12)	2.47 (0.13)	2.53 (0.13)	1.37 (0.11)
190	292	0.38 (0.11)	2.39 (0.15)	3.72 (0.15)	2.92 (0.16)	2.0 (0.14)
192	294		1.9 (0.17)	3.61 (0.17)	1.46 (0.18)	1.08 (0.16)
194	296		1.07 (0.17)	2.55 (0.18)	0.15 (0.18)	0.29 (0.16)
Z = 104 (Rf)						
184	288		0.09 (0.05)	0.19 (0.06)	0.29 (0.07)	0.02 (0.02)
186	290	0.03 (0.03)	0.57 (0.09)	0.86 (0.09)	0.86 (0.09)	0.32 (0.07)
188	292	0.39 (0.07)	1.66 (0.12)	2.1 (0.13)	1.94 (0.13)	1.0 (0.1)
190	294	0.1 (0.1)	1.91 (0.15)	2.64 (0.16)	1.25 (0.16)	0.53 (0.14)
Z = 106 (Sg)						
184	290		0.01 (0.02)	0.06 (0.04)	0.07 (0.05)	
186	292		0.33 (0.07)	0.57 (0.08)	0.45 (0.08)	0.14 (0.06)
188	294	0.15 (0.05)	0.74 (0.12)	0.47 (0.13)	0.4 (0.12)	0.45 (0.09)

Table A.2: Proton quadrupole $Q_{20}(\text{fm}^2)$ and octupole $Q_{30}(\text{fm}^3)$ moments (in parentheses) for octupole-deformed even-even nuclei with predicted $\beta_3 \geq 0.01$ from five Skyrme EDFs: UNEDF0, UNEDF1, UNEDF2, SLy4, and SV-min. See (2.33) for definitions of Q_{20}, Q_{30}. The proton multipole moments closely resemble charge multipole moments, and can be used to compare with experimental data derived from transition strengths. Average values are shown in the rightmost column. All values rounded to integers.

N	A	UNEDF0	UNEDF1	UNEDF2	SLy4	SV-min	Average
Z = 56 (Ba)							
56	112		352 (524)	360 (862)	351 (485)		354 (623)
88	144	292 (339)		306 (952)	330 (932)	310 (593)	309 (704)
90	146	333 (496)	356 (789)	359 (1058)	368 (1048)	352 (705)	353 (819)
Z = 58 (Ce)							
86	144			248 (818)	295 (776)	275 (369)	272 (654)
88	146		346 (950)	323 (1182)	363 (1086)	347 (779)	344 (999)
90	148		405 (1046)	396 (1308)	425 (1150)	418 (775)	411 (1069)
Z = 60 (Nd)							
86	146		277 (804)	227 (991)	297 (834)	286 (430)	271 (764)
88	148		373 (1007)	308 (1344)	400 (1026)	393 (608)	368 (996)
136	196		258 (409)	155 (640)	369 (1666)	339 (1113)	280 (957)
138	198		297 (743)		431 (1779)	390 (1188)	372 (1236)
Z = 62 (Sm)							
132	194		170 (430)	166 (1019)	209 (1287)	176 (573)	180 (827)
134	196		223 (1024)	197 (1354)	289 (1676)	264 (1201)	243 (1313)
136	198		263 (1297)	207 (1532)	367 (1897)	339 (1418)	294 (1536)
Z = 64 (Gd)							
132	196		184 (1127)	174 (1491)	186 (1516)	169 (958)	178 (1273)
134	198		225 (1501)	200 (1781)	279 (1893)	251 (1436)	238 (1652)
136	200		264 (1744)	205 (1957)	385 (2025)	357 (1551)	302 (1819)
Z = 66 (Dy)							
132	198		196 (1328)	177 (1738)	186 (1634)	165 (1010)	181 (1427)
134	200		241 (1728)	197 (2050)	310 (1892)	271 (1440)	254 (1777)
136	202		307 (1947)	194 (2251)	437 (1824)		312 (2007)

N	A	UNEDF0	UNEDF1	UNEDF2	SLy4	SV-min	Average
Z = 68 (Er)							
132	200		223 (1195)	183 (1824)	210 (1498)	199 (711)	203 (1307)
134	202		307 (1529)	192 (2185)	396 (1073)		298 (1595)
Z = 86 (Rn)							
132	218	351 (2152)	382 (1453)	293 (1781)	411 (1799)	374 (1593)	362 (1755)
134	220	431 (2440)	463 (1896)	414 (2270)	476 (2196)	452 (1987)	447 (2157)
136	222	488 (2618)	524 (1921)		531 (2378)	511 (2043)	513 (2240)
138	224	538 (2573)			582 (1927)	563 (1458)	561 (1986)
192	278	359 (928)		226 (1198)	370 (1183)		318 (1103)
194	280	443 (1703)		291 (1386)	482 (2293)		405 (1794)
196	282	498 (2079)			550 (2644)	482 (1055)	510 (1926)
Z = 88 (Ra)							
130	218	349 (2142)	362 (1531)		408 (1935)	362 (1669)	370 (1819)
132	220	472 (2650)	497 (2389)	445 (2617)	515 (2547)	489 (2430)	483 (2526)
134	222	556 (2957)	579 (2814)	559 (3068)	587 (2973)	569 (2806)	570 (2923)
136	224	619 (3144)	649 (3033)	637 (3145)	648 (3253)	633 (2990)	637 (3113)
138	226	682 (3053)	712 (2783)	692 (1821)	708 (3224)	694 (2791)	697 (2734)
140	228	752 (2310)	770 (1595)		756 (2376)	750 (1846)	757 (2031)
192	280	504 (2442)		249 (1300)	508 (2706)	442 (1990)	425 (2109)
194	282	577 (2890)		336 (1072)	599 (3333)	558 (2755)	517 (2512)
196	284	633 (3154)	580 (2173)		668 (3674)	631 (3051)	628 (3013)
198	286	683 (3264)	651 (2129)		724 (3637)	694 (2902)	688 (2983)
200	288	735 (3106)	716 (1589)		780 (1987)	755 (1982)	746 (2166)
Z = 90 (Th)							
130	220	424 (2467)	430 (2240)	345 (2027)	461 (2432)	434 (2283)	418 (2289)
132	222	557 (2950)	564 (2919)	510 (3071)	580 (3010)	562 (2915)	554 (2973)
134	224	649 (3273)	660 (3352)	635 (3530)	662 (3459)	652 (3294)	651 (3381)
136	226	725 (3426)	735 (3592)	723 (3720)	734 (3749)	726 (3493)	728 (3596)
138	228	806 (3063)	809 (3475)	798 (3423)	804 (3734)	798 (3338)	803 (3406)
192	282	582 (3045)		177 (1461)	558 (3280)	524 (2922)	460 (2677)
194	284	663 (3457)	603 (3097)	235 (1722)	661 (3841)	633 (3484)	559 (3120)
196	286	728 (3723)	690 (3469)		740 (4235)	713 (3791)	717 (3804)
198	288	788 (3801)	761 (3517)		802 (4383)	782 (3811)	783 (3878)
200	290	859 (3476)	831 (3168)			855 (3206)	848 (3283)

N	A	UNEDF0	UNEDF1	UNEDF2	SLy4	SV-min	Average
Z = 92 (U)							
130	222	473 (2640)	450 (2673)	356 (2437)	477 (2782)	462 (2653)	443 (2637)
132	224	628 (3058)	600 (3304)	526 (3386)	619 (3344)	610 (3249)	596 (3268)
134	226	739 (3301)	719 (3717)	682 (3884)	726 (3782)	725 (3603)	718 (3657)
136	228		819 (3940)	798 (4085)	818 (4045)	820 (3735)	813 (3951)
138	230		913 (3691)	898 (3747)	907 (3892)		906 (3776)
190	282	503 (2884)			403 (3003)	340 (2415)	415 (2767)
192	284	629 (3396)	498 (3075)	159 (1982)	566 (3706)	543 (3427)	479 (3117)
194	286	727 (3763)	640 (3739)	185 (2285)	690 (4257)	667 (3948)	581 (3598)
196	288	810 (3972)	741 (4125)	187 (2292)	784 (4657)	764 (4263)	657 (3861)
198	290	896 (3804)	828 (4249)		863 (4838)	853 (4277)	860 (4292)
Z = 94 (Pu)							
130	224	509 (2667)	439 (3015)	340 (2769)	458 (3058)	456 (2923)	440 (2886)
132	226	711 (2760)	607 (3621)	484 (3597)	633 (3592)	647 (3486)	616 (3411)
134	228	857 (2384)	774 (3988)	690 (4182)	793 (3940)	809 (3696)	784 (3638)
136	230		915 (4011)	877 (4278)	922 (3957)	939 (3314)	913 (3890)
190	284	497 (3163)	316 (2714)	230 (2540)	384 (3470)	362 (3069)	357 (2991)
192	286	654 (3574)	490 (3639)	283 (3050)	537 (4074)	525 (3814)	497 (3630)
194	288	787 (3779)	627 (4213)	314 (3346)	674 (4571)	664 (4303)	613 (4042)
196	290	910 (3532)	741 (4587)	370 (3525)	792 (4983)	788 (4603)	720 (4246)
198	292		857 (4707)	688 (4276)	909 (5125)	921 (4395)	843 (4625)
Z = 96 (Cm)							
128	224	193 (1769)	184 (2052)	155 (1916)	189 (2113)	125 (1621)	169 (1894)
130	226	564 (2334)	417 (3334)	345 (3174)	417 (3308)	428 (3150)	434 (3060)
132	228		600 (3942)	453 (3863)	629 (3855)	674 (3642)	589 (3825)
134	230		821 (4165)	635 (4434)	845 (3893)		767 (4164)
188	284	267 (2596)	238 (2681)	243 (2834)	251 (3105)	175 (2408)	234 (2724)
190	286	465 (3372)	368 (3539)	330 (3514)	372 (3933)	353 (3529)	377 (3577)
192	288	671 (3591)	487 (4177)	378 (3961)	499 (4460)	496 (4167)	506 (4071)
194	290	879 (2864)	614 (4667)	420 (4290)	651 (4904)	651 (4646)	643 (4274)
196	292		734 (5022)	490 (4574)	788 (5311)	799 (4902)	702 (4952)
198	294		873 (5111)	666 (4924)	935 (5342)		824 (5125)

Table A.2 (*cont′d*)

N	A	UNEDF0	UNEDF1	UNEDF2	SLy4	SV-min	Average

Z = 98 (Cf)

N	A	UNEDF0	UNEDF1	UNEDF2	SLy4	SV-min	Average
128	226	166 (1718)	195 (2568)	193 (2613)	173 (2519)	139 (2119)	173 (2307)
130	228		404 (3672)	361 (3606)	380 (3572)	395 (3359)	385 (3552)
132	230		599 (4279)	472 (4269)	615 (4113)		562 (4220)
186	284	7 (575)	116 (2282)	136 (2494)	125 (2709)	56 (1733)	88 (1958)
188	286	228 (2789)	270 (3408)	277 (3513)	255 (3675)	210 (3130)	248 (3303)
190	288	415 (3523)	392 (4155)	372 (4169)	362 (4374)	342 (3938)	376 (4031)
192	290	708 (3223)	517 (4771)	428 (4607)	482 (4896)	484 (4554)	523 (4410)
194	292		652 (5229)	482 (4964)	670 (5336)	659 (5011)	615 (5135)
196	294		771 (5514)	581 (5341)	804 (5653)	814 (5137)	742 (5411)
198	296		897 (5508)	743 (5584)	936 (5568)		858 (5553)

Z = 100 (Fm)

N	A	UNEDF0	UNEDF1	UNEDF2	SLy4	SV-min	Average
126	226		28 (1456)	57 (1887)	31 (1737)	8 (719)	31 (1449)
128	228	130 (1503)	176 (2834)	177 (2947)	133 (2710)	112 (2289)	145 (2456)
130	230		407 (4023)	384 (4041)	365 (3864)		385 (3976)
132	232		606 (4556)	506 (4709)	617 (4347)		576 (4537)
184	284		23 (1430)	44 (1806)	47 (2317)	4 (680)	29 (1558)
186	286	31 (1445)	118 (2825)	133 (2981)	111 (3187)	73 (2429)	93 (2573)
188	288	179 (2853)	260 (3830)	276 (3956)	227 (4034)	192 (3473)	226 (3629)
190	290	359 (3580)	411 (4684)	401 (4702)	360 (4832)	328 (4285)	371 (4416)
192	292		554 (5341)	466 (5161)	493 (5415)	489 (4952)	500 (5217)
194	294		704 (5718)	532 (5550)	703 (5735)	682 (5292)	655 (5573)
196	296		827 (5817)	663 (5963)	831 (5831)	847 (5087)	792 (5674)
198	298		942 (5494)	841 (5873)	949 (5420)		910 (5595)

Z = 102 (No)

N	A	UNEDF0	UNEDF1	UNEDF2	SLy4	SV-min	Average
128	230	78 (947)	140 (2878)	140 (3052)	70 (2640)	61 (2196)	97 (2342)
184	286		16 (1825)	27 (2101)	21 (2508)	7 (1227)	17 (1915)
186	288	17 (1449)	83 (2992)	97 (3154)	66 (3308)	50 (2579)	62 (2696)
188	290	124 (2749)	243 (4082)	271 (4264)	193 (4218)	152 (3571)	196 (3776)
190	292	318 (3480)	421 (5089)	420 (5131)	377 (5270)	324 (4545)	372 (4703)
192	294		558 (5713)	480 (5580)	496 (5835)	494 (5232)	507 (5590)
194	296		733 (5883)	537 (5942)	723 (5838)	719 (5249)	678 (5728)

N	A	UNEDF0	UNEDF1	UNEDF2	SLy4	SV-min	Average
Z = 104 (Rf)							
184	288		-3 (1680)	-6 (2016)	-10 (2288)	0 (839)	-4 (1705)
186	290	1 (923)	39 (2919)	45 (3122)	15 (3165)	17 (2417)	23 (2509)
188	292	64 (2437)	222 (4192)	251 (4443)	162 (4254)	101 (3465)	160 (3758)
190	294	303 (3160)	406 (5299)	407 (5377)	371 (5516)	313 (4643)	360 (4799)
Z = 106 (Sg)							
184	290		-6 (867)	-22 (1504)	-19 (1592)		-15 (1321)
186	292		5 (2621)	0 (2913)	-22 (2792)	-4 (1906)	-5 (2558)
188	294	15 (1830)	194 (4160)	215 (4496)	128 (4152)	48 (3155)	120 (3558)

Table A.3: Reference table to Fig. 5.10: even-Z elements. For each atomic element with even-Z shown are: the neutron number N_0 of the lightest isotope for which an experimental one- or two-proton separation energy value is available; the neutron number N_{obs} of the lightest isotope observed; the neutron number N_{drip} of the predicted drip line isotope in BMA-I; and the neutron number N_{FRIB} marking the reach of FRIB. (Table taken from Ref. [109])

Z	Elem.	N_0	N_{obs}	N_{drip}	N_{FRIB}
16	S	12	11	11	10
18	Ar	14	11	13	12
20	Ca	16	15	15	14
22	Ti	18	17	18	17
24	Cr	21	18	19	18
26	Fe	23	19	20	19
28	Ni	25	20	22	20
30	Zn	28	24	25	23
32	Ge	31	27	28	25
34	Se	33	29	30	28
36	Kr	35	31	32	31
38	Sr	37	35	35	33
40	Zr	40	37	37	35
42	Mo	43	39	39	36
44	Ru	46	41	41	38
46	Pd	48	44	43	40
48	Cd	50	46	45	42
50	Sn	50	49	47	45
52	Te	53	52	53	52
54	Xe	55	54	55	54
56	Ba	58	58	58	57
58	Ce	68	63	60	57
60	Nd	70	65	62	60
62	Sm	73	67	66	63
64	Gd	76	71	69	66
66	Dy	77	73	72	69
68	Er	78	76	75	74
70	Yb	81	79	78	74
72	Hf	84	82	80	77
74	W	86	83	83	80
76	Os	88	85	86	84
78	Pt	90	88	90	87
80	Hg	94	91	94	88
82	Pb	98	96	97	93

Table A.4: Reference table to Fig. 5.10: odd-Z elements. For each atomic element with odd-Z shown are: the neutron number N_0 of the lightest isotope for which an experimental one- or two-proton separation energy value is available; the neutron number N_{obs} of the lightest isotope observed; the neutron number N_{drip} of the predicted drip line isotope in BMA-I; and the neutron number N_{FRIB} marking the reach of FRIB. (Table taken from Ref. [109])

Z	Elem.	N_0	N_{obs}	N_{drip}	N_{FRIB}
17	Cl	14	11	14	14
19	K	16	16	16	16
21	Sc	19	18	19	18
23	V	20	20	20	19
25	Mn	22	21	22	21
27	Co	24	23	24	23
29	Cu	27	26	27	25
31	Ga	30	29	29	28
33	As	33	31	31	31
35	Br	35	34	33	33
37	Rb	37	35	35	35
39	Y	40	37	37	37
41	Nb	42	41	41	39
43	Tc	44	43	43	40
45	Rh	47	44	45	42
47	Ag	49	45	47	44
49	In	51	47	49	47
51	Sb	55	52	55	52
53	I	57	55	57	55
55	Cs	62	57	61	57
57	La	67	60	61	58
59	Pr	69	62	65	61
61	Pm	72	67	68	64
63	Eu	74	67	71	67
65	Tb	76	70	75	69
67	Ho	79	73	78	72
69	Tm	82	76	81	75
71	Lu	85	79	83	76
73	Ta	87	82	87	78
75	Re	91	84	90	81
77	Ir	95	87	93	84
79	Au	97	91	97	87
81	Tl	102	95	102	90

Appendix B: List of my contributions

1. Léo Neufcourt, **Yuchen Cao**, Witold Nazarewicz, and Frederi Viens, *"Bayesian approach to model-based extrapolation of nuclear observables"*, Phys. Rev. C. **98**, 034318 (2018)

   - Produced and compiled nuclear theory and experimental data,

   - Produced Figures 1, 2, 3, 5, and 6.

2. Léo Neufcourt, **Yuchen Cao**, Witold Nazarewicz, Erik Olsen, and Frederi Viens, *"Neutron Drip Line in the Ca Region from Bayesian Model Averaging"*, Phys. Rev. Lett. **1 22**, 062502 (2019)

   - Produced and compiled raw nuclear theory and experimental data,

   - Produced Fig. 1,

   - Contributed to producing the list of all observed isotopes and nuclei with masses measured.

3. Léo Neufcourt, **Yuchen Cao**, Samuel Giuliani, Witold Nazarewicz, Erik Olsen, and Oleg B. Tarasov, *"Beyond the proton drip line: Bayesian analysis of proton-emitting nuclei"*, Phys. Rev. C **101**, 014319 (2020)

- Produced and compiled raw nuclear theory and experimental data,

- Suggested introduction of non-zero mean parameter to the Gaussian process,

- Performed calculations to estimate the lifetimes of true two-proton emitters,

- Produced Fig. 5.

4. Léo Neufcourt, **Yuchen Cao**, Samuel Giuliani, Witold Nazarewicz, Erik Olsen, and Oleg B. Tarasov, *"Quantified limits of the nuclear landscape"*, Phys. Rev. C **101**, 044307 (2020)

  - Produced and compiled raw nuclear theory and experimental data.

5. **Yuchen Cao**, Sylvester E. Agbemava, Anatoli V. Afanasjev, Witold Nazarewicz, and Erik Olsen, *"Landscape of pear-shaped even-even nuclei"*, arXiv:2004.01319 (2020)

  - Performed global Skyrme HFB calculations for octupole-deformed even-even nuclei, including necessary computational developments (see p. 7),

  - Performed calculations of single particle energies in the octupole-deformed region,

  - Wrote the first draft (except for Sec. II(B)),

  - Produced all figures in this paper.

6. MassExplorer

  - Developed source codes (with E. Olsen) for main page of "Plotting Tools" using HTML.

  - Developed source codes (individually) for the "Nuclear Data Search", "Isotope/Isotone/Isobar Chain Plot", "Separation Energy Plot", and "3D Quadrupole Deformation Plot" functionalities using JavaScript.

- Developed source codes (with E. Olsen and A. Savanur) for the "Correlation Plot" functionality using JavaScript.

7. Other contributions

- Implemented dynamic MPI scheduling in HFBTHO (v3.00) masstable mode,

- Introduced Q30 constraints in HFBTHO (v3.00) masstable mode,

- Implemented calculation of Lipkin-Nogami corrected deformations in HFBTHO (v3.00),

- Implemented calculation of intrinsic Schiff moment in HFBTHO (v3.00),

- Developed Python code for automating blocking calculation with HFBTHO,

- Developed Python code for automating blocking calculation with HFODD,

- Developed Python code for automating single particle orbital calculations with HFBTHO,

- Developed Python code for remote status monitoring of large scale survey calculations,

- Served as graduate mentor for the National Science Foundation *Research Experience for Teachers* (RET) program at MSU in summer 2019.

BIBLIOGRAPHY

BIBLIOGRAPHY

[1] E. Rutherford. The scattering of alpha and beta particles by matter and the structure of the atom. *Phil. Mag. Ser. 6*, 21:669–688, 1911.

[2] C. F. v. Weizsäcker. Zur theorie der kernmassen. *Zeitschrift für Phys.*, 96(7-8):431–458, July 1935.

[3] P. Möller, J.R. Nix, W.D. Myers, and W.J. Swiatecki". Nuclear ground-state masses and deformations. *At. Data Nucl. Data Tables*, 59(2):185 – 381, 1995.

[4] P. Möller, R. Bengtsson, B. G. Carlsson, P. Olivius, T. Ichikawa, H. Sagawa, and A. Iwamoto. Axial and reflection asymmetry of the nuclear ground state. *At. Data Nucl. Data Tables*, 94(5):758–780, Sep 2008.

[5] P. Möller and J.R. Nix. Nuclear masses from a unified macroscopic-microscopic model. *Atomic Data and Nuclear Data Tables*, 39(2):213 – 223, 1988.

[6] J. Carlson. Green's function monte carlo study of light nuclei. *Phys. Rev. C*, 36:2026–2033, Nov 1987.

[7] C. Forssén, J. Christensson, P. Navrátil, S. Quaglioni, S. Reimann, J. Vary, and S. Åberg. The Ab Initio No-core Shell Model. *Few-Body Systems*, 45(2-4):111–114, May 2009.

[8] L. Coraggio, A. Covello, A. Gargano, N. Itaco, and T.T.S. Kuo. Shell-model calculations and realistic effective interactions. *Progress in Particle and Nuclear Physics*, 62(1):135 – 182, 2009.

[9] E. Caurier, G. Martínez-Pinedo, F. Nowacki, A. Poves, and A. P. Zuker. The shell model as a unified view of nuclear structure. *Rev. Mod. Phys.*, 77:427–488, Jun 2005.

[10] Michael Bender, Paul-Henri Heenen, and Paul-Gerhard Reinhard. Self-consistent mean-field models for nuclear structure. *Rev. Mod. Phys.*, 75:121–180, Jan 2003.

[11] Jacek Dobaczewski. Current developments in nuclear density functional methods. *Journal of Physics: Conference Series*, 312(9):092002, sep 2011.

[12] Klaus-Peter Lieb. Theodor Schmidt and Hans Kopfermann Pioneers in Hyperfine Physics. *Hyperfine Interactions*, 136(3):783–802, November 2001.

[13] Casimir H.B.G. On the Interaction between Atomic Nuclei and Electrons. *Prize Essay for Teyler's Foundation at Haarlem*, 1936.

[14] H. A. Jahn and E. Teller. Stability of polyatomic molecules in degenerate electronic states. I. orbital degeneracy. *Proc. R. Soc. Lond. A*, 161(905):220–235, Jul 1937.

[15] P.-G. Reinhard and E. W. Otten. Transition to deformed shapes as a nuclear Jahn-Teller effect. *Nucl. Phys. A*, 420(2):173, 1984.

[16] W. Nazarewicz. Microscopic origin of nuclear deformations. *Nucl. Phys. A*, 574:27 – 49, 1994.

[17] Stefan Frauendorf. Spontaneous symmetry breaking in rotating nuclei. *Rev. Mod. Phys.*, 73:463–514, Jun 2001.

[18] V. M. Strutinsky. Remarks about pear-shaped nuclei. *Physica*, 22(6):1166–1167, Jan 1956.

[19] Kiuck Lee and D. R. Inglis. Stability of pear-shaped nuclear deformations. *Phys. Rev.*, 108(3):774–778, Nov 1957.

[20] Sven A.E. Johansson. Nuclear octupole deformation and the mechanism of fission. *Nucl. Phys.*, 22(4):529 – 552, 1961.

[21] P. A. Butler and W. Nazarewicz. Intrinsic reflection asymmetry in atomic nuclei. *Rev. Mod. Phys.*, 68(2):349–421, Apr 1996.

[22] P. A. Butler. Octupole collectivity in nuclei. *J. Phys. G*, 43(7):073002, Jul 2016.

[23] A. Gyurkovich, A. Sobiczewski, B. Nerlo-Pomorska, and K. Pomorski. On the stable octupole deformation of nuclei. *Phys. Lett. B*, 105(2):95 – 98, 1981.

[24] W. Nazarewicz, P. Olanders, I. Ragnarsson, J. Dudek, G.A. Leander, P. Möller, and E. Ruchowska. Analysis of octupole instability in medium-mass and heavy nuclei. *Nucl. Phys. A*, 429(2):269 – 295, 1984.

[25] L. M. Robledo and G. F. Bertsch. Global systematics of octupole excitations in even-even nuclei. *Phys. Rev. C*, 84:054302, Nov 2011.

[26] L M Robledo and R R Rodríguez-Guzmán. Octupole deformation properties of actinide isotopes within a mean-field approach. *J. Phys. G*, 39(10):105103, aug 2012.

[27] M. Warda and J. L. Egido. Fission half-lives of superheavy nuclei in a microscopic approach. *Phys. Rev. C*, 86:014322, Jul 2012.

[28] L M Robledo. Ground state octupole correlation energy with effective forces. *J. Phys. G*, 42(5):055109, 2015.

[29] L. M. Robledo, M. Baldo, P. Schuck, and X. Viñas. Octupole deformation properties of the Barcelona-Catania-Paris energy density functionals. *Phys. Rev. C*, 81:034315, Mar 2010.

[30] J. Erler, K. Langanke, H. P. Loens, G. Martínez-Pinedo, and P.-G. Reinhard. Fission properties for *r*-process nuclei. *Phys. Rev. C*, 85:025802, Feb 2012.

[31] Shuichiro Ebata and Takashi Nakatsukasa. Octupole deformation in the nuclear chart based on the 3D Skyrme Hartree-Fock plus BCS model. *Physica Scr.*, 92(6):064005, may 2017.

[32] K. Nomura, D. Vretenar, T. Nikšić, and Bing-Nan Lu. Microscopic description of octupole shape-phase transitions in light actinide and rare-earth nuclei. *Phys. Rev. C*, 89:024312, Feb 2014.

[33] Zhong Xu and Zhi-Pan Li. Microscopic analysis of octupole shape transitions in neutron-rich actinides with relativistic energy density functional. *Chinese Phys. C*, 41(12):124107, 2017.

[34] S. E. Agbemava, A. V. Afanasjev, and P. Ring. Octupole deformation in the ground states of even-even nuclei: A global analysis within the covariant density functional theory. *Phys. Rev. C*, 93:044304, Apr 2016.

[35] S. E. Agbemava and A. V. Afanasjev. Octupole deformation in the ground states of even-even $Z \sim 96$, $N \sim 196$ actinides and superheavy nuclei. *Phys. Rev. C*, 96:024301, Aug 2017.

[36] S. Y. Xia, H. Tao, Y. Lu, Z. P. Li, T. Nikšić, and D. Vretenar. Spectroscopy of reflection-asymmetric nuclei with relativistic energy density functionals. *Phys. Rev. C*, 96:054303, Nov 2017.

[37] Mark Trodden. Electroweak baryogenesis. *Rev. Mod. Phys.*, 71:1463–1500, Oct 1999.

[38] T. E. Chupp, P. Fierlinger, M. J. Ramsey-Musolf, and J. T. Singh. Electric dipole moments of atoms, molecules, nuclei, and particles. *Rev. Mod. Phys.*, 91:015001, Jan 2019.

[39] W. C. Griffith, M. D. Swallows, T. H. Loftus, M. V. Romalis, B. R. Heckel, and E. N. Fortson. Improved limit on the permanent electric dipole moment of ^{199}Hg. *Phys. Rev. Lett.*, 102:101601, Mar 2009.

[40] L. I. Schiff. Measurability of nuclear electric dipole moments. *Phys. Rev.*, 132:2194–2200, Dec 1963.

[41] V. Spevak and N. Auerbach. Parity mixing and time reversal violation in nuclei with octupole deformations. *Physics Letters B*, 359(3):254 – 260, 1995.

[42] V. Spevak, N. Auerbach, and V. V. Flambaum. Enhanced t-odd, p-odd electromagnetic moments in reflection asymmetric nuclei. *Phys. Rev. C*, 56:1357–1369, Sep 1997.

[43] J. Engel, J. L. Friar, and A. C. Hayes. Nuclear octupole correlations and the enhancement of atomic time-reversal violation. *Phys. Rev. C*, 61:035502, Feb 2000.

[44] S. Athanassopoulos, E. Mavrommatis, K.A. Gernoth, and J.W. Clark. Nuclear mass systematics using neural networks. *Nuclear Physics A*, 743(4):222 – 235, 2004.

[45] R. Utama, J. Piekarewicz, and H. B. Prosper. Nuclear mass predictions for the crustal composition of neutron stars: A bayesian neural network approach. *Phys. Rev. C*, 93:014311, Jan 2016.

[46] R. Utama and J. Piekarewicz. Refining mass formulas for astrophysical applications: A bayesian neural network approach. *Phys. Rev. C*, 96:044308, Oct 2017.

[47] R. Utama and J. Piekarewicz. Validating neural-network refinements of nuclear mass models. *Phys. Rev. C*, 97:014306, Jan 2018.

[48] Hai Fei Zhang, Li Hao Wang, Jing Peng Yin, Peng Hui Chen, and Hong Fei Zhang. Performance of the levenberg–marquardt neural network approach in nuclear mass prediction. *Journal of Physics G: Nuclear and Particle Physics*, 44(4):045110, mar 2017.

[49] Z.M. Niu and H.Z. Liang. Nuclear mass predictions based on bayesian neural network approach with pairing and shell effects. *Physics Letters B*, 778:48 – 53, 2018.

[50] P. Hohenberg and W. Kohn. Inhomogeneous electron gas. *Phys. Rev.*, 136:B864–B871, Nov 1964.

[51] J.F. Berger, M. Girod, and D. Gogny. Microscopic analysis of collective dynamics in low energy fission. *Nuclear Physics A*, 428:23 – 36, 1984.

[52] F. Chappert, M. Girod, and S. Hilaire. Towards a new gogny force parameterization: Impact of the neutron matter equation of state. *Physics Letters B*, 668(5):420 – 424, 2008.

[53] S. Goriely, S. Hilaire, M. Girod, and S. Péru. First gogny-hartree-fock-bogoliubov nuclear mass model. *Phys. Rev. Lett.*, 102:242501, Jun 2009.

[54] G. A. Lalazissis, T. Nikšić, D. Vretenar, and P. Ring. New relativistic mean-field interaction with density-dependent meson-nucleon couplings. *Phys. Rev. C*, 71:024312, Feb 2005.

[55] G.A. Lalazissis, S. Karatzikos, R. Fossion, D. Pena Arteaga, A.V. Afanasjev, and P. Ring. The effective force NL3 revisited. *Phys. Lett. B*, 671(1):36 – 41, 2009.

[56] P. W. Zhao, Z. P. Li, J. M. Yao, and J. Meng. New parametrization for the nuclear covariant energy density functional with a point-coupling interaction. *Phys. Rev. C*, 82:054319, Nov 2010.

[57] T. Nikšić, D. Vretenar, and P. Ring. Relativistic nuclear energy density functionals: Adjusting parameters to binding energies. *Phys. Rev. C*, 78:034318, Sep 2008.

[58] C. Titin-Schnaider and Ph. Quentin. Coulomb exchange contribution in nuclear hartree-fock calculations. *Physics Letters B*, 49(5):397 – 400, 1974.

[59] T. H. R. Skyrme. Cvii. the nuclear surface. *The Philosophical Magazine: A Journal of Theoretical Experimental and Applied Physics*, 1(11):1043–1054, 1956.

[60] D. Gogny. "Proceedings of the international conference on nuclear self-consistent fields, triestel". page 333, 1975.

[61] D. Vretenar, A.V. Afanasjev, G.A. Lalazissis, and P. Ring. Relativistic Hartree-Bogoliubov theory: Static and dynamic aspects of exotic nuclear structure. *Phys. Rep.*, 409(3):101 – 259, 2005.

[62] W. Kohn and L. J. Sham. Self-consistent equations including exchange and correlation effects. *Phys. Rev.*, 140:A1133–A1138, Nov 1965.

[63] J. C. Slater. A simplification of the hartree-fock method. *Phys. Rev.*, 81:385–390, Feb 1951.

[64] J. C. Slater. The theory of complex spectra. *Phys. Rev.*, 34:1293–1322, Nov 1929.

[65] P Ring and P Schuck. *The Nuclear Many-Body Problem.*, 1980.

[66] J. Bardeen, L. N. Cooper, and J. R. Schrieffer. Theory of superconductivity. *Phys. Rev.*, 108:1175–1204, Dec 1957.

[67] E. Perlińska, S. G. Rohoziński, J. Dobaczewski, and W. Nazarewicz. Local density approximation for proton-neutron pairing correlations: Formalism. *Phys. Rev. C*, 69:014316, Jan 2004.

[68] Wikipedia: Table of spherical harmonics.

[69] M.V. Stoitsov, J. Dobaczewski, W. Nazarewicz, and P. Ring. Axially deformed solution of the Skyrme-Hartree-Fock-Bogolyubov equations using the transformed harmonic oscillator basis: The Program HFBTHO (v1.66p). *Comput. Phys. Commun.*, 167:43–63, 2005.

[70] R. Navarro Perez, N. Schunck, R.-D. Lasseri, C. Zhang, and J. Sarich. Axially deformed solution of the Skyrme-Hartree-Fock-Bogolyubov equations using the transformed harmonic oscillator basis (iii) HFBTHO (v3.00): A new version of the program. *Comput. Phys. Commun.*, 220:363 – 375, 2017.

[71] N. Schunck, J. Dobaczewski, W. Satuła, P. Bączyk, J. Dudek, Y. Gao, M. Konieczka, K. Sato, Y. Shi, X.B. Wang, and T.R. Werner. Solution of the Skyrme-Hartree-Fock-Bogolyubov equations in the cartesian deformed harmonic-oscillator basis. (viii) HFODD (v2.73y): A new version of the program. *Comput. Phys. Commun.*, 216:145 – 174, 2017.

[72] M. V. Stoitsov, J. Dobaczewski, R. Kirchner, W. Nazarewicz, and J. Terasaki. Variation after particle-number projection for the hartree-fock-bogoliubov method with the skyrme energy density functional. *Phys. Rev. C*, 76:014308, Jul 2007.

[73] Harry J. Lipkin. Collective motion in many-particle systems : Part 1. The violation of conservation laws. *Annals of Physics*, 9(2):272–291, February 1960.

[74] Yukihisa Nogami. Improved superconductivity approximation for the pairing interaction in nuclei. *Phys. Rev.*, 134:B313–B321, Apr 1964.

[75] H.C. Pradhan, Y. Nogami, and J. Law. Study of approximations in the nuclear pairing-force problem. *Nuclear Physics A*, 201(2):357 – 368, 1973.

[76] W. Younes and D. Gogny. Microscopic calculation of ^{240}Pu scission with a finite-range effective force. *Phys. Rev. C*, 80:054313, Nov 2009.

[77] M.V. Stoitsov, N. Schunck, M. Kortelainen, N. Michel, H. Nam, E. Olsen, J. Sarich, and S. Wild. Axially deformed solution of the skyrme-hartree-fock-bogoliubov equations using the transformed harmonic oscillator basis (ii) hfbtho v2.00d: A new version of the program. *Computer Physics Communications*, 184(6):1592 – 1604, 2013.

[78] N. Schunck, J. Dobaczewski, J. McDonnell, W. Satuła, J.A. Sheikh, A. Staszczak, M. Stoitsov, and P. Toivanen. Solution of the skyrme-hartree-fock-bogolyubov equations in the cartesian deformed harmonic-oscillator basis.: (vii) hfodd (v2.49t): A new version of the program. *Computer Physics Communications*, 183(1):166 – 192, 2012.

[79] P.-H. Heenen, P. Bonche, and H. Flocard. Microscopic study of superdeformation in 193hg. *Nuclear Physics A*, 588(2):490 – 500, 1995.

[80] J. Dobaczewski, W. Satuła, B.G. Carlsson, J. Engel, P. Olbratowski, P. Powałowski, M. Sadziak, J. Sarich, N. Schunck, A. Staszczak, M. Stoitsov, M. Zalewski, and H. Zduńczuk. Solution of the skyrme-hartree-fock-bogolyubov equations in the cartesian deformed harmonic-oscillator basis.: (vi) hfodd (v2.40h): A new version of the program. *Computer Physics Communications*, 180(11):2361 – 2391, 2009.

[81] N. Schunck, J. Dobaczewski, J. McDonnell, J. Moré, W. Nazarewicz, J. Sarich, and M. V. Stoitsov. One-quasiparticle states in the nuclear energy density functional theory. *Phys. Rev. C*, 81:024316, Feb 2010.

[82] Sara Perez-Martin and L. M. Robledo. Microscopic justification of the equal filling approximation. *Phys. Rev. C*, 78:014304, Jul 2008.

[83] Sara Perez-Martin and Luis M. Robledo. Generalized wick's theorem for multiquasi-particle overlaps as a limit of gaudin's theorem. *Phys. Rev. C*, 76:064314, Dec 2007.

[84] V.V. Flambaum, I.B. Khriplovich, and O.P. Sushkov. Limit on the constant of t-nonconserving nucleon-nucleon interaction. *Physics Letters B*, 162(4):213 – 216, 1985.

[85] V.V. Flambaum, I.B. Khriplovich, and O.P. Sushkov. On the p- and t-nonconserving nuclear moments. *Nuclear Physics A*, 449(4):750 – 760, 1986.

[86] V.A. Dzuba, V.V. Flambaum, and P.G. Silvestrov. Bounds on electric dipole moments and t-violating weak interactions of the nucleons. *Physics Letters B*, 154(2):93 – 95, 1985.

[87] V. Spevak, N. Auerbach, and V. V. Flambaum. Enhanced *t*-odd, *p*-odd electromagnetic moments in reflection asymmetric nuclei. *Phys. Rev. C*, 56:1357–1369, Sep 1997.

[88] V. V. Flambaum and J. S. M. Ginges. Nuclear schiff moment and time-invariance violation in atoms. *Phys. Rev. A*, 65:032113, Feb 2002.

[89] R.R. Chasman. Incipient octupole deformation and parity doublets in the odd mass light actinides. *Physics Letters B*, 96(1):7 – 10, 1980.

[90] R.G. Helmer, M.A. Lee, C.W. Reich, and I. Ahmad. Intrinsic reflection asymmetry in 225 Ra: Additional information from a study of the α-decay scheme of 229 Th. *Nucl. Phys. A*, 474:77–113, 1987.

[91] Jacek Dobaczewski, Jonathan Engel, Markus Kortelainen, and Pierre Becker. Correlating Schiff moments in the light actinides with octupole moments. *Phys. Rev. Lett.*, 121:232501, Dec 2018.

[92] Yuchen Cao, Sylvester E. Agbemava, Anatoli V. Afanasjev, Witold Nazarewicz, and Erik Olsen. Landscape of pear-shaped even-even nuclei. 4 2020.

[93] M. Kortelainen, T. Lesinski, J. Moré, W. Nazarewicz, J. Sarich, N. Schunck, M. V. Stoitsov, and S. Wild. Nuclear energy density optimization. *Phys. Rev. C*, 82:024313, Aug 2010.

[94] M. Kortelainen, J. McDonnell, W. Nazarewicz, P.-G. Reinhard, J. Sarich, N. Schunck, M. V. Stoitsov, and S. M. Wild. Nuclear energy density optimization: Large deformations. *Phys. Rev. C*, 85:024304, Feb 2012.

[95] M. Kortelainen, J. McDonnell, W. Nazarewicz, E. Olsen, P.-G. Reinhard, J. Sarich, N. Schunck, S. M. Wild, D. Davesne, J. Erler, and A. Pastore. Nuclear energy density optimization: Shell structure. *Phys. Rev. C*, 89:054314, May 2014.

[96] E Chabanat, P Bonche, P Haensel, J Meyer, and R Schaeffer. New Skyrme effective forces for supernovae and neutron rich nuclei. *Physica Scr.*, 1995(T56):231, 1995.

[97] P. Klüpfel, P.-G. Reinhard, T. J. Bürvenich, and J. A. Maruhn. Variations on a theme by Skyrme: A systematic study of adjustments of model parameters. *Phys. Rev. C*, 79(3):034310, Mar 2009.

[98] Jochen Erler, Noah Birge, Markus Kortelainen, Witold Nazarewicz, Erik Olsen, Alexander M. Perhac, and Mario Stoitsov. The limits of the nuclear landscape. *Nature*, 486(7404):509–512, 2012.

[99] Meng Wang, G. Audi, F. G. Kondev, W.J. Huang, S. Naimi, and Xing Xu. The AME2016 atomic mass evaluation (II). tables, graphs and references. *Chin. Phys. C*, 41(3):030003, mar 2017.

[100] A. V. Afanasjev and S. Frauendorf. Central depression in nuclear density and its consequences for the shell structure of superheavy nuclei. *Phys. Rev. C*, 71:024308, Feb 2005.

[101] B. Schuetrumpf, W. Nazarewicz, and P.-G. Reinhard. Central depression in nucleonic densities: Trend analysis in the nuclear density functional theory approach. *Phys. Rev. C*, 96:024306, Aug 2017.

[102] Witold Nazarewicz. The limits of nuclear mass and charge. *Nat. Phys.*, 14(6):537–541, Jun 2018.

[103] A. V. Afanasjev, S. E. Agbemava, and A. Gyawali. Hyperheavy nuclei: Existence and stability. *Phys. Lett. B*, 782:533, 2018.

[104] S. A. Giuliani, Z. Matheson, W. Nazarewicz, E. Olsen, P.-G. Reinhard, J. Sadhukhan, B. Schuetrumpf, N. Schunck, and P. Schwerdtfeger. Colloquium: Superheavy elements: Oganesson and beyond. *Rev. Mod. Phys.*, 91:011001, Jan 2019.

[105] S. E. Agbemava, A. V. Afanasjev, A. Taninah, and A. Gyawali. Extension of the nuclear landscape to hyperheavy nuclei. *Phys. Rev. C*, 99:034316, 2019.

[106] Institute for cyber-enabled research at michigan state university. `https://icer.msu.edu/`.

[107] MassExplorer. `http://massexplorer.frib.msu.edu`.

[108] Léo Neufcourt, Yuchen Cao, Samuel A. Giuliani, Witold Nazarewicz, Erik Olsen, and Oleg B. Tarasov. Quantified limits of the nuclear landscape. *Phys. Rev. C*, 101:044307, Apr 2020.

[109] Léo Neufcourt, Yuchen Cao, Samuel Giuliani, Witold Nazarewicz, Erik Olsen, and Oleg B. Tarasov. Beyond the proton drip line: Bayesian analysis of proton-emitting nuclei. *Phys. Rev. C*, 101:014319, Jan 2020.

[110] National Nuclear Data Center. http://www.nndc.bnl.gov.

[111] L. P. Gaffney, P. A. Butler, M. Scheck, A. B. Hayes, F. Wenander, M. Albers, B. Bastin, C. Bauer, A. Blazhev, S. Bönig, N. Bree, J. Cederkäll, T. Chupp, D. Cline, T. E. Cocolios, T. Davinson, H. de Witte, J. Diriken, T. Grahn, A. Herzan, M. Huyse, D. G. Jenkins, D. T. Joss, N. Kesteloot, J. Konki, M. Kowalczyk, Th. Kröll, E. Kwan, R. Lutter, K. Moschner, P. Napiorkowski, J. Pakarinen, M. Pfeiffer, D. Radeck, P. Reiter, K. Reynders, S. V. Rigby, L. M. Robledo, M. Rudigier, S. Sambi, M. Seidlitz, B. Siebeck, T. Stora, P. Thoele, P. van Duppen, M. J. Vermeulen, M. von Schmid, D. Voulot, N. Warr, K. Wimmer, K. Wrzosek-Lipska, C. Y. Wu, and M. Zielinska. Studies of pear-shaped nuclei using accelerated radioactive beams. *Nature*, 497(7448):199–204, May 2013.

[112] K. Gulda, H. Mach, A.J. Aas, M.J.G. Borge, D.G. Burke, B. Fogelberg, H. Gietz, I.S. Grant, E. Hagebo, P. Hill, P. Hoff, N. Kaffrell, W. Kurcewicz, A. Lindroth, G. Løvhøiden, T. Martinez, S. Mattsson, R.A. Naumann, K. Nybø, G. Nyman, B. Rubio, M. Sanchez-Vega, J.L. Tain, R.B.E. Taylor, O. Tengblad, and T.F. Thorsteinsen. Quadrupole deformed and octupole collective bands in 228Ra. *Nucl. Phys. A*, 636(1):28 – 46, 1998.

[113] Sukhjeet Singh, A.K. Jain, and Jagdish K. Tuli. Nuclear data sheets for $A = 222$. *Nucl. Data Sheets*, 112(11):2851 – 2886, 2011.

[114] J.L. Egido and L.M. Robledo. Parity-projected calculations on octupole deformed nuclei. *Nucl. Phys. A*, 524(1):65 – 87, 1991.

[115] L. M. Robledo. Enhancement of octupole strength in near spherical nuclei. *Eur. Phys. J. A*, 52(9):300, 2016.

[116] J. M. Yao, E. F. Zhou, and Z. P. Li. Beyond relativistic mean-field approach for nuclear octupole excitations. *Phys. Rev. C*, 92:041304, Oct 2015.

[117] J. M. Yao and J. Engel. Octupole correlations in low-lying states of ^{150}Nd and ^{150}Sm and their impact on neutrinoless double-β decay. *Phys. Rev. C*, 94:014306, Jul 2016.

[118] J. F. C. Cocks, P. A. Butler, K. J. Cann, P. T. Greenlees, G. D. Jones, S. Asztalos, P. Bhattacharyya, R. Broda, R. M. Clark, M. A. Deleplanque, R. M. Diamond, P. Fallon, B. Fornal, P. M. Jones, R. Julin, T. Lauritsen, I. Y. Lee, A. O. Macchiavelli,

R. W. MacLeod, J. F. Smith, F. S. Stephens, and C. T. Zhang. Observation of octupole structures in radon and radium isotopes and their contrasting behavior at high spin. *Phys. Rev. Lett.*, 78:2920–2923, Apr 1997.

[119] J.F.C. Cocks, D. Hawcroft, N. Amzal, P.A. Butler, K.J. Cann, P.T. Greenlees, G.D. Jones, S. Asztalos, R.M. Clark, M.A. Deleplanque, R.M. Diamond, P. Fallon, I.Y. Lee, A.O. Macchiavelli, R.W. MacLeod, F.S. Stephens, P. Jones, R. Julin, R. Broda, B. Fornal, J.F. Smith, T. Lauritsen, P. Bhattacharyya, and C.T. Zhang. Spectroscopy of Rn, Ra and Th isotopes using multi-nucleon transfer reactions. *Nucl. Phys. A*, 645(1):61 – 91, 1999.

[120] P. A. Butler, L. P. Gaffney, P. Spagnoletti, J. Konki, M. Scheck, J. F. Smith, K. Abrahams, M. Bowry, J. Cederkäll, T. Chupp, G. de Angelis, H. De Witte, P. E. Garrett, A. Goldkuhle, C. Henrich, A. Illana, K. Johnston, D. T. Joss, J. M. Keatings, N. A. Kelly, M. Komorowska, T. Kröll, M. Lozano, B. S. Nara Singh, D. O'Donnell, J. Ojala, R. D. Page, L. G. Pedersen, C. Raison, P. Reiter, J. A. Rodriguez, D. Rosiak, S. Rothe, T. M. Shneidman, B. Siebeck, M. Seidlitz, J. Sinclair, M. Stryjczyk, P. Van Duppen, S. Vinals, V. Virtanen, N. Warr, K. Wrzosek-Lipska, and M. Zielinska. The observation of vibrating pear-shapes in radon nuclei. *Nat. Commun.*, 10:2473, 2019.

[121] P. A. Butler, L. P. Gaffney, P. Spagnoletti, K. Abrahams, M. Bowry, J. Cederkäll, G. de Angelis, H. De Witte, P. E. Garrett, A. Goldkuhle, C. Henrich, A. Illana, K. Johnston, D. T. Joss, J. M. Keatings, N. A. Kelly, M. Komorowska, J. Konki, T. Kröll, M. Lozano, B. S. Nara Singh, D. O'Donnell, J. Ojala, R. D. Page, L. G. Pedersen, C. Raison, P. Reiter, J. A. Rodriguez, D. Rosiak, S. Rothe, M. Scheck, M. Seidlitz, T. M. Shneidman, B. Siebeck, J. Sinclair, J. F. Smith, M. Stryjczyk, P. Van Duppen, S. Vinals, V. Virtanen, N. Warr, K. Wrzosek-Lipska, and M. Zielińska. Evolution of octupole deformation in radium nuclei from coulomb excitation of radioactive ^{222}Ra and ^{228}Ra beams. *Phys. Rev. Lett.*, 124:042503, Jan 2020.

[122] T. E. Chupp, P. Fierlinger, M. J. Ramsey-Musolf, and J. T. Singh. Electric dipole moments of atoms, molecules, nuclei, and particles. *Rev. Mod. Phys.*, 91:015001, Jan 2019.

[123] J. Engel, M. Bender, J. Dobaczewski, J. H. de Jesus, and P. Olbratowski. Time-reversal violating Schiff moment of ^{225}Ra. *Phys. Rev. C*, 68:025501, Aug 2003.

[124] H.J. Wollersheim, H. Emling, H. Grein, R. Kulessa, R.S. Simon, C. Fleischmann, J. [de Boer], E. Hauber, C. Lauterbach, C. Schandera, P.A. Butler, and T. Czosnyka. Coulomb excitation of 226ra. *Nuclear Physics A*, 556(2):261 – 280, 1993.

[125] P. A. Butler. (private communication).

[126] B. Ackermann, H. Baltzer, C. Ensel, K. Freitag, V. Grafen, C. Günther, P. Herzog, J. Manns, M. Marten-Tölle, U. Müller, J. Prinz, I. Romanski, R. Tölle, J. deBoer, N. Gollwitzer, and H.J. Maier. Collective E1 transitions in even-A Ra, Th, and U nuclei. *Nucl. Phys. A*, 559(1):61 – 82, 1993.

[127] J. F. Smith, J. F. C. Cocks, N. Schulz, M. Aïche, M. Bentaleb, P. A. Butler, F. Hannachi, G. D. Jones, P. M. Jones, R. Julin, S. Juutinen, R. Kulessa, E. Lubkiewicz, A. Płochocki, F. Riess, E. Ruchowska, A. Savelius, J. C. Sens, J. Simpson, and E. Wolf. Contrasting behavior in octupole structures observed at high spin in ^{220}Ra and ^{222}Th. *Phys. Rev. Lett.*, 75:1050–1053, Aug 1995.

[128] P. T. Greenlees, N. Amzal, P. A. Butler, K. J. Cann, D. Hawcroft, G. D. Jones, R. D. Page, J. F. C. Cocks, A. Andreev, T. Enqvist, K. Helariutta, P. M. Jones, R. Julin, S. Juutinen, H. Kankaanpaeae, H. Kettunen, P. Kuusiniemi, M. Leino, M. Muikku, A. Savelius, W. H. Trzaska, J. Uusitalo, P. Fallon, B. Gall, F. Hoellinger, M. Guttormsen, S. Messelt, A. Schiller, S. Siem, and T. Tveter. First observation of excited states in ^{226}U. *J. Phys. G*, 24(10):L63, 1998.

[129] K. Nishio, H. Ikezoe, S. Mitsuoka, K. Satou, and C. J. Lin. Half-life of ^{228}Pu and α decay of ^{228}Np. *Phys. Rev. C*, 68:064305, Dec 2003.

[130] S. A. Giuliani, G. Martínez-Pinedo, and L. M. Robledo. Fission properties of superheavy nuclei for r-process calculations. *Phys. Rev. C*, 97:034323, 2018.

[131] S. A. Giuliani, G. Martínez-Pinedo, M. R. Wu, and L. M. Robledo. Fission and the r-process nucleosynthesis of translead nuclei. 2019.

[132] W. R. Phillips, I. Ahmad, H. Emling, R. Holzmann, R. V. F. Janssens, T. L. Khoo, and M. W. Drigert. Octupole deformation in neutron-rich barium isotopes. *Phys. Rev. Lett.*, 57:3257–3260, Dec 1986.

[133] H. Mach, W. Nazarewicz, D. Kusnezov, M. Moszyński, B. Fogelberg, M. Hellström, L. Spanier, R. L. Gill, R. F. Casten, and A. Wolf. Influence of shell effects and stable octupole deformation on the E1 and E2 transition rates in the heavy-Ba region. *Phys. Rev. C*, 41:R2469–R2473, Jun 1990.

[134] S.J. Zhu, Q.H. Lu, J.H. Hamilton, A.V. Ramayya, L.K. Peker, M.G. Wang, W.C. Ma, B.R.S. Babu, T.N. Ginter, J. Kormicki, D. Shi, J.K. Deng, W. Nazarewicz, J.O. Rasmussen, M.A. Stoyer, S.Y. Chu, K.E. Gregorich, M.F. Mohar, S. Asztalos, S.G. Prussin, J.D. Cole, R. Aryaeinejad, Y.K. Dardenne, M. Drigert, K.J. Moody, R.W. Loughed, J.F. Wild, N.R. Johnson, I.Y. Lee, F.K. McGowan, G.M. Ter-Akopian, and

Yu.Ts. Oganessian. Octupole deformation in ^{142,143}Ba and ^{144}Ce: New band structures in neutron-rich Ba-isotopes. *Phys. Lett. B*, 357(3):273 – 280, 1995.

[135] W. Urban, M.A. Jones, J.L. Durell, M. Leddy, W.R. Phillips, A.G. Smith, B.J. Varley, I. Ahmad, L.R. Morss, M. Bentaleb, E. Lubkiewicz, and N. Schulz. Octupole correlations in neutron-rich, even-even barium isotopes. *Nucl. Phys. A*, 613(1):107 – 131, 1997.

[136] B. Bucher, S. Zhu, C. Y. Wu, R. V. F. Janssens, D. Cline, A. B. Hayes, M. Albers, A. D. Ayangeakaa, P. A. Butler, C. M. Campbell, M. P. Carpenter, C. J. Chiara, J. A. Clark, H. L. Crawford, M. Cromaz, H. M. David, C. Dickerson, E. T. Gregor, J. Harker, C. R. Hoffman, B. P. Kay, F. G. Kondev, A. Korichi, T. Lauritsen, A. O. Macchiavelli, R. C. Pardo, A. Richard, M. A. Riley, G. Savard, M. Scheck, D. Seweryniak, M. K. Smith, R. Vondrasek, and A. Wiens. Direct evidence of octupole deformation in neutron-rich ^{144}Ba. *Phys. Rev. Lett.*, 116:112503, Mar 2016.

[137] B. Bucher, S. Zhu, C. Y. Wu, R. V. F. Janssens, R. N. Bernard, L. M. Robledo, T. R. Rodríguez, D. Cline, A. B. Hayes, A. D. Ayangeakaa, M. Q. Buckner, C. M. Campbell, M. P. Carpenter, J. A. Clark, H. L. Crawford, H. M. David, C. Dickerson, J. Harker, C. R. Hoffman, B. P. Kay, F. G. Kondev, T. Lauritsen, A. O. Macchiavelli, R. C. Pardo, G. Savard, D. Seweryniak, and R. Vondrasek. Direct evidence for octupole deformation in ^{146}Ba and the origin of large E1 moment variations in reflection-asymmetric nuclei. *Phys. Rev. Lett.*, 118:152504, Apr 2017.

[138] W.R. Phillips, R.V.F. Janssens, I. Ahmad, H. Emling, R. Holzmann, T.L. Khoo, and M.W. Drigert. Octupole correlation effects near $Z = 56, N = 88$. *Phys. Lett. B*, 212(4):402 – 406, 1988.

[139] Y. J. Chen, S. J. Zhu, J. H. Hamilton, A. V. Ramayya, J. K. Hwang, M. Sakhaee, Y. X. Luo, J. O. Rasmussen, K. Li, I. Y. Lee, X. L. Che, H. B. Ding, and M. L. Li. Search for octupole correlations in neutron-rich ^{148}Ce nucleus. *Phys. Rev. C*, 73:054316, May 2006.

[140] S. J. Zhu, M. Sakhaee, J. H. Hamilton, A. V. Ramayya, N. T. Brewer, J. K. Hwang, S. H. Liu, E. Y. Yeoh, Z. G. Xiao, Q. Xu, Z. Zhang, Y. X. Luo, J. O. Rasmussen, I. Y. Lee, K. Li, and W. C. Ma. Observation of new levels and proposed octupole correlations in neutron-rich ^{150}Ce. *Phys. Rev. C*, 85:014330, Jan 2012.

[141] W. Urban, R.M. Lieder, J.C. Bacelar, P.P. Singh, D. Alber, D. Balabanski, W. Gast, H. Grawe, G. Hebbinghaus, J.R. Jongman, T. Morek, R.F. Noorman, T. Rzaca-Urban, H. Schnare, M. Thoms, O. Zell, and W. Nazarewicz. High-spin octupole correlations in the $N = 86$, ^{146}Nd and ^{148}Sm nuclei. *Phys. Lett. B*, 258(3):293 – 298, 1991.

[142] V.E Iacob, W Urban, J.C Bacelar, J Jongman, J Nyberg, G Sletten, and L Trache. Reflection asymmetric states in ^{146}Nd. *Nucl. Phys. A*, 596(1):155 – 170, 1996.

[143] R. Ibbotson, C. A. White, T. Czosnyka, P. A. Butler, N. Clarkson, D. Cline, R. A. Cunningham, M. Devlin, K. G. Helmer, T. H. Hoare, J. R. Hughes, G. D. Jones, A. E. Kavka, B. Kotlinski, R. J. Poynter, P. Regan, E. G. Vogt, R. Wadsworth, D. L. Watson, and C. Y. Wu. Octupole collectivity in the ground band of ^{148}Nd. *Phys. Rev. Lett.*, 71:1990–1993, Sep 1993.

[144] R.W. Ibbotson, C.A. White, T. Czosnyka, P.A. Butler, N. Clarkson, D. Cline, R.A. Cunningham, M. Devlin, K.G. Helmer, T.H. Hoare, J.R. Hughes, G.D. Jones, A.E. Kavka, B. Kotlinski, R.J. Poynter, P.H. Regan, E.G. Vogt, R. Wadsworth, D.L. Watson, and C.Y. Wu. Quadrupole and octupole collectivity in ^{148}Nd. *Nucl. Phys. A*, 619(1):213 – 240, 1997.

[145] H. Friedrichs, B. Schlitt, J. Margraf, S. Lindenstruth, C. Wesselborg, R. D. Heil, H. H. Pitz, U. Kneissl, P. von Brentano, R. D. Herzberg, A. Zilges, D. Häger, G. Müller, and M. Schumacher. Evidence for enhanced electric dipole excitations in deformed rare earth nuclei near 2.5 MeV. *Phys. Rev. C*, 45:R892–R895, Mar 1992.

[146] S. P. Bvumbi, J. F. Sharpey-Schafer, P. M. Jones, S. M. Mullins, B. M. Nyakó, K. Juhász, R. A. Bark, L. Bianco, D. M. Cullen, D. Curien, P. E. Garrett, P. T. Greenlees, J. Hirvonen, U. Jakobsson, J. Kau, F. Komati, R. Julin, S. Juutinen, S. Ketelhut, A. Korichi, E. A. Lawrie, J. J. Lawrie, M. Leino, T. E. Madiba, S. N. T. Majola, P. Maine, A. Minkova, N. J. Ncapayi, P. Nieminen, P. Peura, P. Rahkila, L. L. Riedinger, P. Ruotsalainen, J. Saren, C. Scholey, J. Sorri, S. Stolze, J. Timar, J. Uusitalo, and P. A. Vymers. Octupole correlations in the structure of 0_2^+ bands in the $N = 88$ nuclei ^{150}Sm and ^{152}Gd. *Phys. Rev. C*, 87:044333, Apr 2013.

[147] V. V. Flambaum and H. Feldmeier. Enhanced nuclear Schiff moment in stable and metastable nuclei. *Phys. Rev. C*, 101:015502, Jan 2020.

[148] J. Skalski. Octupolly deformed nuclei near ^{112}Ba. *Phys. Lett. B*, 238(1):6 – 10, 1990.

[149] P.-H. Heenen, J. Skalski, P. Bonche, and H. Flocard. Octupole excitations in light xenon and barium nuclei. *Phys. Rev. C*, 50:802–806, Aug 1994.

[150] J.F Smith, C.J Chiara, D.B Fossan, D.R LaFosse, G.J Lane, J.M Sears, K Starosta, M Devlin, F Lerma, D.G Sarantites, S.J Freeman, M.J Leddy, J.L Durell, A.J Boston, E.S Paul, A.T Semple, I.Y Lee, A.O Macchiavelli, and P.H Heenen. Excited states and deformation of ^{112}Xe. *Phys. Lett. B*, 523(1):13 – 21, 2001.

[151] S. L. Rugari, R. H. France, B. J. Lund, Z. Zhao, M. Gai, P. A. Butler, V. A. Holliday, A. N. James, G. D. Jones, R. J. Poynter, R. J. Tanner, K. L. Ying, and J. Simpson. Broken reflection symmetry in ^{114}Xe. *Phys. Rev. C*, 48:2078–2081, Oct 1993.

[152] L. Capponi, J. F. Smith, P. Ruotsalainen, C. Scholey, P. Rahkila, K. Auranen, L. Bianco, A. J. Boston, H. C. Boston, D. M. Cullen, X. Derkx, M. C. Drummond, T. Grahn, P. T. Greenlees, L. Grocutt, B. Hadinia, U. Jakobsson, D. T. Joss, R. Julin, S. Juutinen, M. Labiche, M. Leino, K. G. Leach, C. McPeake, K. F. Mulholland, P. Nieminen, D. O'Donnell, E. S. Paul, P. Peura, M. Sandzelius, J. Sarén, B. Saygi, J. Sorri, S. Stolze, A. Thornthwaite, M. J. Taylor, and J. Uusitalo. Direct observation of the ^{114}Ba $\rightarrow$ ^{110}Xe $\rightarrow$ ^{106}Te $\rightarrow$ ^{102}Sn triple α-decay chain using position and time correlations. *Phys. Rev. C*, 94:024314, Aug 2016.

[153] J. Lippuner and L. F. Roberts. r-process lanthanide production and heating rates in kilonovae. *APJ*, 815(2):82, 2015.

[154] W. J. Vermeer, M. K. Khan, A. S. Mowbray, J. B. Fitzgerald, J. A. Cizewski, B. J. Varley, J. L. Durell, and W. R. Phillips. Octupole correlation effects in ^{151}Pm. *Phys. Rev. C*, 42:R1183–R1186, Oct 1990.

[155] W. Urban, J.C. Bacelar, W. Gast, G. Hebbinghaus, A. Krämer-Flecken, R.M. Lieder, T. Morek, and T. Rązca-Urban. High-spin parity doublets in the nucleus 151pm. *Physics Letters B*, 247(2):238 – 241, 1990.

[156] C. J. Pearson, W. R. Phillips, J. L. Durell, B. J. Varley, W. J. Vermeer, W. Urban, and M. K. Khan. Opposite-parity bands in ^{153}Eu. *Phys. Rev. C*, 49:R1239–R1242, Mar 1994.

[157] V. Spevak, N. Auerbach, and V. V. Flambaum. Enhanced t-odd, p-odd electromagnetic moments in reflection asymmetric nuclei. *Phys. Rev. C*, 56:1357–1369, Sep 1997.

[158] Léo Neufcourt, Yuchen Cao, Witold Nazarewicz, and Frederi Viens. Bayesian approach to model-based extrapolation of nuclear observables. *Phys. Rev. C*, 98:034318, Sep 2018.

[159] Léo Neufcourt, Yuchen Cao, Witold Nazarewicz, Erik Olsen, and Frederi Viens. Neutron drip line in the ca region from bayesian model averaging. *Phys. Rev. Lett.*, 122:062502, Feb 2019.

[160] W.J. Huang, G. Audi, Meng Wang, F. G. Kondev, S. Naimi, and Xing Xu. The AME2016 atomic mass evaluation (i). evaluation of input data and adjustment procedures. *Chinese Physics C*, 41(3):030002, mar 2017.

[161] Tuncay Bayram, Serkan Akkoyun, and S. Okan Kara. A study on ground-state energies of nuclei by using neural networks. *Annals of Nuclear Energy*, 63:172 – 175, 2014.

[162] Tuncay Bayram and Serkan Akkoyun. An approach to adjustment of relativistic mean field model parameters. 146:12033, September 2017.

[163] Cenxi Yuan. Uncertainty decomposition method and its application to the liquid drop model. *Phys. Rev. C*, 93:034310, Mar 2016.

[164] G. F. Bertsch and Derek Bingham. Estimating parameter uncertainty in binding-energy models by the frequency-domain bootstrap. *Phys. Rev. Lett.*, 119:252501, Dec 2017.

[165] Hai Fei Zhang, Li Hao Wang, Jing Peng Yin, Peng Hui Chen, and Hong Fei Zhang. Performance of the levenberg–marquardt neural network approach in nuclear mass prediction. *Journal of Physics G: Nuclear and Particle Physics*, 44(4):045110, mar 2017.

[166] A.H. Wapstra, G. Audi, and C. Thibault. The AME2003 atomic mass evaluation: (i). evaluation of input data, adjustment procedures. *Nuclear Physics A*, 729(1):129 – 336, 2003. The 2003 NUBASE and Atomic Mass Evaluations.

[167] G. Audi, A.H. Wapstra, and C. Thibault. The AME2003 atomic mass evaluation: (ii). tables, graphs and references. *Nuclear Physics A*, 729(1):337 – 676, 2003. The 2003 NUBASE and Atomic Mass Evaluations.

[168] M. Vilen, J. M. Kelly, A. Kankainen, M. Brodeur, A. Aprahamian, L. Canete, T. Eronen, A. Jokinen, T. Kuta, I. D. Moore, M. R. Mumpower, D. A. Nesterenko, H. Penttilä, I. Pohjalainen, W. S. Porter, S. Rinta-Antila, R. Surman, A. Voss, and J. Äystö. Precision mass measurements on neutron-rich rare-earth isotopes at JYFLTRAP: Reduced neutron pairing and implications for *r*-process calculations. *Phys. Rev. Lett.*, 120:262701, Jun 2018.

[169] P. Möller, A.J. Sierk, T. Ichikawa, and H. Sagawa. Nuclear ground-state masses and deformations: Frdm(2012). *Atomic Data and Nuclear Data Tables*, 109-110:1 – 204, 2016.

[170] S. Goriely, N. Chamel, and J. M. Pearson. Further explorations of skyrme-hartree-fock-bogoliubov mass formulas. xiii. the 2012 atomic mass evaluation and the symmetry coefficient. *Phys. Rev. C*, 88:024308, Aug 2013.

[171] J. Bartel, P. Quentin, M. Brack, C. Guet, and H.-B. Hakansson. Towards a better parametrisation of Skyrme-like effective forces: A critical study of the SkM force. *Nucl. Phys. A*, 386(1):79 – 100, 1982.

[172] J. Dobaczewski, H. Flocard, and J. Treiner. Hartree-Fock-Bogolyubov description of nuclei near the neutron-drip line. *Nucl. Phys. A*, 422(1):103 – 139, 1984.

[173] X. Roca-Maza, X. Viñas, M. Centelles, P. Ring, and P. Schuck. Relativistic mean-field interaction with density-dependent meson-nucleon vertices based on microscopical calculations. *Phys. Rev. C*, 84:054309, Nov 2011.

[174] W. R. Gilks, S. Richardson, and D. Spiegelhalter. Markov chain monte carlo in practice. *Chapman & Hall/CRC Interdisciplinary Statistics (Chapman and Hall, London, 1995)*.

[175] D. MacKay. Information theory, inference, and learning algorithms. *(Cambridge University Press, Cambridge, 2005)*.

[176] R Utama, Wei-Chia Chen, and J Piekarewicz. Nuclear charge radii: density functional theory meets bayesian neural networks. *Journal of Physics G: Nuclear and Particle Physics*, 43(11):114002, oct 2016.

[177] R. F. Casten, D. S. Brenner, and P. E. Haustein. Valence p-n interactions and the development of collectivity in heavy nuclei. *Phys. Rev. Lett.*, 58:658–661, Feb 1987.

[178] E. Leistenschneider, M. P. Reiter, S. Ayet San Andrés, B. Kootte, J. D. Holt, P. Navrátil, C. Babcock, C. Barbieri, B. R. Barquest, J. Bergmann, J. Bollig, T. Brunner, E. Dunling, A. Finlay, H. Geissel, L. Graham, F. Greiner, H. Hergert, C. Hornung, C. Jesch, R. Klawitter, Y. Lan, D. Lascar, K. G. Leach, W. Lippert, J. E. McKay, S. F. Paul, A. Schwenk, D. Short, J. Simonis, V. Somà, R. Steinbrügge, S. R. Stroberg, R. Thompson, M. E. Wieser, C. Will, M. Yavor, C. Andreoiu, T. Dickel, I. Dillmann, G. Gwinner, W. R. Plaß, C. Scheidenberger, A. A. Kwiatkowski, and J. Dilling. Dawning of the $n = 32$ shell closure seen through precision mass measurements of neutron-rich titanium isotopes. *Phys. Rev. Lett.*, 120:062503, Feb 2018.

[179] S. Michimasa, M. Kobayashi, Y. Kiyokawa, S. Ota, D. S. Ahn, H. Baba, G. P. A. Berg, M. Dozono, N. Fukuda, T. Furuno, E. Ideguchi, N. Inabe, T. Kawabata, S. Kawase, K. Kisamori, K. Kobayashi, T. Kubo, Y. Kubota, C. S. Lee, M. Matsushita, H. Miya, A. Mizukami, H. Nagakura, D. Nishimura, H. Oikawa, H. Sakai, Y. Shimizu, A. Stolz, H. Suzuki, M. Takaki, H. Takeda, S. Takeuchi, H. Tokieda, T. Uesaka, K. Yako, Y. Yamaguchi, Y. Yanagisawa, R. Yokoyama, K. Yoshida, and S. Shimoura. Magic nature of neutrons in ^{54}Ca: First mass measurements of $^{55--57}$Ca. *Phys. Rev. Lett.*, 121:022506, Jul 2018.

[180] O. B. Tarasov, D. S. Ahn, D. Bazin, N. Fukuda, A. Gade, M. Hausmann, N. Inabe, S. Ishikawa, N. Iwasa, K. Kawata, T. Komatsubara, T. Kubo, K. Kusaka, D. J. Morrissey, M. Ohtake, H. Otsu, M. Portillo, T. Sakakibara, H. Sakurai, H. Sato, B. M. Sherrill, Y. Shimizu, A. Stolz, T. Sumikama, H. Suzuki, H. Takeda, M. Thoennessen, H. Ueno, Y. Yanagisawa, and K. Yoshida. Discovery of ^{60}Ca and implications for the stability of ^{70}Ca. *Phys. Rev. Lett.*, 121:022501, Jul 2018.

[181] O. B. Tarasov, D. J. Morrissey, A. M. Amthor, T. Baumann, D. Bazin, A. Gade, T. N. Ginter, M. Hausmann, N. Inabe, T. Kubo, A. Nettleton, J. Pereira, M. Portillo, B. M. Sherrill, A. Stolz, and M. Thoennessen. Evidence for a change in the nuclear mass surface with the discovery of the most neutron-rich nuclei with $17 \leq z \leq 25$. *Phys. Rev. Lett.*, 102:142501, Apr 2009.

[182] I. Mukha, K. Sümmerer, L. Acosta, M. A. G. Alvarez, E. Casarejos, A. Chatillon, D. Cortina-Gil, J. Espino, A. Fomichev, J. E. García-Ramos, H. Geissel, J. Gómez-Camacho, L. Grigorenko, J. Hoffmann, O. Kiselev, A. Korsheninnikov, N. Kurz, Yu. Litvinov, I. Martel, C. Nociforo, W. Ott, M. Pfutzner, C. Rodríguez-Tajes, E. Roeckl, M. Stanoiu, H. Weick, and P. J. Woods. Observation of two-proton radioactivity of ^{19}Mg by tracking the decay products. *Phys. Rev. Lett.*, 99:182501, Oct 2007.

[183] J. Giovinazzo, B. Blank, M. Chartier, S. Czajkowski, A. Fleury, M. J. Lopez Jimenez, M. S. Pravikoff, J.-C. Thomas, F. de Oliveira Santos, M. Lewitowicz, V. Maslov, M. Stanoiu, R. Grzywacz, M. Pfützner, C. Borcea, and B. A. Brown. Two-proton radioactivity of ^{45}Fe. *Phys. Rev. Lett.*, 89:102501, Aug 2002.

[184] M. Pfützner, E. Badura, and C. et al. Bingham. First evidence for the two-proton decay of ^{45}Fe. *Eur. Phys. J. A*, 14:279, 2002.

[185] C. Dossat, A. Bey, B. Blank, G. Canchel, A. Fleury, J. Giovinazzo, I. Matea, F. de Oliveira Santos, G. Georgiev, S. Grévy, I. Stefan, J. C. Thomas, N. Adimi, C. Borcea, D. Cortina Gil, M. Caamano, M. Stanoiu, F. Aksouh, B. A. Brown, and L. V. Grigorenko. Two-proton radioactivity studies with ^{45}Fe and ^{48}Ni. *Phys. Rev. C*, 72:054315, Nov 2005.

[186] C. Dossat, N. Adimi, F. Aksouh, F. Becker, A. Bey, B. Blank, C. Borcea, R. Borcea, A. Boston, M. Caamano, G. Canchel, M. Chartier, D. Cortina, S. Czajkowski, G. [de France], F. [de Oliveira Santos], A. Fleury, G. Georgiev, J. Giovinazzo, S. Grévy, R. Grzywacz, M. Hellström, M. Honma, Z. Janas, D. Karamanis, J. Kurcewicz, M. Lewitowicz, M.J. [López Jiménez], C. Mazzocchi, I. Matea, V. Maslov, P. Mayet, C. Moore, M. Pfützner, M.S. Pravikoff, M. Stanoiu, I. Stefan, and J.C. Thomas. The decay of proton-rich nuclei in the mass a=36-56 region. *Nuclear Physics A*, 792(1):18 – 86, 2007.

[187] M. Pomorski, M. Pfützner, W. Dominik, R. Grzywacz, T. Baumann, J. S. Berryman, H. Czyrkowski, R. Dąbrowski, T. Ginter, J. Johnson, G. Kamiński, A. Kuźniak, N. Larson, S. N. Liddick, M. Madurga, C. Mazzocchi, S. Mianowski, K. Miernik, D. Miller, S. Paulauskas, J. Pereira, K. P. Rykaczewski, A. Stolz, and S. Suchyta. First observation of two-proton radioactivity in ^{48}Ni. *Phys. Rev. C*, 83:061303, Jun 2011.

[188] M. Pomorski, M. Pfützner, W. Dominik, R. Grzywacz, A. Stolz, T. Baumann, J. S. Berryman, H. Czyrkowski, R. Dąbrowski, A. Fijałkowska, T. Ginter, J. Johnson, G. Kamiński, N. Larson, S. N. Liddick, M. Madurga, C. Mazzocchi, S. Mianowski, K. Miernik, D. Miller, S. Paulauskas, J. Pereira, K. P. Rykaczewski, and S. Suchyta. Proton spectroscopy of ^{48}Ni,^{46}Fe, and ^{44}Cr. *Phys. Rev. C*, 90:014311, Jul 2014.

[189] B. Blank, A. Bey, G. Canchel, C. Dossat, A. Fleury, J. Giovinazzo, I. Matea, N. Adimi, F. De Oliveira, I. Stefan, G. Georgiev, S. Grévy, J. C. Thomas, C. Borcea, D. Cortina, M. Caamano, M. Stanoiu, F. Aksouh, B. A. Brown, F. C. Barker, and W. A. Richter. First observation of ^{54}Zn and its decay by two-proton emission. *Phys. Rev. Lett.*, 94:232501, Jun 2005.

[190] P. Ascher, L. Audirac, N. Adimi, B. Blank, C. Borcea, B. A. Brown, I. Companis, F. Delalee, C. E. Demonchy, F. de Oliveira Santos, J. Giovinazzo, S. Grévy, L. V. Grigorenko, T. Kurtukian-Nieto, S. Leblanc, J.-L. Pedroza, L. Perrot, J. Pibernat, L. Serani, P. C. Srivastava, and J.-C. Thomas. Direct observation of two protons in the decay of ^{54}Zn. *Phys. Rev. Lett.*, 107:102502, Sep 2011.

[191] T. Goigoux, P. Ascher, B. Blank, M. Gerbaux, J. Giovinazzo, S. Grévy, T. Kurtukian Nieto, C. Magron, P. Doornenbal, G. G. Kiss, S. Nishimura, P.-A. Söderström, V. H. Phong, J. Wu, D. S. Ahn, N. Fukuda, N. Inabe, T. Kubo, S. Kubono, H. Sakurai, Y. Shimizu, T. Sumikama, H. Suzuki, H. Takeda, J. Agramunt, A. Algora, V. Guadilla, A. Montaner-Piza, A. I. Morales, S. E. A. Orrigo, B. Rubio, Y. Fujita, M. Tanaka, W. Gelletly, P. Aguilera, F. Molina, F. Diel, D. Lubos, G. de Angelis, D. Napoli, C. Borcea, A. Boso, R. B. Cakirli, E. Ganioglu, J. Chiba, D. Nishimura, H. Oikawa, Y. Takei, S. Yagi, K. Wimmer, G. de France, S. Go, and B. A. Brown. Two-proton radioactivity of ^{67}Kr. *Phys. Rev. Lett.*, 117:162501, Oct 2016.

[192] I. A. Egorova, R. J. Charity, L. V. Grigorenko, Z. Chajecki, D. Coupland, J. M. Elson, T. K. Ghosh, M. E. Howard, H. Iwasaki, M. Kilburn, Jenny Lee, W. G. Lynch, J. Manfredi, S. T. Marley, A. Sanetullaev, R. Shane, D. V. Shetty, L. G. Sobotka, M. B. Tsang, J. Winkelbauer, A. H. Wuosmaa, M. Youngs, and M. V. Zhukov. Democratic decay of ^{6}Be exposed by correlations. *Phys. Rev. Lett.*, 109:202502, Nov 2012.

[193] T. B. Webb, S. M. Wang, K. W. Brown, R. J. Charity, J. M. Elson, J. Barney, G. Cerizza, Z. Chajecki, J. Estee, D. E. M. Hoff, S. A. Kuvin, W. G. Lynch, J. Manfredi, D. McNeel, P. Morfouace, W. Nazarewicz, C. D. Pruitt, C. Santamaria, J. Smith,

L. G. Sobotka, S. Sweany, C. Y. Tsang, M. B. Tsang, A. H. Wuosmaa, Y. Zhang, and K. Zhu. First observation of unbound ^{11}O, the mirror of the halo nucleus ^{11}Li. *Phys. Rev. Lett.*, 122:122501, Mar 2019.

[194] T. B. Webb, R. J. Charity, J. M. Elson, D. E. M. Hoff, C. D. Pruitt, L. G. Sobotka, K. W. Brown, J. Barney, G. Cerizza, J. Estee, G. Jhang, W. G. Lynch, J. Manfredi, P. Morfouace, C. Santamaria, S. Sweany, M. B. Tsang, T. Tsang, S. M. Wang, Y. Zhang, K. Zhu, S. A. Kuvin, D. McNeel, J. Smith, A. H. Wuosmaa, and Z. Chajecki. Particle decays of levels in ^{11,12}N and ^{12}O investigated with the invariant-mass method. *Phys. Rev. C*, 100:024306, Aug 2019.

[195] M. Baldo, L. M. Robledo, P. Schuck, and X. Viñas. New kohn-sham density functional based on microscopic nuclear and neutron matter equations of state. *Phys. Rev. C*, 87:064305, Jun 2013.

[196] A. de Roubin, D. Atanasov, K. Blaum, S. George, F. Herfurth, D. Kisler, M. Kowalska, S. Kreim, D. Lunney, V. Manea, E. Minaya Ramirez, M. Mougeot, D. Neidherr, M. Rosenbusch, L. Schweikhard, A. Welker, F. Wienholtz, R. N. Wolf, and K. Zuber. Nuclear deformation in the $a \approx 100$ region: Comparison between new masses and mean-field predictions. *Phys. Rev. C*, 96:014310, Jul 2017.

[197] A. Welker, N. A. S. Althubiti, D. Atanasov, K. Blaum, T. E. Cocolios, F. Herfurth, S. Kreim, D. Lunney, V. Manea, M. Mougeot, D. Neidherr, F. Nowacki, A. Poves, M. Rosenbusch, L. Schweikhard, F. Wienholtz, R. N. Wolf, and K. Zuber. Binding energy of ^{79}Cu: Probing the structure of the doubly magic ^{78}Ni from only one proton away. *Phys. Rev. Lett.*, 119:192502, Nov 2017.

[198] S. Michimasa, M. Kobayashi, Y. Kiyokawa, S. Ota, D. S. Ahn, H. Baba, G. P. A. Berg, M. Dozono, N. Fukuda, T. Furuno, E. Ideguchi, N. Inabe, T. Kawabata, S. Kawase, K. Kisamori, K. Kobayashi, T. Kubo, Y. Kubota, C. S. Lee, M. Matsushita, H. Miya, A. Mizukami, H. Nagakura, D. Nishimura, H. Oikawa, H. Sakai, Y. Shimizu, A. Stolz, H. Suzuki, M. Takaki, H. Takeda, S. Takeuchi, H. Tokieda, T. Uesaka, K. Yako, Y. Yamaguchi, Y. Yanagisawa, R. Yokoyama, K. Yoshida, and S. Shimoura. Magic nature of neutrons in ^{54}Ca: First mass measurements of $^{55--57}$Ca. *Phys. Rev. Lett.*, 121:022506, Jul 2018.

[199] R. Orford, N. Vassh, J. A. Clark, G. C. McLaughlin, M. R. Mumpower, G. Savard, R. Surman, A. Aprahamian, F. Buchinger, M. T. Burkey, D. A. Gorelov, T. Y. Hirsh, J. W. Klimes, G. E. Morgan, A. Nystrom, and K. S. Sharma. Precision mass measurements of neutron-rich neodymium and samarium isotopes and their role in understanding rare-earth peak formation. *Phys. Rev. Lett.*, 120:262702, Jun 2018.

[200] Y. Ito, P. Schury, M. Wada, F. Arai, H. Haba, Y. Hirayama, S. Ishizawa, D. Kaji, S. Kimura, H. Koura, M. MacCormick, H. Miyatake, J. Y. Moon, K. Morimoto, K. Morita, M. Mukai, I. Murray, T. Niwase, K. Okada, A. Ozawa, M. Rosenbusch, A. Takamine, T. Tanaka, Y. X. Watanabe, H. Wollnik, and S. Yamaki. First direct mass measurements of nuclides around $z = 100$ with a multireflection time-of-flight mass spectrograph. *Phys. Rev. Lett.*, 120:152501, Apr 2018.

[201] E. Olsen, M. Pfützner, N. Birge, M. Brown, W. Nazarewicz, and A. Perhac. Landscape of two-proton radioactivity. *Phys. Rev. Lett.*, 110:222501, May 2013.

[202] E. Olsen, M. Pfützner, N. Birge, M. Brown, W. Nazarewicz, and A. Perhac. Erratum: Landscape of two-proton radioactivity [phys. rev. lett. 110, 222501 (2013)]. *Phys. Rev. Lett.*, 111:139903, Sep 2013.

[203] W. Nazarewicz, J. Dobaczewski, T. R. Werner, J. A. Maruhn, P.-G. Reinhard, K. Rutz, C. R. Chinn, A. S. Umar, and M. R. Strayer. Structure of proton drip-line nuclei around doubly magic ^{48}Ni. *Phys. Rev. C*, 53:740–751, Feb 1996.

[204] Junlong Tian, Ning Wang, Cheng Li, and Jingjing Li. Improved kelson-garvey mass relations for proton-rich nuclei. *Phys. Rev. C*, 87:014313, Jan 2013.

[205] B. Alex Brown. Diproton decay of nuclei on the proton drip line. *Phys. Rev. C*, 43:R1513–R1517, Apr 1991.

[206] L. V. Grigorenko, I. Mukha, D. Kostyleva, C. Scheidenberger, L. Acosta, E. Casarejos, V. Chudoba, A. A. Ciemny, W. Dominik, J. A. Dueñas, V. Dunin, J. M. Espino, A. Estradé, F. Farinon, A. Fomichev, H. Geissel, A. Gorshkov, Z. Janas, G. Kamiński, O. Kiselev, R. Knöbel, S. Krupko, M. Kuich, Yu. A. Litvinov, G. Marquinez-Durán, I. Martel, C. Mazzocchi, E. Yu. Nikolskii, C. Nociforo, A. K. Ordúz, M. Pfützner, S. Pietri, M. Pomorski, A. Prochazka, S. Rymzhanova, A. M. Sánchez-Benítez, P. Sharov, H. Simon, B. Sitar, R. Slepnev, M. Stanoiu, P. Strmen, I. Szarka, M. Takechi, Y. K. Tanaka, H. Weick, M. Winkler, J. S. Winfield, X. Xu, and M. V. Zhukov. Deep excursion beyond the proton dripline. ii. toward the limits of existence of nuclear structure. *Phys. Rev. C*, 98:064309, Dec 2018.

[207] M. Gonçalves, N. Teruya, O.A.P. Tavares, and S.B. Duarte. Two-proton emission half-lives in the effective liquid drop model. *Physics Letters B*, 774:14 – 19, 2017.

[208] L. V. Grigorenko and M. V. Zhukov. Two-proton radioactivity and three-body decay. ii. exploratory studies of lifetimes and correlations. *Phys. Rev. C*, 68:054005, Nov 2003.

[209] J Erler, N Birge, M Kortelainen, W Nazarewicz, E Olsen, A Perhac, and M Stoitsov. Microscopic nuclear mass table with high-performance computing. *Journal of Physics: Conference Series*, 402:012030, dec 2012.

[210] Rui Wang and Lie-Wen Chen. Positioning the neutron drip line and the r-process paths in the nuclear landscape. *Phys. Rev. C*, 92:031303, Sep 2015.

[211] J. P. Delaroche, M. Girod, J. Libert, H. Goutte, S. Hilaire, S. Péru, N. Pillet, and G. F. Bertsch. Structure of even-even nuclei using a mapped collective hamiltonian and the d1s gogny interaction. *Phys. Rev. C*, 81:014303, Jan 2010.

[212] A.V. Afanasjev, S.E. Agbemava, D. Ray, and P. Ring. Nuclear landscape in covariant density functional theory. *Physics Letters B*, 726(4):680 – 684, 2013.

[213] S. E. Agbemava, A. V. Afanasjev, D. Ray, and P. Ring. Global performance of covariant energy density functionals: Ground state observables of even-even nuclei and the estimate of theoretical uncertainties. *Phys. Rev. C*, 89:054320, May 2014.

[214] X.W. Xia, Y. Lim, P.W. Zhao, H.Z. Liang, X.Y. Qu, Y. Chen, H. Liu, L.F. Zhang, S.Q. Zhang, Y. Kim, and J. Meng. The limits of the nuclear landscape explored by the relativistic continuum hartree-bogoliubov theory. *Atomic Data and Nuclear Data Tables*, 121-122:1 – 215, 2018.

[215] A. V. Afanasjev, S. E. Agbemava, D. Ray, and P. Ring. Neutron drip line: Single-particle degrees of freedom and pairing properties as sources of theoretical uncertainties. *Phys. Rev. C*, 91:014324, Jan 2015.

[216] Takeshi Kodama. β-Stability Line and Liquid-Drop Mass Formulas. *Progress of Theoretical Physics*, 45(4):1112–1122, 04 1971.

[217] Quantified landscape of nuclear existence. `https://people.nscl.msu.edu/~witek/Projects/Bayes/fig_landscape1.pdf`.

[218] L.M. Robledo. Enhancement of octupole strength in near spherical nuclei. *Eur. Phys. J. A*, 52:300, 2016.

[219] Paulo Bedaque et al. Report from the A.I. For Nuclear Physics Workshop. 6 2020.